

The Impact of the Progenitor White Dwarf's Composition on Thermonuclear Supernovae

Diploma Thesis

by

Sebastian Thomas Ohlmann

November 2012



Contents

1	Introduction	1
1.1	History of Supernova Observation	1
1.2	Observations of Supernovae	2
1.2.1	Classification	3
1.2.2	Spectroscopic and Photometric Properties	4
1.3	SN Ia Progenitor Systems and Explosion Models	6
1.3.1	Progenitor Channels	7
1.3.2	Recent Findings	12
1.4	Impacts on Other Research Fields	13
1.5	Previous Work	13
1.6	Objectives of This Work	14
2	Physical Foundations	17
2.1	Hydrodynamics	17
2.1.1	Conservation Laws	17
2.1.2	Reactive Euler Equations	18
2.1.3	Instabilities	19
2.2	Nuclear Reactions	20
2.2.1	Nuclear Reaction Networks	20
2.2.2	Nuclear Statistical Equilibrium	21
2.3	Combustion Physics	22
2.3.1	Simple Theory	22
2.3.2	Detonations	24
2.3.3	Deflagrations	27
2.3.4	Deflagration-Detonation Transition	28
2.4	Progenitor Evolution	29
2.4.1	Binary Pre-Supernova evolution	29
2.4.2	Pre-Ignition Phase	30
2.5	Thermodynamical Properties of WD Matter	31
3	Numerical Methods	33
3.1	Hydrodynamical Simulations	33
3.1.1	Discretization of the Euler Equations	33
3.1.2	Level Set Method	35
3.1.3	LEAFS	37
3.2	Nuclear Reactions	42
3.2.1	Nuclear Reaction Network	42

3.2.2	Postprocessing	42
3.2.3	Nuclear Statistical Equilibrium	43
3.3	Iterative Computation of Abundance Tables	44
4	Results	47
4.1	Iterative Calibration	47
4.1.1	Detonations	47
4.1.2	Deflagrations	52
4.2	2D Simulations	59
4.2.1	Initial Models	60
4.2.2	Hydrodynamical Evolution	61
4.2.3	Nucleosynthetic Yields	64
4.2.4	Distribution of Ejecta in Velocity Space	68
4.2.5	Synthetic Light Curves and Spectra	70
4.3	3D Simulations	72
4.3.1	Initial Models	73
4.3.2	Hydrodynamical Evolution	74
4.3.3	Nucleosynthetic Yields	76
4.3.4	Distribution of Ejecta in Velocity Space	78
5	Conclusions	83
5.1	Properties of Burning Fronts	83
5.2	Impact on Simulations of Delayed Detonations	84
5.3	Outlook	85
A	Nucleosynthetic Yields for 2D Simulations	87
	Bibliography	91
	Zusammenfassung	101

1 Introduction

1.1 History of Supernova Observation

Ever since the dawn of mankind, the dark night sky with its sparkling stars has fascinated humans. For a long time, these stars had been believed to be pinned immovably to some kind of heavenly sphere which rotates throughout the night. And in front of this immutable background, the sun and the planets followed their tracks according to some complex but nevertheless invariant law. How much more fascinating must have been *transient phenomena*, breaking the eternal steadiness of the celestial sphere!

One of the first observations of these phenomena recorded in newer times dates back to the year 1006. Astronomers mainly in China and Japan witnessed a new star emerging in the sky, being visible over several years before fainting again. This event is supposed to be the brightest transient event in recorded history—apart from comets. Several centuries later, in 1572, a very bright new star appeared in the constellation Cassiopeia, challenging in brightness even Venus. This event was documented very well by Tycho Brahe in his book “*De nova stella*” (Brahe, 1573), describing the appearance of a “new star”. This coined the term *nova* for these bright transient phenomena. Many more of these and similar events were observed in the following centuries, raising the need for a better terminology. Thus, the term *supernova* (SN) was used first by W. Baade and F. Zwicky in the 1930s to classify certain transient events, comprising the ones from 1054 and 1572. An image of the supernova remnant left behind by Tycho’s supernova

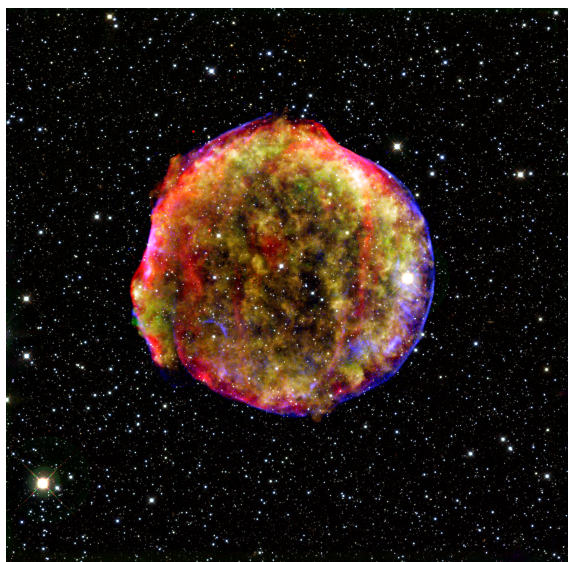


Figure 1.1 | Tycho’s supernova (SN 1572). This image combines data from the space observatories Spitzer in the infrared part of the spectrum and Chandra in the X-ray part, as well as optical data from the Calar Alto observatory in Spain. Courtesy NASA/JPL-Caltech/CXC/Calar Alto, O. Krause (Max-Planck Institute for Astronomy).

combined from data from several modern telescopes (Spitzer, Chandra, Calar Alto) reveals a very complex structure (Figure 1.1). For more information on the history of supernovae see Green & Stephenson (2003). They give an overview over historical supernovae—including SN 1006 and SN 1572—and compile historical records from various sources.

The interest in supernovae has persisted to the present, and the development of new telescopes and instruments has allowed us to improve our knowledge of these fascinating objects more and more. As supernovae belong to the brightest and most energetic events in the Universe, modern telescopes can observe them out to the edge of the Universe. Albeit a large number of supernovae are observed nowadays, their physical mechanism is still not known in detail. It is known, however, that a variety of different kinds of supernovae exist and that they all are explosions marking the death of a star—contrary to what their name might suggest.

In order to elucidate the nature of supernovae, the quest of classifying supernovae according to their light curves and spectra began in the 1930s. This was improved over the years, and finally led to the insight that two physically distinct mechanisms may explain the diversity of supernovae: thermonuclear explosions of white dwarfs (WDs) and core collapses of massive stars.

This work aims at improving numerical modeling of thermonuclear explosions. The following sections give an introduction to SNe focussing on thermonuclear events.

1.2 Observations of Supernovae

Supernovae occur somewhere in the Universe far away from our solar system. Therefore, the only information we can gather from these events is electromagnetic radiation and—in the case of nearby core collapse supernovae—neutrinos and cosmic rays from remnants. Since we cannot gain information about these objects by experimenting with them on Earth, we are restricted to observations as the acid test of any model we build to explain them.

Observations of supernovae, like all astronomical observations in the optical and adjacent bands, rely on two methods: *spectroscopy* and *photometry*. Spectroscopy uses a spectrometer in order to resolve the flux of the emitted electromagnetic radiation as a function of the wavelength of the radiation and thus yields spectra. Photometry measures the total emitted flux in images taken with or without a filter. Multi-band photometry is equivalent to spectroscopy with very low resolution and yields fluxes which are averaged over larger parts of the electromagnetic spectrum and which are called light curves. Spectroscopy yields more detailed information about the observed object than photometry. One advantage of photometry on the other side is that it is also possible for rather faint objects, where spectroscopy cannot be done. For objects radiating approximately a thermal spectrum, as e.g. stars, photometry can be used to determine colors and consequently the surface temperature. The most common system for photometry is the system of *UBVRI* passbands (Bessell, 1990), where for each passband a certain filter is applied, thus restricting the radiation to the corresponding band.

1.2.1 Classification

The spectral classification of supernovae uses photometric and spectroscopic properties of the corresponding objects. The discussion here follows the works of Filippenko (1997) and Leibundgut (2000). A summary of the classification scheme is given in Figure 1.2, which shows the most common supernova types. As the classification of supernovae evolved historically from photometric and spectroscopic properties, it does not reflect the main differentiation with regard to the underlying physical mechanisms, i.e. the distinction of thermonuclear and core collapse supernovae.

The basic supernova classes are Type I and Type II supernovae. They are distinguished by the presence of hydrogen lines: Type II supernovae (SNe II) are defined by the presence, Type I supernovae (SNe I) by the absence of H lines in their optical spectra, usually at maximum brightness. SNe II can be further divided into the subclasses SN IIP (“plateau”) and SN IIL (“linear”), according to the shape of their light curve, as well as SN IIn and SN IIb. The class of SNe I consists of the subclasses SN Ia, SN Ib and SN Ic. SNe Ia are defined by showing strong Si II absorption lines near maximum light, whereas SNe Ib and Ic do not show these. SNe Ib are further distinguished from SNe Ic by the presence of moderately strong He I lines. As Li et al. (2011) found out, 24% of all supernovae are Type Ia supernovae, 57% Type II supernovae and 19% Type Ib and Ic supernovae.

The observationally motivated classification in the end reflects the physical explosion mechanism at least in parts: SNe Ia are believed to be explained by thermonuclear explo-

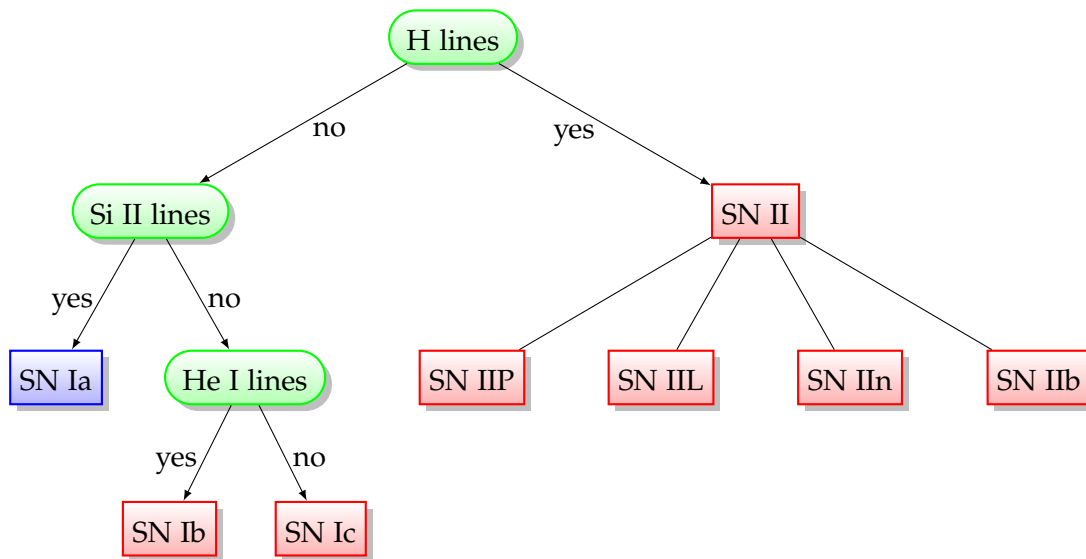


Figure 1.2 | Spectroscopical classification scheme of supernovae. The green, rounded boxes show the element lines and a subsequent classification decision depends on the presence of these lines in the spectra (usually at maximum brightness). The blue box shows the SN type associated with thermonuclear explosions. The red boxes display SN types associated with a core collapse mechanism. This classification follows Filippenko (1997). For explanations of the different types see text.

sions of carbon/oxygen white dwarfs in binary systems, whereas all other spectroscopic classes are believed to be the result of a core collapse of a massive star.

1.2.2 Spectroscopic and Photometric Properties

The spectroscopic and photometric properties of supernovae are extensively discussed by Filippenko (1997). The particular properties of SNe Ia are further discussed in Hillebrandt & Niemeyer (2000) and Leibundgut (2000).

The early-time spectra of SNe, taken in the “photospheric phase”, are characterized by broad lines, i.e. the ejecta move at high velocities up to several 10 000 km/s. The characteristic lines show up in the form of *P-Cygni profiles* for all types, except for emission-dominated features. A P-Cygni profile arises when absorbing—and re-emitting—material moves outwards, thereby enclosing an optically thick, radiating core. It consists of two main contributions: a blue-shifted, broadened absorption feature and a wide (re-)emission component at the rest-frame wavelength. The emission component is caused by all material moving outwards and is thus subject to Doppler line broadening. The absorption feature, however, is due to the material in front of the opaque core, moving towards the observer and thus causing a blue-shifted absorption feature, which is superimposed on the emission feature. The material behind the optically thick core does not contribute, since it is obscured by the core.

Late-time spectra of SNe taken in the “nebular phase”, when the core has become transparent, show broad emission lines. In SNe Ia, these are mostly due to iron group elements (IGE; e.g. Fe, Co), whereas SNe Ib and Ic display emission lines mostly of intermediate mass elements (IME; e.g. O, Ca) and He (for SNe Ib). The late-time spectra of SNe II form a very heterogeneous class.

Type Ia Supernovae

As Type Ia supernovae belong to the class of SNe I, they do not show any H lines in their spectra at any time. Their characteristic spectroscopic feature in early-time spectra is a deep and wide absorption line at around 6150 Å, which is the blue-shifted part of the P-Cygni profile of the Si II lines at rest wavelengths of 6347 Å and 6371 Å. This feature distinguishes SNe Ia from SNe Ib and Ic. The early-time spectra in general are characterized by lines from various IME (O, Mg, Si, S, Ca) as well as IGE (e.g. Fe, Ni, Cr, Ti, Co) in the bluer part of the spectrum. As the ejecta expand and the density decreases, the opacity decreases as well and the photosphere—the outer edge of the optically thick core—moves inward. About two weeks after maximum brightness, Fe II lines dominate the spectrum. This means that iron is abundant in the inner core, which is now revealed in the spectrum. Late-time spectra in the nebular phase, which the SN enters after a long transitional phase of about 100 d, are dominated by emission lines from Fe and Co.

The light curves of “normal” SNe Ia show only limited variability (Branch et al., 1993). As found by Riess et al. (1999), the rise time from explosion to the maximum of brightness in the *B* band is $19.5 \text{ d} \pm 0.2 \text{ d}$ for a typical Type Ia supernova. A typical SN Ia is characterized by a peak magnitude in *B* band of about -19.5 mag and a decline in

magnitude from B band maximum to 15 days afterwards of $\Delta m_{15}(B) \approx 1.1$ mag (Riess et al., 1999). In the first month after B band maximum, the light curve usually declines by about three magnitudes. After the first month, the decline continues at a rate of about one magnitude per month (Hillebrandt & Niemeyer, 2000). In the near infrared, especially in the I band and at redder wavelengths, a second maximum appears for normal SNe Ia between 21 and 30 days after B band maximum (Leibundgut, 2000).

The light curve—and the electromagnetic emission in general—is powered by the radioactive decay of ^{56}Ni and its daughter nucleus ^{56}Co (Truran et al., 1967; Colgate & McKee, 1969). Thus, the amount of ^{56}Ni produced in a SN Ia through thermonuclear burning determines the peak luminosity.

Different characteristics of the light curves of normal SNe Ia correlate with each other (for an overview, see Branch, 1998). Most prominently, this shows up in the “Phillips relation” (Phillips, 1993) between the maximum magnitude in B , V or I band and the decline in B band $\Delta m_{15}(B)$. In conjunction with other correlations, normal SNe Ia seem to form a one-parameter family ranging from stronger explosions with high luminosities and slow light curves to weaker explosions with low luminosities and fast light curves (Branch, 1998). From the light curve width or from $\Delta m_{15}(B)$ the peak magnitude of a SN Ia can be estimated. This allows to use them as distance indicators in cosmology (Riess et al., 1998; Schmidt et al., 1998; Perlmutter et al., 1999).

Although the class of Type Ia supernovae is rather homogeneous, compared with other classes, only 70% of all SNe Ia are classified as normal (Li et al., 2011), whereas the other SNe Ia consist of peculiar objects and is further sub-classified (Li et al., 2011): 15% are 1991bg-like objects, 9% are 1991T-like and 5% are 2002cx-like. SNe Ia similar to 1991bg are sub-luminous, the colors are redder at maximum brightness, but slightly bluer at late times and the second maximum in the I band is missing (Filippenko, 1997). 1991T-like SNe, however, are super-luminous objects lacking the Si II lines in pre-maximum spectra and showing low IME velocities (Filippenko, 1997). 2002cx-like SNe are sub-luminous and miss the second maximum in the I band, similar to 1991bg-like objects, but show 1991T-like pre-maximum spectra and have very low line velocities (Phillips et al., 2007).

Type Ib and Ic Supernovae

Type Ib and Ic supernovae do not show signs of hydrogen in their spectra and do not show the prominent Si II absorption line as it is characteristic for SNe Ia. The general light curves are similar to SNe Ia, but the maximum brightness is typically 1.5 mag fainter than normal SNe Ia and the colors are reddish (Filippenko, 1997). Li et al. (2011) give fractions of 21% for SNe Ib, 54% for SNe Ic and 25% for peculiar objects, named Ibc-pec.

Type II Supernovae

All SNe II show hydrogen lines in their spectra, although with a varying strength and profile of the $H\alpha$ line (Filippenko, 1997). Apart from that, the early-time as well as the late-time spectra constitute a very heterogeneous class. The main two subclasses

characterize the shape of the light curves: the light curve of SNe II-L (“linear”) is similar to SN I light curves, whereas SNe II-P (“plateau”) show a plateau in the light curve after maximum brightness (Filippenko, 1997). Type II_n supernovae show narrow components of the H α emission lines and seem to be bluer at early times (Filippenko, 1997). The last subclass, Type II_b supernovae, is linked to Type Ib supernovae: at early times, the spectra show H α lines, as do SNe II, but at late times the spectra gradually turn into SNe Ib, being dominated by He (and also IME/IGE) features.

The most common subclass of Type II supernovae are SNe II-P with 70%. The other subclasses are of similar frequencies, namely SNe II-L with 10%, SNe II_b with 12% and SNe II_n with 9% (Li et al., 2011).

1.3 SN Ia Progenitor Systems and Explosion Models

Despite the ongoing efforts in the past years, no progenitor system of a SN Ia has been unambiguously identified by now. In order to shed light on their nature, results from stellar evolution models have to be combined with observations. Since the progenitors have never been identified observationally, all progenitor models have to be considered and the ones not compatible with observations or physical principles have to be ruled out. Unfortunately, in the case of SNe Ia this procedure has not singled out one specific progenitor system but yields several possible models. The key result is that the progenitor systems incorporate white dwarfs consisting of carbon and oxygen in interacting binary systems. The different channels are the *double degenerate* (DD) scenario, where the binary system consists of two carbon/oxygen white dwarfs, and the *single degenerate* (SD) scenario, where the companion star of the carbon/oxygen WD is a non-degenerate star—e.g. a main sequence star or a red giant. Good overviews of how this result was reached are given in Leibundgut (2000) and Hillebrandt & Niemeyer (2000).

One fact constraining the nature of the progenitor system comes from the short rise time and peak phase, indicating a compact object. The fact that neither hydrogen nor helium—the two most abundant elements in the universe—are present in the spectra hints to highly evolved objects. This is also supported by the occurrence of SNe Ia in elliptical galaxies with their older stellar population (Leibundgut, 2000). Long-lived compact objects are usually stable and the violent event of a SN Ia indicates the presence of a companion star, triggering the supernova. This suggests an interacting binary system as progenitor system. As already mentioned in Section 1.2.2, the light curve of SNe Ia is powered by the radioactive decay of ^{56}Ni and its daughter nucleus. Thus, nuclear fusion provides the energy source for these events—opposed to SNe II, which are powered by the release of gravitational energy. All these reasons suggest that a Type Ia supernova is a thermonuclear explosion of a white dwarf. The composition of this WD can be He, C/O and O/Ne. He WDs can be excluded because of their explosion characteristics (see Woosley et al., 1986, and references therein). O/Ne WDs, on the other hand, are supposed to undergo a collapse to a neutron star when they reach high enough masses rather than an explosion due to electron capture reactions (Nomoto & Kondo, 1991). This finally leaves carbon/oxygen white dwarfs as the favored progenitors for SNe Ia.

1.3.1 Progenitor Channels

As noted above, the two main scenarios for SN Ia progenitor systems are the single degenerate (SD) and the double degenerate (DD) scenario. These scenarios include several explosion channels which can be distinguished by the mass of the WDs and the burning modes causing the explosion. A WD consists of a plasma of ionized nuclei and degenerate electrons and is stabilized against gravity by the degeneracy pressure of the electrons. This yields an upper limit for the mass of a stable WD, the Chandrasekhar mass (Chandrasekhar, 1931), which is used to classify white dwarfs into sub-Chandrasekhar, Chandrasekhar and “super-Chandrasekhar” white dwarfs. The two distinct burning modes which can be present in these explosions are subsonic deflagrations and supersonic detonations (see Section 2.3 for more details on this). Now the combination of the burning modes and initial masses yields a wide range of different explosion scenarios with different outcomes.

Single Degenerate Scenario

In the single degenerate scenario, the companion star of the exploding white dwarf is either a main sequence star or a red giant. Through mass overflow from this companion to the WD, H or He is transferred to the surface of the WD, where the material is steadily burned if the conditions are suitable (Leibundgut, 2000).

In the *Chandrasekhar mass model*, it is assumed that the accreted material burns to carbon and oxygen, increasing the mass of the WD until nearly reaching the Chandrasekhar mass. Shortly before this mass is reached, the rise in density in the core of the WD renders carbon fusion possible. A simmering phase follows, where the heat from the carbon burning can be transferred outwards by convection processes. But when a critical temperature is reached, a thermonuclear runaway can occur: because of the degeneracy of the electrons, a further rise in temperature is not followed by a rise in pressure, thus leading to the formation of hot spots. Now, due to the sensitivity of the reaction rates on temperature, a runaway may occur in these hot spots.

Depending on the type of burning which is establishing in the course of the explosion, different models have been proposed:

- The *pure detonation* model assumes that a detonation wave is initiated near the core of the WD. The initial density in Chandrasekhar mass models is on the order of 10^9 g/cm^3 and hydrostatic models show a steep density gradient only at the outer edge of the WD. As the density threshold for burning to nuclear statistical equilibrium (NSE) lies at around 10^7 g/cm^3 (see also the results in Section 4.1.1), most of the WD is burned to ^{56}Ni yielding ^{56}Ni masses of $\sim 1.3 M_{\odot}$. Since this is too bright even for the super-luminous class of 1991T-like SNe¹, the pure detonation model cannot explain SNe Ia. Moreover, the amount of intermediate mass elements produced in such a pure detonation is insufficient to explain the spectra (Hillebrandt & Niemeyer, 2000).

¹SN1991T, e.g., produced $1.1 M_{\odot}$ of ^{56}Ni according to Leibundgut (2000).

- The *pure deflagration* model assumes a deflagration being ignited near the core of the WD. First, laminar burning takes place. This in turn leads to the formation of hydrodynamical instabilities producing turbulent motion, which greatly enhances the nuclear burning (see Section 2.3). Since the burning propagates subsonically, the material ahead of the deflagration front is pre-expanded. Thus, a significant part of the material can be burned at lower densities, thereby producing the IME missing in the pure detonation scenario.

Parametrized one-dimensional models were very successful in explaining SNe Ia spectra and light curves, especially the *W7* model by Nomoto et al. (1984) and Iwamoto et al. (1999). The key for the success of this model was to assume that the propagation speed of the deflagration front is enhanced by turbulence up to about 30% of the sound speed (Hillebrandt & Niemeyer, 2000). More recent multi-dimensional models (e.g. Reinecke et al., 2002b; Röpke et al., 2006a) with a focus on first principles calculations have shown that deflagrations can provide enough explosion energy to unbind the star. Despite this, however, the mass of ^{56}Ni produced during the explosion is too small with a maximum of roughly $0.5 M_{\odot}$ of ^{56}Ni (Röpke et al., 2006a) in order to explain normal SNe Ia. Moreover, a strong mixing of the explosion products is predicted due to the turbulent burning, in contradiction to the layered structure indicated by observations.

A very recent study by Kromer et al. (2012) with refined numerical methods indicates that deflagration models could explain the peculiar subtype of 2002cx-like SNe Ia.

- The *delayed detonation* model is inspired by terrestrial experiments showing that a deflagration may under certain conditions trigger a detonation (e.g. Clavin, 2004). Now the assumption is that such a deflagration-detonation transition (DDT) may also occur in the context of thermonuclear flames (Blinnikov & Khokhlov, 1986; Khokhlov, 1991a). Opposed to the pure detonation model, the delayed detonation has the advantage that the detonation burns the material pre-expanded by the deflagration. A transition density was used as a fitting parameter in early one dimensional models and was found to be of the order of 10^7 g/cm^3 (Höflich & Khokhlov, 1996; Iwamoto et al., 1999). Just slightly below this transition density lies the density range, where IME are produced in detonations (Section 4.1.1). Hence, a substantial amount of IME is produced in a layer nearly surrounding the deflagration ashes.

This behaviour has also been found in a study by Röpke & Niemeyer (2007), where three dimensional simulations were conducted using a fixed DDT criterion based on density and the effective Karlovitz number (the same as in Golombek & Niemeyer, 2005) in the spirit of a first principles simulation. They found that the models they computed are all in the range of normal SNe Ia concerning the mass of produced IGE and IME. In a very recent survey by Seitenzahl et al. (2012), fourteen three dimensional simulations of delayed detonation models are presented with detailed nucleosynthetic yields. They employ a more elaborate DDT criterion

involving the velocity distribution generated by the deflagration. Their models span the range of ^{56}Ni masses needed for explaining the natural luminosity range of normal SNe Ia. Thus, the delayed detonation model seems to explain normal SNe Ia quite well, yet synthetic spectra should be computed and compared with observed spectra, as already done in two dimensions by Kasen et al. (2009) and Blondin et al. (2011).

The delayed detonation model of Chandrasekhar mass white dwarfs is also examined in this diploma thesis, where the models from Seitenzahl et al. (2012) are improved by taking into account a more realistic progenitor composition.

- Another model which combines an initial deflagration phase with a detonation later on is the *pulsational delayed detonation* model, which was investigated by Arnett & Livne (1994a,b). The basic assumption is that the deflagration fails to unbind the star, resulting in a pulsation. During the contraction phase, the material in the core heats up and finally ignites a detonation wave.
- The *gravitationally confined detonation* model (Plewa et al., 2004; Jordan et al., 2008) also combines an initial deflagration with a detonation in a pre-expanded medium. In this model, the deflagration starts off-center, rises to the surface of the star and propagates around the star to converge at the antipodal point, where a detonation is initiated. The three dimensional models presented in Jordan et al. (2008) produce rather large amounts of ^{56}Ni and only small amounts of IME and could thus only be an explanation for high-luminosity SNe Ia.

This model has been refined to the “*pulsationally-assisted*” *gravitationally confined detonation* model (Jordan et al., 2012), which leads to a greater pre-expansion of the WD and thus to lower ^{56}Ni masses. Here, the deflagration is stronger than in the previous model, thus releasing more energy in the early phase leading to a greater pre-expansion. Then the detonation cannot be initiated by the deflagration ashes converging in the antipodal point of the surface, but a pulsation of the star drives the ignition of a detonation, similar to the pulsational delayed detonation mechanism. Three dimensional simulations by Jordan et al. (2012) yield lower ^{56}Ni masses compatible with normal SNe Ia. It is, however unclear, if the amounts of IGE and IME produced at the surface by the initial deflagration is compatible with observations. To further judge the validity of this model, radiative transfer calculations should be done in order to compare the synthetic spectra and light curves to observables.

Apart from these Chandrasekhar mass models, models exist where a *sub-Chandrasekhar mass* WD explodes. They do not reach the critical mass by accretion, because an external event triggers the explosion before. On the surface of the WD, a He layer is accreted by mass overflow from the companion star. When this layer is massive enough, a detonation can be ignited in the He shell. This detonation surrounds the WD and the shock waves emitted from the detonation may converge in the core of the WD, thereby causing a secondary detonation of the carbon/oxygen core. Thus, this scenario is also called *double*

detonation sub-Chandrasekhar mass model (Nomoto, 1980; Iben & Tutukov, 1984). The secondary detonation of the C/O core can alternatively also be ignited directly at the edge of the core. These double detonation models have been studied (for references, see Hillebrandt & Niemeyer, 2000), but face severe problems: The detonation of the outer He shell produces a significant amount of ^{56}Ni in the outer layers at higher velocities than the IME and inner iron and nickel core. This clearly contradicts the early-time and maximum brightness spectra, thus disfavoring this model.

Despite this, recent multi dimensional simulations have shown that the mechanism of triggering a secondary detonation near the center of the core through converging shock waves is rather robust (Fink et al., 2007), although large amounts of ^{56}Ni are produced in the outer layers. This restriction may be alleviated by the results of Fink et al. (2010), as they find that lower He shell masses, such as predicted in the AM CVn models of Shen et al. (2010), may trigger a secondary detonation as was thought necessary before, especially for higher mass WDs. Although less ^{56}Ni is produced in the outer layers, still substantial amounts of other IGE, as for example Cr and Ti, are synthesized, leading to inconsistencies of the synthetic spectra with the observed spectra (see the radiative transfer calculations in Kromer et al., 2010). A better agreement of the spectra with observations can be reached if the He shell is enriched by carbon through some mixing process (Kromer et al., 2010). If the effects of the He shell are neglected altogether, as done in Sim et al. (2010) for explosions of pure C/O sub-Chandrasekhar WDs, the resulting models can reproduce the characteristics of the range of normal SNe Ia. Thus, the sub-Chandrasekhar mass double detonation model may explain normal Type Ia supernovae if some mechanism can be found suppressing the effects of the burning products of the accreted He shell.

Although the Chandrasekhar mass limits the stability of WDs, this limit can be pushed up, allowing for *super-Chandrasekhar mass* models which are supported by rotation. In principle, rotating WDs simply have an increased Chandrasekhar mass due to the rotation. But since the masses of the WDs are usually compared to the Chandrasekhar mass of non-rotating WDs, the term super-Chandrasekhar mass WDs is used frequently. Yoon & Langer (2004) show that accretion onto the white dwarf taking rotation into account leads to differentially rotating WDs with masses beyond the Chandrasekhar mass, up to $1.9 M_{\odot}$.

Such rapidly rotating WDs have been used as progenitor systems for thermonuclear explosions. Pfannes et al. (2010b) find that deflagrations occurring in these rotating WDs develop strong anisotropies along the rotational axis, thus leaving large amounts of unburnt matter behind. These weak explosions are not able to explain normal SNe Ia, similar to pure deflagrations of non-rotating WDs. Pure detonations, however, could possibly explain super-luminous events of the 1991T-like subclass of SNe Ia (Pfannes et al., 2010a). Due to the different density profile, which is not as steep as in the non-rotating case, the pure detonation produces appreciable amounts of IME, apart from large ^{56}Ni masses (as high as $1.48 M_{\odot}$, see Pfannes et al., 2010a). Despite this, the amount of IME may be overestimated in this study due to their simplified assumptions about the transitions to the different burning stages. Moreover, Fink (2010) finds that an improved treatment of the burning scheme leads to IME being present at high velocities (on the

order of 20 000 km/s), which is incompatible with observations, which predict IME at rather low velocities (e.g. ~ 9000 km/s for the Si lines).

Delayed detonation models of these super-Chandrasekhar mass WDs have been simulated by Howell et al. (2006) and Fink (2010), but cannot explain SNe Ia as no carbon is left over after the detonation, in contradiction to observations which predict a layer of unburnt carbon. Moreover, the velocities of the IME are too high to match the observations of super-luminous SNe Ia.

Double Degenerate Scenario

In the double degenerate scenario, the primary carbon/oxygen white dwarf is accompanied by a secondary carbon/oxygen white dwarf (Webbink, 1984). This binary system eventually merges due to the emission of gravitational waves. Simulations of the merging process show that the smaller secondary WD is disrupted and forms an accretion disk around the primary (Benz et al., 1990; Lorén-Aguilar et al., 2009). At high accretion rates, it is most likely that a carbon deflagration ignites off-center, burning inwards and thereby converting the C/O WD into a O/Ne WD (Saio & Nomoto, 1985, 1998). A O/Ne WD near the Chandrasekhar mass, however, may be unstable after ignition due to electron captures. This results in a gravitational collapse, leading to the formation of a neutron star (Saio & Nomoto, 1985; Nomoto & Kondo, 1991).

Another scenario which occurs in the case of two WDs with similar masses is the *violent merger scenario* (Pakmor et al., 2010, 2011, 2012b). Instead of a slow disruption of the lighter secondary WD, the two WDs merge violently on a time scale of only a few orbits. Compression of the material at the interface between the merging WDs leads to heating and thus to the formation of hot spots in high density regions. Under the conditions given in these hot spots, a detonation may spontaneously ignite (Seitenzahl et al., 2009; Pakmor et al., 2011, 2012b) and consume the WDs. In principle, super-luminous events could be expected from such progenitor systems, as the combined mass of the WDs may well exceed the Chandrasekhar mass. But as the density in most of the material is as low as in the sub-Chandrasekhar-mass model—because the two WDs obviously are sub-Chandrasekhar-mass WDs and the core of the primary is virtually unaffected by the merger—the outcome of the violent merger model resembles the sub-Chandrasekhar-mass models. Pakmor et al. (2010) find that the merger of two WDs with masses near $0.9 M_{\odot}$ may explain the sub-luminous class of 1991bg-like events. A more recent simulation with two WDs with masses of $0.9 M_{\odot}$ and $1.1 M_{\odot}$ resembles a normal SN Ia, also with respect to light curves and line velocities (Pakmor et al., 2012b).

It may thus be concluded that violent mergers in the double degenerate scenario can produce sub-luminous as well as normal Type Ia supernovae. But there is still a huge parameter space to be explored in further studies.

Apart from this, the classification in single and double degenerate scenarios may not be as useful as it seems. The double detonation sub-Chandrasekhar-mass scenario, for example, can have progenitor systems from both scenarios. The binary population synthesis results from Ruitter et al. (2011) show that 87% of these double detonation sub-Chandrasekhar-mass models incorporate a He WD as a companion star and thus

a double degenerate progenitor system. One may also conclude here that the double degenerate channel may not only produce mergers, but also other models.

1.3.2 Recent Findings

The recent discovery of the nearby supernova SN 2011fe by the Palomar Transient Factory (Nugent et al., 2011a,b) provides very good observational data. In order to constrain the progenitor system, Röpke et al. (2012) compare observed spectra with synthetic spectra of two different explosion models: one delayed detonation of a Chandrasekhar-mass WD and one violent merger of two sub-Chandrasekhar-mass WDs. Both models reproduce the main features, and an unambiguous decision is not possible based on early-time and maximum brightness spectra. Perhaps, late-time light curves depending on the nucleosynthetic abundances of iron group elements powering the light curve may discriminate between the different scenarios (Röpke et al., 2012).

Another way of obtaining constraints on the nature of SNe Ia progenitors involves examining statistical properties as for example delay time distributions (DTD) and brightness distributions of SNe Ia. The DTD describes the distribution of the times between the birth of the progenitor system and the explosion for a sample of SNe. This becomes more and more feasible as more and more SNe Ia are observed, delivering more data. The results from comparing the DTD obtained from observed SN Ia rates with analytical estimates favors the double degenerate channel (e.g. Maoz et al., 2010). This is mainly due to their higher number in total. Theoretical predictions for the DTD can also be obtained from binary population synthesis (Ruiter et al., 2009, 2012; Toonen et al., 2012), where the stellar evolution of binary systems is followed until a possible SN Ia explosion. Ruiter et al. (2009) conclude that the double degenerate scenario should be the dominant channel for generating SNe Ia in spiral galaxies. More recently, in conjunction with the violent merger model (Pakmor et al., 2010, 2012b), Ruiter et al. (2012) find that the brightness distribution and the DTD may agree with observations, thus favoring the double degenerate scenario.

The double degenerate scenario is further supported by the fact that no surviving companion star has been identified so far. In the single degenerate scenario, the companion star should survive the explosion with a characteristic velocity, rotation and spectrum (Marietta et al., 2000; Pakmor et al., 2008; Wang & Han, 2010; Liu et al., 2012). But up to now, searches for the surviving companion of Tycho's supernova, e.g., remain unclear (Ruiz-Lapuente et al., 2004; Kerzendorf et al., 2009). Another supernova remnant, SNR 0509-67.5, also shows no sign of a surviving companion star (Schaefer & Pagnotta, 2012; Ruiz-Lapuente, 2012).

On the other hand, the detection of circumstellar material from the companion star would support the single degenerate scenario. In some cases, variable absorption of the Na I D line has been detected (Patat et al., 2007) and interpreted as being caused by circumstellar material probably stemming from a red giant companion. Another indication of circumstellar material was found by Sternberg et al. (2011), who detect blue-shifted lines in 35 SNe Ia and conclude that these originate from mass outflows in single degenerate systems. They estimate the fraction of SNe Ia in spiral galaxies to be

at least 20% to 25%. Recently, indications of circumstellar material have also been found directly in the spectra of PTF 11kx (Dilday et al., 2012).

The picture of SNe Ia progenitor systems emerging in the last few years seems to combine different progenitor system in order to explain the diversity of Type Ia supernovae. Different progenitor channels may contribute to normal SNe Ia and also explain the diverse peculiar subtypes.

1.4 Impacts on Other Research Fields

One research field where Type Ia supernovae play an important role is the chemical evolution of galaxies. Because the explosion ejecta move with high velocities up to 20 000 km/s into the interstellar space, SNe Ia are a major source of distributing heavy elements in galaxies, together with core collapse supernovae. As an example, a large mass up to $1 M_{\odot}$ of ^{56}Ni is produced in a SN Ia, which subsequently decays to stable ^{56}Fe . It is assumed that a large fraction of stable iron in the galaxy is contributed by SNe Ia (55% of IGE, Iwamoto et al., 1999). Furthermore, the chemical composition of the solar system is well known and can be used to infer constraints on SN Ia explosion models (Iwamoto et al., 1999) and SN Ia delay-time distributions (Kobayashi & Nomoto, 2009).

As SNe Ia can be used as standardizable candles, they allow distance measurements in the Universe. With this method, it could be shown that the expansion of the Universe is accelerating (Perlmutter et al., 1997, 1999; Riess et al., 1998; Schmidt et al., 1998). This fascinating discovery was awarded with the physics Nobel Prize in 2011.

1.5 Previous Work

The microscopic properties of nuclear burning fronts in degenerate carbon/oxygen matter have been subject to studies in the past: Khokhlov (1988) computes parameters of combustion waves—deflagrations and detonations—for different initial compositions (He, different C/O mixtures). Calculated are for example the propagation speed, the energy release and the maximum temperature.

The propagation of deflagration fronts, driven by conduction, has been examined in more detail for different initial compositions with different methods in Timmes & Woosley (1992). They compute the speed, width and density structure of one-dimensional laminar burning fronts.

More details on the structure of detonation waves are given by Khokhlov (1989). Properties of one-dimensional, steady planar detonation waves are calculated, such as propagation velocities and the thickness of the detonation wave. The calculations are done for different C/O mixtures. It is also found that detonation waves in degenerate C/O matter is of the pathological type at higher densities instead of the Chapman-Jouguet type. This work was extended by Gamezo et al. (1999), where properties of one-dimensional detonation fronts are calculated also for the pathological case, but only for a equal-by-mass C/O mixture. Additionally, they find that two-dimensional simulations show a cellular pattern similar to terrestrial detonations. The pathological

structure of the detonation wave is further investigated by Sharpe (1999), who calculates the full structure of the detonation wave, also behind the pathological point.

The effect of different progenitor compositions on SN Ia explosion models has been studied by Höflich et al. (1998) for one-dimensional delayed detonation models. A depletion of carbon in their models led to a decrease in the ^{56}Ni production. Consequently, Umeda et al. (1999) state as a working hypothesis for explaining the variety of luminosities in SNe Ia, that larger carbon mass fractions should lead to a larger production of ^{56}Ni . The three-dimensional deflagration models of Khokhlov (2000) agree with this trend. In contrast to this, Röpke & Hillebrandt (2004) find in their three-dimensional models with a better modeling of the turbulent flame structure, that the amount of ^{56}Ni produced in the explosion does not strongly depend on the carbon-to-oxygen ratio. An extended study with more three-dimensional deflagration models supports this (Röpke et al., 2006a). Their conclusion that the carbon-to-oxygen ratio cannot account primarily for the variations in SNe Ia may be invalid, as pure deflagrations can probably not explain normal SNe Ia. This is supported by newer results by Kromer et al. (2012), who suggest that deflagration models cannot account for normal SNe Ia, but rather for subluminal 2002cx-like objects. Recent studies of 2D simulations (Kasen et al., 2009) and 3D simulations (Seitenzahl et al., 2012) of delayed detonation models show that delayed detonations of Chandrasekhar-mass WDs may explain Type Ia supernovae. Röpke et al. (2012) compare a delayed detonation model of a Chandrasekhar-mass WD and a violent merger of two sub-Chandrasekhar-mass WDs to the nearby SN 2011fe. They compare synthetic spectra to the observed spectrum and find, e.g., that the Si II line is blueshifted, meaning that the Si II moves at too high velocities. They speculate that this velocity could be less for a carbon depleted core because of the lower overall nuclear energy.

Therefore, this work examines the impact of a different carbon-to-oxygen ratio on delayed-detonation simulations in two and three dimensions.

1.6 Objectives of This Work

This work improves the modeling approach of the explosive stage of thermonuclear—i.e. Type Ia—supernovae by considering more realistic progenitor models. To this end, the impact of a different progenitor composition on thermonuclear flames is investigated. Because of the multi-scale character of the problem—the flame width is orders of magnitudes below the numerical resolution—the nuclear burning fronts are approximated as discontinuities in the level set approach. In this approach, the chemical composition behind the burning front is determined from tables, which are obtained in an iterative calibration procedure.

Using these tables, the impact of different compositions of the progenitor WD on large scale, multi-dimensional explosion simulations is examined. The model chosen here is the delayed detonation model of a Chandrasekhar-mass WD. The initial progenitor composition is also allowed to vary spatially according to newer results from stellar evolution theory.

The objectives of this diploma thesis are on the one hand to improve the explosion modeling by extending the involved physics. This is accomplished by taking into account different initial compositions as predicted from stellar evolution simulations. On the other hand, the agreement of these more realistic models with observations are tested. Firstly, the variability of the luminosities of normal SNe Ia should be reproduced by variations in the initial compositions. Secondly, the agreement of synthetic light curves and spectra obtained by radiative transfer calculations with observables is tested.

One expects for a realistic progenitor structure with a carbon depleted core that the kinetic energy of the ejecta decreases. This is caused by the higher binding energy of carbon compared to oxygen leading to a lower overall nuclear energy release. The lower kinetic energy then results in a red-shift of line velocities in the P-Cygni line profiles of the spectrum. As in current spectra of delayed detonation Chandrasekhar-mass models the line velocities for e.g. the Si II line are too high (cf. Röpke et al., 2012), this could improve the agreement between synthetic and observed spectra. Moreover, the whole dynamical evolution is expected to change because of the different burning front properties. Apart from this, the predictions for the size and detailed composition of the carbon depleted core show a certain variability. Thus, it is important to know if this variability may help to explain the diversity in luminosity of normal SNe Ia, which is important for distance measurements used in cosmology.

The outline of this diploma thesis is the following: Chapter 2 introduces the physical concepts which are important in this work. Chapter 3 explains the numerical methods used in the simulations. In Chapter 4, the results of the calibrations and large scale simulations of delayed detonation models are presented. Finally, in Chapter 5, conclusions are drawn from these results.

2 Physical Foundations

2.1 Hydrodynamics

At the heart of the numerical method used in this work lies the continuum assumption, that the medium consisting of individual particles is assumed to form a continuous fluid. This macroscopic fluid can then be described by the hydrodynamical Euler equations. The prerequisite for this assumption to be fulfilled is that the mean free path λ of the individual particles is small against the length scale L , over which important properties of the problem change significantly (Müller, 1998). If this is the case, the medium can be thought to consist of “fluid elements” being small compared to L but large compared to λ . These fluid elements contain matter being in local thermal equilibrium—which is reached by collisions of the individual particles on short length scales. Moreover, the small λ ensures that only a small fraction of the particles is scattered to neighbouring fluid elements.

The system under consideration, WD matter, can be approximated very well by the description of a fully ionized plasma with arbitrarily degenerate electrons, thus fulfilling the continuum assumption (Hillebrandt & Niemeyer, 2000).

2.1.1 Conservation Laws

The hydrodynamical equations can be derived either in a continuum approach (Landau & Lifschitz, 2007) or from statistical physics using the moments of the Boltzmann equation (Landau & Lifschitz, 1983; Shore, 2007). As the continuum approach is more instructive when looking at the numerical implementation, it is used to derive the basics of the hydrodynamical equations, similar to Röpke (2003).

The main hydrodynamical equations have the form of conservation laws. Given an extensive quantity Q in a fluid volume V , the quantity can be computed from the corresponding density $q(x, t)$ using

$$Q(t) = \iiint_V q(x, t) dV.$$

A change of this extensive quantity in time can only happen through surface fluxes, where part of the quantity is transported outside or inside the volume, or through the existence of sources or sinks inside the volume. This can be quantified as

$$\frac{dQ}{dt} = \frac{dQ_f}{dt} + \frac{dQ_s}{dt}, \quad (2.1)$$

where the first term gives the contribution by the flux and the second term the contribution by the sources.

The change caused by the flux is calculated by integrating the flux density \mathbf{j}_q over the surface of the volume V ,

$$\frac{dQ_f}{dt} = - \oint_{\partial V} \mathbf{j}_q(\mathbf{x}, t) \cdot d\mathbf{S} = - \iiint_V \nabla \cdot \mathbf{j}_q(\mathbf{x}, t) dV, \quad (2.2)$$

where the last equation follows from the divergence theorem, assuming the flux density \mathbf{j}_q to be differentiable.

The change in Q resulting from the sources inside the volume can be obtained by integrating the source density s_q over the volume V ,

$$\frac{dQ_s}{dt} = \iiint_V s_q(\mathbf{x}, t) dV. \quad (2.3)$$

Now combining equations (2.2) and (2.3) with equation (2.1) yields the integral form of the balance equation,

$$\frac{d}{dt} \iiint_V q(\mathbf{x}, t) dV = - \oint_{\partial V} \mathbf{j}_q(\mathbf{x}, t) \cdot d\mathbf{S} + \iiint_V s_q(\mathbf{x}, t) dV, \quad (2.4)$$

which does not require the functions q and \mathbf{j}_q to be differentiable.

If now the functions q and \mathbf{j}_q are differentiable, the differential form of the balance equation can be obtained from (2.4), using (2.2) and the fact that V is arbitrary,

$$\partial_t q(\mathbf{x}, t) + \nabla \cdot \mathbf{j}_q(\mathbf{x}, t) = s_q(\mathbf{x}, t). \quad (2.5)$$

As this differential form of the balance equation (2.5) cannot be applied to functions containing discontinuities, the integral form (2.4) is better suited for computing weak solutions. The integral formulation is also used in the discretization of our numerical method (see Section 3.1.3).

2.1.2 Reactive Euler Equations

In order to describe an ordinary fluid, balance equations are needed for mass, momentum and energy. In the system considered here, combustion processes play an important role, therefore balance equations for the mass fractions of the chemical species have to be added.

The balance equation for mass yields the *continuity equation*

$$\partial_t \rho + \nabla(\rho \mathbf{u}) = 0, \quad (2.6)$$

with ρ being the mass density and \mathbf{u} the fluid velocity. Concerning momentum, the corresponding balance equation is given by

$$\partial_t(\rho \mathbf{u}) + \nabla(\rho \mathbf{u} \otimes \mathbf{u}) = -\nabla p + \rho \mathbf{f}, \quad (2.7)$$

with an external force \mathbf{f} , which in our case will be the gravitational force derived from the gravitational potential $\mathbf{f} = \nabla\Phi$. The balance equation for the total energy e_{tot} can be written as

$$\partial_t(\rho e_{\text{tot}}) + \nabla(\rho e_{\text{tot}}\mathbf{u}) = -\nabla(p\mathbf{u}) + \rho\mathbf{u} \cdot \mathbf{f}. \quad (2.8)$$

In order to describe combustion processes resulting in varying chemical composition, the mass fractions \mathbf{X}^1 ($X_j = \rho_j/\rho$) are introduced for the N chemical species. A new set of balance equations describes for the coupling to the hydrodynamics,

$$\partial_t(\rho X_j) + \nabla(\rho\mathbf{u}X_j) = r_j(\rho, T, \mathbf{X}) \quad , j = 1, \dots, N, \quad (2.9)$$

where r_j is given by the reaction rate for species j ². The influence of the thermonuclear reactions on the energy in the medium is expressed as an additional source term $s(\mathbf{r})$ in the energy balance equation,

$$\partial_t(\rho e_{\text{tot}}) + \nabla(\rho e_{\text{tot}}\mathbf{u}) = -\nabla(p\mathbf{u}) + \rho\mathbf{u} \cdot \mathbf{f} + \rho s(\mathbf{r}), \quad (2.10)$$

the source term $s(\mathbf{r})$ depending on the nuclear reaction rates.

This set of equations is closed by the equation of state, which relates temperature and pressure to density, internal energy and composition,

$$\begin{aligned} T &= T_{\text{eos}}(\rho, e_i, \mathbf{X}), \\ p &= p_{\text{eos}}(\rho, e_i, \mathbf{X}). \end{aligned} \quad (2.11)$$

The details of the equation of state of white dwarf matter are given in Section 2.5.

The equations presented so far describe an ideal fluid consisting of N reacting species under the influence of an external force \mathbf{f} , which in our application is given by the gravitational force.

To account for the properties of real fluids, an extension of these equations is necessary. Important physical effects to be included are viscosity (leading to the Navier-Stokes equations), thermal and chemical diffusion. These effects are crucial to the theoretical understanding of the microscopic properties of flame propagation in SNe Ia. But as these effects are neglected in the numerical implementation for our large scale simulations—for reasons given in Section 3.1.3—the resulting equations will not be given here.

2.1.3 Instabilities

During the course of a SN Ia, several hydrodynamical instabilities may occur, depending on the channel. The most important instabilities occur during the deflagration phase—the Rayleigh-Taylor and Kelvin-Helmholtz instabilities.

¹Note that \mathbf{X} denotes a vector in the N -dimensional space of chemical species, not in ordinary space. The same holds for the rates \mathbf{r} .

²Due to the additional constraint of particle conservation, $\sum_j X_j = 1$, not all of the equations (2.9) are independent. One way of dealing with this problem is solving for $(N - 1)$ species, computing the last species via conservation of the particle number. A numerically more stable solution is mentioned in Müller (1998).

The *Rayleigh-Taylor* instability is caused by an inverted density profile in a gravitational field. If a fluid layer of high density is located in the direction of lower gravitation (“above”) compared to a fluid layer of lower density, the front separating the two layers develops an instability. This is caused by buoyancy driving material from the lower layer up, thereby forming characteristic, mushroom-shaped fingers. As linear stability analysis shows (e.g. Shore, 2007), this instability forms for any layered fluid system with a density inversion.

In SNe Ia, this density inversion is reached in the deflagration phase. The burnt material in a deflagration has a lower density and pressure than the initial, unburnt fuel (compare Section 2.3). As the deflagration is initiated near the center of the WD, burnt material with low density is generated near the center, thus giving rise to Rayleigh-Taylor instabilities.

In contrast to the Rayleigh-Taylor instability, the *Kelvin-Helmholtz* instability is not driven by buoyancy, but by shear. Given two fluid layers with a relative velocity between them, a perturbation at the boundary layer causes one fluid to stream around it. This results locally in a lower pressure, thus enhancing the perturbation. As the situation is symmetric, the same process happens in the other layer, leading to the generation of a vortex sheet. This is an important mechanism for creating turbulence. Again, linear stability analysis (Shore, 2007) can show that this instability can even occur in layers with the same density being in relative movement to each other.

The Kelvin-Helmholtz instability appears as a secondary instability in SNe Ia, accompanying Rayleigh-Taylor instabilities while forming mushroom-shaped fingers.

Another example for the occurrence of these instabilities are the mushroom clouds resulting from explosions on Earth, where hot ashes are driven up into the colder and denser atmosphere.

2.2 Nuclear Reactions

2.2.1 Nuclear Reaction Networks

In order to compute detailed nucleosynthetic abundances—for example the rates in equation (2.9)—a nuclear reaction network has to be employed. This is a large set of non-linear, coupled ordinary differential equations connecting the abundances of different species through nuclear reactions. The nuclear reactions can be classified by the number of nuclei participating in the reaction into one-body, two-body and three-body reactions. Important one-body reactions are weak reactions like β decay and electron capture, but also photo-disintegration. Two-body reactions contain most strong reactions, where two nuclei take part. Because of statistical reasons, three-body reactions are usually very slow and thus not as important as the other reactions. The most important three-body reaction, however, is the triple- α reaction $3(^4\text{He}) \rightarrow ^{12}\text{C} + \gamma$.

The change in the specific abundances $Y_i = X_i/A_i$, where A_i is the atomic number of species i , can be expressed as (Müller, 1998)

$$\dot{Y}_i = \sum_j c_i(j) \lambda_j Y_j + \sum_{j,k} c_i(j,k) \rho N_A \langle jk \rangle Y_j Y_k + \sum_{j,k,l} c_i(j,k,l) (\rho N_A)^2 \langle jkl \rangle Y_j Y_k Y_l, \quad (2.12)$$

where the three terms describe one-body, two-body and three-body reactions, respectively. λ_j is the one-body reaction rate (β decay, electron capture, photo disintegration) and $\langle jk \rangle$ and $\langle jkl \rangle$ denote averaged products of cross section and relative velocity. The statistical factors c_i avoid multiple counting of rates and are given by (Müller, 1998)

$$c_i(j) = \pm N_i, \quad c_i(j, k) = \pm \frac{N_i}{N_j! N_k!} \quad \text{and} \quad c_i(j, k, l) = \pm \frac{N_i}{N_j! N_k! N_l!}. \quad (2.13)$$

Here, the numbers N_i denote the total number of nuclei of species i in the corresponding reaction and the sign denotes production (+) or destruction (−) of the nucleus of kind i .

2.2.2 Nuclear Statistical Equilibrium

At temperatures above about 2×10^9 K and corresponding densities, the strong reactions between the isotopes become very fast, thereby establishing a statistical equilibrium—also called nuclear statistical equilibrium (NSE). The problem of calculating the equilibrium of a set of chemical reactions is basically one of statistical physics. An overview of the equations as well as computations for 333 parameter values can be found in Clifford & Tayler (1965).

The basic assumption is that there is an equilibrium reaction between a nucleus with Z protons and $A - Z$ neutrons and the free protons and neutrons,



which is reached over several intermediate reactions like for example ${}^A Z(\gamma, p) {}^{A-1}(Z-1)$, ${}^A Z(\gamma, n) {}^{A-1}Z$, $\alpha(\gamma, 2n) 2p$ etc. The equilibrium condition for reaction (2.14),

$$\mu_i = Z_i \mu_p + (A_i - Z_i) \mu_n, \quad (2.15)$$

relates the chemical potential μ_i of nucleus i to the chemical potentials of protons μ_p and neutrons μ_n . Under the given thermodynamic conditions the nuclei can be approximated with a Maxwell-Boltzmann distribution. The specific abundance Y_i for the species i in equilibrium can then be computed as (see standard textbooks on statistical physics, e.g. Reichl, 2009)

$$Y_i = \frac{\rho A_i}{m_i} \left(\frac{m_i kT}{2\pi \hbar^2} \right)^{3/2} \omega_i \exp \left(\frac{\mu_i - m_i c^2}{kT} \right), \quad (2.16)$$

where m_i is the mass of nucleus i and $\omega_i = \sum_r (2J_r^{(i)} + 1) \exp(-\frac{\varepsilon_{i,r}}{kT})$ is the statistical weight (the sum extends over all energy states r with energy $\varepsilon_{i,r}$ and spin $J_r^{(i)}$).

Combining Equation (2.15) with Equation (2.16) yields the basic equation

$$Y_i = Y_p^{Z_i} Y_n^{(A_i - Z_i)} \frac{\omega_i A_i^{3/2}}{2^{A_i}} \cdot \left(\frac{\rho}{m_p} \right)^{\frac{3(A_i - 1)}{2}} \exp \left(\frac{(Z_i m_p + (A_i - Z_i) m_n - m_i) c^2}{kT} \right), \quad (2.17)$$

where $m_i = A_i m_p$ was assumed. This assumption is fulfilled for heavy isotopes with an error of about 1%. In addition to these $N - 2$ equations, two more conditions allow for

the computation of two independent variables, namely the conservation of the baryon number,

$$\sum_i A_i Y_i = 1, \quad (2.18)$$

and—as the weak processes happen on much longer time scales—the condition for the electron fraction Y_e ,

$$\frac{\sum_i Z_i Y_i}{\sum_i A_i Y_i} = Y_e. \quad (2.19)$$

This set of equations is then usually solved at given temperature, density and electron fraction for the chemical potentials of protons μ_p and neutrons μ_n . This allows for the subsequent computation of all other specific abundances Y_i using Equation (2.17). Computations spanning a density range from $1 \times 10^4 \text{ g/cm}^3$ to $1 \times 10^8 \text{ g/cm}^3$ and a temperature range from $2 \times 10^9 \text{ K}$ to $8 \times 10^9 \text{ K}$ for several Y_e have already been done in the 1960s by Clifford & Tayler (1965).

2.3 Combustion Physics

The combination of hydrodynamics and thermonuclear reactions gives rise to a vast range of phenomena reaching from violent burning in detonations to quiet hydrostatic burning as it occurs in the interior of stars. In the context of SNe Ia explosions, the two most important burning modes are detonations and deflagrations.

2.3.1 Simple Theory

The simplest theory of burning fronts (e.g. Landau & Lifschitz, 2007) is understood quite well, especially for detonations. The assumptions for the simplified treatment are that the wavefront is a one dimensional plane, that the flow through the burning front is steady and that the reaction zone is thin.

As an approximation, the burning front can then be regarded as a hydrodynamical discontinuity or shock. If we now look at the reference frame where this discontinuity is at rest, let the unburnt material (density ρ_0 , temperature T_0 and composition \mathbf{X}_0) stream into the shock with a velocity D and the burnt material (density ρ , temperature T and composition \mathbf{X}) come out with velocity u . The pressure p and the internal energy e_i are given by the equation of state (compare Equation (2.11)). The total energy e_{tot} is given by

$$e_{\text{tot}}(\rho, T, \mathbf{X}) = e_i(\rho, T, \mathbf{X}) - q(\mathbf{X}), \quad (2.20)$$

taking into account the binding energy $q > 0$. Integration of the one dimensional hydrodynamical equations over the discontinuity shows that mass flux (2.21), momentum flux (2.22) and energy flux (2.23) are conserved (Landau & Lifschitz, 2007),

$$\rho_0 D = \rho u, \quad (2.21)$$

$$p(\rho_0, T_0, \mathbf{X}_0) + \rho_0 D^2 = p(\rho, T, \mathbf{X}) + \rho u^2, \quad (2.22)$$

$$e_{\text{tot}}(\rho_0, T_0, \mathbf{X}_0) + \frac{p(\rho_0, T_0, \mathbf{X}_0)}{\rho_0} + \frac{D^2}{2} = e_{\text{tot}}(\rho, T, \mathbf{X}) + \frac{p(\rho, T, \mathbf{X})}{\rho} + \frac{u^2}{2}. \quad (2.23)$$

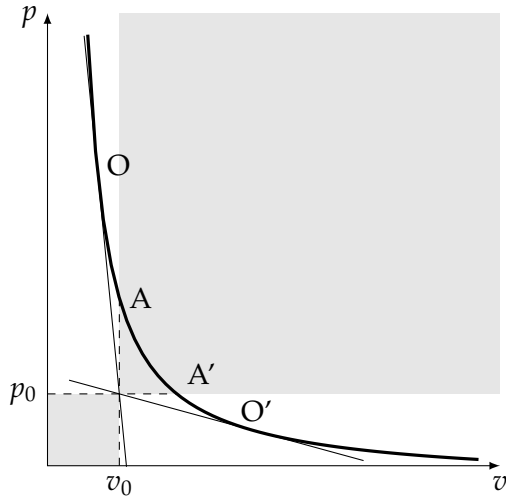


Figure 2.1 | Jump conditions for burning fronts. Shown is the Hugoniot adiabat (2.25) with the two tangent Rayleigh lines determining the Chapman-Jouguet points O and O'. For a discussion of the different intervals, see Equation (2.26) and the following paragraphs. The gray area symbolizes unphysical end states. This figure is similar to Landau & Lifschitz (2007, Figure 136), but was computed for a polytropic equation of state with $\gamma = 5/3$.

These equations can be combined to the Rankine-Hugoniot jump conditions, namely the Rayleigh line,

$$\mathcal{R}(p, v) = p - p_0 + \frac{D^2}{v_0^2}(v - v_0) = 0, \quad (2.24)$$

here parametrized by pressure p and specific volume $v = \frac{1}{\rho}$, and the Hugoniot adiabat,

$$\mathcal{H}(p, v) = e_i - e_{i,0} + \Delta q + \frac{1}{2}(p + p_0)(v - v_0) = 0, \quad (2.25)$$

where $\Delta q = q_0 - q$ denotes the reaction energy release.

These conditions can now be analyzed in the p - v -plane (compare Figure 2.1), following Landau & Lifschitz (2007). As the final state has to fulfill the Rankine-Hugoniot conditions, its representation in the p - v -plane has to be on the Rayleigh line as well as on the Hugoniot adiabat. From the point of the initial conditions p_0 and v_0 , several lines divide the Hugoniot adiabat in five interesting regions: the vertical and horizontal lines (leading to A and A') as well as the tangents to the adiabat (leading to O and O'). The interval between A and A' (with $p > p_0$ and $v > v_0$) is unphysical because the mass flux here would be imaginary.

As Landau & Lifschitz (2007) show, the velocities of the unburnt material, D , and of the burnt material, u , fulfill the inequalities

$$\begin{aligned} \text{above O:} & \quad D > c_0, \quad u < c; \\ \text{between A and O:} & \quad D > c_0, \quad u > c; \\ \text{between A' and O':} & \quad D < c_0, \quad u < c; \\ \text{below O':} & \quad D < c_0, \quad u > c, \end{aligned} \quad (2.26)$$

where c_0 and c are the speed of sound in the unburnt and burnt material, respectively.

The regime of *detonations* lies above O, where the burning front propagates supersonically with respect to the unburnt material. In this case, the hydrodynamical shock heats the unburnt fuel, thus crossing the burning threshold of the fuel.

Between A and O, burning occurs that is not like a detonation, but still propagates supersonically due to high heat conduction (Landau & Lifschitz, 2007). Fickett & Davis (1979) use the term “strong detonations” for the region above O and “weak detonations” for the interval between A and O. There, it is also stated that “strong detonations” correspond to boundary conditions with a piston driving the detonation, whence they are also called “overdriven detonations”. More details on detonations are given in Section 2.3.2.

The solution at the points O and O', where $u = c$ (i.e. the motion behind the front is sonic), are called Chapman-Jouguet solutions. For a self-sustained detonation, it is the physical solution (Landau & Lifschitz, 2007).

The interval between A' and O' belongs to *deflagrations*, which are slow burning fronts propagating subsonically. The physical mechanism differs from detonations in that the key process here is thermal diffusion. Heat is being transferred from the burning flame to the cold, unburnt material, which is thus heating up to the point where burning can start. Deflagrations are described in more detail in Section 2.3.3.

Below O', no stable burning front can emerge, because an absolute instability occurs under the conditions given here. This is described in more detail in Landau & Lifschitz (2007).

An important difference between detonations and deflagrations can be seen from Figure 2.1 and Equation (2.26): For detonations, the pressure in the burnt material increases ($p > p_0$), the specific volume decreases ($v < v_0$, equivalent to $\rho > \rho_0$) and the velocity decreases as well ($u < D$). This means that after the burning, the material is compressed and moves in the direction of the burning front. In contrast to this, for deflagrations, there is a pressure decrease ($p < p_0$), an increase in specific volume ($v > v_0$) and velocity ($u > D$). Here, the burnt material is not compressed, but rarefied, and moves in the opposite direction as the front in the rest frame of the unburnt material.

2.3.2 Detonations

A detailed view of the jump conditions for detonations is shown in Figure 2.2. The physical mechanism can in this simple theory be understood as follows (compare Landau & Lifschitz, 2007; Fickett & Davis, 1979): The initial point a at (v_0, p_0) has to be connected to the final state which corresponds to a point on the Hugoniot adiabat. The Chapman-Jouguet solution corresponds to the point O in Figure 2.2. In order to reach this state, the matter is first compressed by a hydrodynamical shock wave and moves up to the point e. This results in heating of the material, thus allowing for nuclear burning. The final state O is reached by following the Rayleigh line. The same can be said for strong detonations: First, the hydrodynamical shock wave brings the system from a to d, and after the burning it moves down the Rayleigh line to the final point c. As this configuration is stable, the point b cannot be reached by this mechanism. Thus, “weak detonations” corresponding to points below O are not explained by this mechanism and consequently are not really “detonations”.

This model with the assumption of a finite reaction rate, where the reaction is separated from the hydrodynamical shock, extends the simplest theory and is usually called

Zeldovich-von Neumann-Döring theory or ZND theory. The ZND theory is explained extensively in Fickett & Davis (1979). The model assumes that the hydrodynamical shock is much thinner than the reaction zone and can thus be modeled by a discontinuity. This discontinuity is then followed by an extended reaction zone. The separation of chemical reactions and the hydrodynamical shock is justified since many collisions occur at the shock front establishing mechanical equilibrium but a much smaller number of collisions lead to chemical reactions. The basic assumptions of the theory can be summarized as follows (Fickett & Davis, 1979): There is a one-dimensional flow with the shock being modeled as a hydrodynamical discontinuity because microscopic transport effects—e.g. conduction, viscosity, diffusion—are neglected. The reaction starts exactly at the shock and all variables besides the chemical composition are in local thermal equilibrium. Now, these assumptions lead to a steady one dimensional flow. In this physical picture, the intervals in Figure 2.2 from d to c and from e to O can now be interpreted as the chemical reaction progressing from the hydrodynamical shock (d; e) to its final state (c; O). Each point on these intervals of the Rayleigh lines also belong to Hugoniot adiabates corresponding to partial reactions down to the Hugoniot adiabetic of the final state.

The detailed structure of the reaction zone can be obtained by integrating the one-dimensional, steady version of the reactive Euler equations (2.6), (2.7), (2.10) and (2.9) together with the equation of state (2.11). Using thermodynamic, differential relations for the pressure p and energy e , the reactive Euler equations can be written as (Khokhlov, 1989; Sharpe, 1999)

$$\frac{d\rho}{dx} = \frac{\rho c_f^2}{u} \frac{\sigma \cdot r}{u^2 - c_f^2}, \quad (2.27)$$

$$\frac{dT}{dx} = \left(\frac{\partial p}{\partial T} \right)_{T,Y}^{-1} \left\{ \left[u^2 - \left(\frac{dp}{d\rho} \right)_{T,Y} \right] \frac{d\rho}{dx} - \frac{dp}{dY} \cdot \frac{dY}{dx} \right\}. \quad (2.28)$$

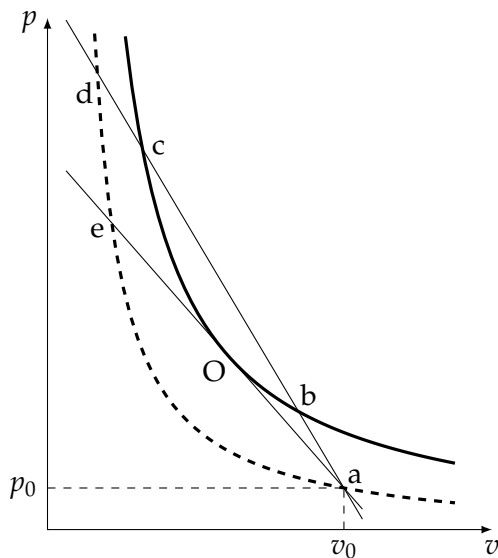


Figure 2.2 | Jump conditions for the detonation branch. Shown is the Hugoniot adiabetic (2.25) (thick, solid) and the shock adiabetic for $\Delta q = 0$ (thick, dashed). Moreover, the Rayleigh lines corresponding to a Chapman-Jouguet detonation and to a detonation with higher velocity are plotted. The points a to e are explained in the text. This figure is similar to Landau & Lifschitz (2007, Figure 132) and displays just another sector of Figure 2.1, although with a different scaling of the axes.

Additionally, the coupling to the chemical reactions is given by (compare Equation (2.9))

$$\frac{d\mathbf{Y}}{dx} = \frac{\mathbf{r}}{u}. \quad (2.29)$$

The rates \mathbf{r} can be computed with a nuclear network as given in Equation (2.12). Here, c_f is the frozen sound speed at constant chemical composition,

$$c_f^2 = \left(\frac{dp}{d\rho} \right)_{s,Y} = \left(\frac{\partial p}{\partial \rho} \right)_{T,Y} + \frac{T}{\rho^2} \left(\frac{\partial p}{\partial T} \right)_{\rho,Y}^2 \left(\frac{\partial e}{\partial T} \right)_{\rho,Y}^{-1}, \quad (2.30)$$

and $\sigma \cdot \mathbf{r}$ the thermicity, which can be interpreted as the heat release function (Fickett & Davis, 1979) with

$$\sigma = \frac{1}{\rho c_f^2} \left\{ \left(\frac{\partial p}{\partial \mathbf{Y}} \right)_{\rho,T,Y_i} - \left[\left(\frac{\partial e}{\partial \mathbf{Y}} \right)_{\rho,T,Y_i} - \left(\frac{\partial q}{\partial \mathbf{Y}} \right)_{Y_i} \right] \left(\frac{\partial p}{\partial T} \right)_{\rho,Y} \left(\frac{\partial e}{\partial T} \right)_{\rho,Y}^{-1} \right\} \quad (2.31)$$

being the thermicity coefficients.

In order to compute the reaction zone structure, first, the state behind the hydrodynamical shock, being a discontinuity, is obtained from the Rankine-Hugoniot jump conditions, equations (2.24) and (2.25). This also gives a relation between the fluid velocity u and the detonation propagation speed D :

$$u = \frac{\rho_0}{\rho} D. \quad (2.32)$$

Now, giving D as an initial value, and thus u , according to Equation (2.32), the structure of the reaction zone is obtained by integrating equations (2.27), (2.28) and (2.29) from the post-shock state into the reaction zone. For the Chapman-Jouguet state, the fluid velocity u is determined by the equilibrium speed of sound, $u = c_e$, where (Fickett & Davis, 1979)

$$c_e^2 = \left(\frac{\partial p}{\partial \rho} \right)_{s,\Delta f=0} = c_f^2 \left\{ 1 - c_f^2 \sigma \cdot \phi^{-1} \cdot \sigma \right\}. \quad (2.33)$$

Here, $\Delta f = (\partial f / \partial \mathbf{Y})_{T,\rho}$ denotes the change of the free energy f with the composition, which is zero in chemical equilibrium. The elements of the matrix ϕ are given by $\phi_{ij} = (\partial^2 f / (\partial Y_i \partial Y_j))_{T,\rho}$. Perturbations which have high frequencies propagate with the frozen sound speed, as the chemical equilibrium (NSE in this case) cannot be established since the nuclear reactions are too slow to adapt to the new density and temperature. Perturbations with lower frequencies, on the other hand, travel with the equilibrium sound speed, as the chemical equilibrium is established faster than density and temperature vary. In the ZND theory, the fluid velocity should equal the equilibrium sound speed because NSE is established at the end of the reaction zone. The difference between these sound speeds is also discussed in Khokhlov (1988) in the context of detonations in degenerate C/O matter.

If at some point in the reaction zone a frozen sonic point occurs with $u = c_f$ and $\sigma \cdot \mathbf{r}$ at the same time, the detonation is of the pathological type (Fickett & Davis, 1979;

Khokhlov, 1989; Sharpe, 1999). This can lead to higher detonation propagation velocities (Sharpe, 1999). The cause for this pathological nature of the detonation is an endothermic reaction.

All these one-dimensional theories may only be seen as an averaged description of the real, multi-dimensional structure of the wave front. Since the detonation wave front undergoes certain instabilities, a cellular pattern behind the front emerges (Fickett & Davis, 1979). The propagation of the front is ensured by transverse waves behind the incident shock.

Application to SNe Ia

In the context of Type Ia supernovae, the simple theory using the Rankine-Hugoniot conditions was applied by Khokhlov (1988) to detonations in degenerate carbon/oxygen matter as found in white dwarfs. There, the Chapman-Jouguet propagation velocities and Hugoniot adiabates are calculated for different compositions. The ZND theory was applied by Khokhlov (1989) to detonation waves in thermonuclear supernovae. The structure of the wavefront is computed for an equal-by-mass C/O composition, taking the pathological nature of the detonation into account. This pathological nature of the detonation results from the NSE relaxation being endothermic at densities $\gtrsim 10^7 \text{ g/cm}^3$ (Khokhlov, 1989). As Khokhlov (1989) was not able to continue the solution for the detonation wave structure behind the frozen sonic point, his solution ends there. Khokhlov (1989) also finds that the reaction zone consists of three separated burning stages: carbon burning, oxygen burning and silicon burning to NSE.

This was examined by Sharpe (1999), where for an equal-by-mass mixture of C/O the complete structure of the detonation reaction zone is computed. The pathological point is determined via a bisection method, reaching either a zero thermicity point or a frozen sonic point. The solution is then continued using a linearization around the pathological point.

The reaction zone structure was also computed by Gamezo et al. (1999), giving the detonation propagation speeds depending on the density for an equal-by-mass C/O composition, which for higher densities may be larger as the Chapman-Jouguet detonation speeds by a maximum of roughly 6%. They also compute the reaction zone lengths for the different burning stages and find that the silicon burning length gets larger than the WD at low densities. At very low densities, even the oxygen burning length may be larger than the size of the WD. Moreover, using two-dimensional time-dependent simulations of the reactive Euler equations, Gamezo et al. (1999) were able to find cellular patterns at the carbon, oxygen and silicon scales, which are similar to the patterns found in terrestrial detonations (Fickett & Davis, 1979).

2.3.3 Deflagrations

For deflagrations, the maximum propagation velocity is reached at the Chapman-Jouguet point O' (Figure 2.1). For degenerate C/O matter, the deflagration speeds according to the Rankine-Hugoniot conditions, equations (2.24) and (2.25), have been calculated by

Khokhlov (1988). As already noted there, the propagation of deflagration fronts in white dwarfs are affected by the Rayleigh-Taylor instability (compare Section 2.1.3), which leads to an increase in the flame surface and hence to a faster propagation.

The propagation of deflagration flames is further studied in Timmes & Woosley (1992) with several methods. They compute the laminar flame speed for different compositions and give the following, fitting formula for the propagation speed:

$$v_{\text{lam}} = 92.0 \left(\frac{\rho}{2 \times 10^9} \right)^{0.805} \left(\frac{X(^{12}\text{C})}{0.5} \right)^{0.889} \text{ km/s} \quad (2.34)$$

Further, the acceleration of the flame by the Rayleigh-Taylor instability inducing turbulence is discussed. If the thickness of the burning front, λ_{max} , is much larger than the minimum instability wavelength, λ_{min} , the flame surface will become wrinkled with the deformation lengths being in between these two lengths. This results in a higher surface of the flame and an increase in the fractal dimension of the flame D , thus accelerating the flame. Timmes & Woosley (1992) use

$$v_{\text{eff}} = v_{\text{lam}} \left(\frac{\lambda_{\text{max}}}{\lambda_{\text{min}}} \right)^{D-2} \quad (2.35)$$

as an estimate for the effective turbulent velocity v_{eff} , where the fractal dimension is assumed to lie between 2 and 2.7. For turbulent flames, the fractal dimension is expected to lie between 2.3 and 2.36 (Niemeyer & Woosley, 1997).

As found by Damköhler (1940), the turbulent propagation of the deflagration flame decouples from the laminar burning speed and is dominated by the properties of the turbulence. More sophisticated, three-dimensional simulations using subgrid-scale modeling of turbulent effects showed that the propagation velocity is dominated by the turbulent velocity fluctuations (Niemeyer & Hillebrandt, 1995; Reinecke et al., 1999b) induced by the Rayleigh-Taylor and Kelvin-Helmholtz instabilities. This subgrid-scale modeling has been refined by Schmidt et al. (2006a,b). For more details on the numerical implementation, see Section 3.1.3.

2.3.4 Deflagration-Detonation Transition

It is known from terrestrial experiments, that turbulent deflagration flames may turn into detonation waves under certain circumstances (Clavin, 2004, and references therein). The main reason for this deflagration-detonation transition (DDT) to occur lies in the emergence of temperature gradients in hot spots, triggering the detonation.

The idea that the turbulent deflagration flame may undergo such a DDT in Type Ia supernovae was introduced by Blinnikov & Khokhlov (1986) and modeled in one-dimensional simulations by Khokhlov (1991a,c,b). The delayed detonation model (see also Section 1.3.1), where the burning starts as a subsonic deflagration and then turns into a supersonic detonation, could cure some of the shortcomings of pure detonation and pure deflagration models. On one hand, the produced mass of ^{56}Ni is enough to explain normal SNe Ia due to the detonation, on the other hand, a sufficient amount

of IME are produced since the WD is pre-expanded by the initial deflagration. The reason for the DDT to occur lies in the formation of pre-heated hot spots in the fuel with temperature gradients, similar to terrestrial experiments. Mechanisms leading to such hot spots may be the pre-compression ahead of the deflagration wave, the mixing of hot ashes with cold fuel in turbulent flames or shock heating (Khokhlov, 1991a).

That detonations may form in such hot spots was confirmed in one-dimensional hydrodynamical simulations by Niemeyer & Woosley (1997), Röpke et al. (2007) and Seitenzahl et al. (2009). There, the critical parameters are determined which are needed for a successful initiation of a detonation in degenerate C/O matter.

In more recent studies, the most probable mechanism for hot spots to emerge is assumed to be the mixing of heat from the hot ashes into the cold fuel (Niemeyer & Woosley, 1997; Röpke, 2007; Woosley, 2007; Woosley et al., 2009). This occurs as the turbulent flame changes from the flamelet regime to the distributed regime. In the flamelet regime, which governs the flame evolution during the largest part of the explosion, the internal flame structure is not affected by turbulence, only the large-scale structure. This is because the Gibson scale is larger than the flame width, where the Gibson scale is defined as the length scale, where the velocity fluctuations caused by turbulence are equal to the laminar burning speed. Thus, the deflagration flame burns faster through turbulent eddies below the Gibson scale than these can affect the internal structure (e.g. Röpke, 2007). If now the density decreases, as occurring during a deflagration in a WD, where the material is expanded during the flame evolution, the Gibson scale also decreases, whereas the flame width increases (Röpke, 2007). This marks the transition to the distributed burning regime, where the internal wave structure is distorted by turbulent eddies. This allows hot ashes and cold fuel to be mixed, which is not possible in the flamelet regime.

The distributed flame width has further to become comparable to the largest turbulent eddies, which restricts the density range where a DDT may occur to $(0.5 - 1.5) \times 10^7 \text{ g/cm}^3$ (Woosley, 2007). Moreover, large turbulent velocity fluctuations $\gtrsim 10^8 \text{ cm/s}$ are necessary in order to ensure strong mixing between ashes and fuel (Lisewski et al., 2000). That these occur with probabilities high enough to trigger a detonation was confirmed in three-dimensional simulations by Röpke (2007).

Woosley et al. (2009) give a more detailed discussion of the distributed burning regime, and conclude that a DDT may occur in this regime, when high velocity fluctuations are present due to turbulence.

The numerical implementation of the DDT criterion employed in the simulations is discussed in Seitenzahl et al. (2012) and Ciaraldi-Schoolmann et al. (2012) (see also Section 3.1.3).

2.4 Progenitor Evolution

2.4.1 Binary Pre-Supernova evolution

Since in this work simulations of delayed detonations of Chandrasekhar-mass WDs are carried out, the discussion of the evolution of the progenitor system focuses on these

systems. White dwarfs are born on average with a mass of about $0.6 M_{\odot}$ (Homeier et al., 1998), which means that they have to undergo a binary evolution phase in order to reach the Chandrasekhar mass of about $1.4 M_{\odot}$, as WDs in single systems are stable and simply cool down due to radiation.

The WD grows to the Chandrasekhar mass by accreting material from a non-degenerate companion star (Whelan & Iben, 1973; Nomoto, 1982), which can be a main-sequence star, a helium star, a subgiant or a giant. For a detailed discussion and more references, see Hillebrandt & Niemeyer (2000). The problem with this model is that most of the accretion rates do not lead to a stable mass transfer. If the accretion rate of hydrogen is too low, nova eruptions may occur, blasting away more mass than accreted before. If the accretion rate is higher, a degenerate layer of helium forms at the surface of the WD, which might detonate and thus give rise to novae. At an even higher accretion rate, hydrogen and helium may burn hydrostatically to a C/O mixture, which means that stable mass transfer is established. But some of these systems might also correspond to symbiotic or cataclysmic binaries (Hillebrandt & Niemeyer, 2000). If the accretion rate is too high, a H-rich envelope would form around the WD, whose existence is not seen in spectra of SNe Ia.

One can thus conclude that there is only a narrow parameter space of mass accretion allowing for stable burning of the accreted matter, hence increasing the WD mass to the Chandrasekhar mass. This parameter space might be larger for very low metallicities, as a recent study by Shen & Bildsten (2007) suggests.

Binary systems being home to nova explosions may also be SN Ia progenitor systems (e.g. Moore & Bildsten, 2012). A nova is a thermonuclear runaway in the accreted H shell of a WD and may occur in short and long period binaries. The short period binaries may be cataclysmic variables, where the mass transfer is achieved by Roche lobe overflow of the companion star. The long period binaries may be explained by symbiotic systems, where the WD accretes the material from the wind of the companion star, which is probably a red giant star (Hachisu et al., 1999). Another promising channel may be supersoft X-ray sources (e.g. Han & Podsiadlowski, 2004).

The recent discovery of circumstellar material (CSM) in SNe Ia (e.g. in PTF11kx, Dilday et al., 2012; or from Na lines, Sternberg et al., 2011) supports the SD scenario, as CSM is not supposed to be present in DD systems.

2.4.2 Pre-Ignition Phase

Prior to ignition, when the WD nearly reaches the Chandrasekhar mass, the accretion increases the temperature and density of the WD until carbon fusion begins (Hillebrandt & Niemeyer, 2000; Lesaffre et al., 2006). In the beginning, the carbon burning rates will be slow and thus the fusion energy can be transported away by neutrino and radiative cooling. But as the temperature further rises, the carbon reaction rate is enhanced and a convective motion is born in the core. This convective core has to grow very fast due to the high sensitivity of the carbon burning rate, which leads to a high increase in energy generation. This phase is called the C-flash phase (Lesaffre et al., 2006). As soon as the convective time scale exceeds the nuclear burning time scale, the nuclear energy

cannot be transported away from the core any longer and a thermonuclear runaway may occur. This constitutes the onset of the explosion, where explosion models of Type Ia supernovae begin.

Another process which is important in this phase immediately preceding the ignition is the convective Urca process. The Urca process was first proposed by Gamow & Schoenberg (1941) as a source for cooling in stars. It incorporates a pair of nuclei connected by beta decay and electron capture reactions, both emitting neutrinos/antineutrinos respectively. Paczyński (1972) connected the Urca process with the convective motion in the interior of the WD core after the onset of carbon burning. As the treatment of convection together with chemical reactions is very complex and numerically demanding, different numerical studies have yielded different results over the years. The results from Lesaffre et al. (2005) and Stein & Wheeler (2006) show that the convective Urca process influences the convective motion and should be taken into account for more realistic models.

The initial models used in this work are based on Lesaffre et al. (2006). They follow the evolution of the WD from the end of a common envelope phase to the ignition of a thermonuclear flame. They also capture the accretion, the convective motion of the core and the C flash. Unfortunately, numerical obstacles prevent the implementation of the Urca process. The results concerning the WD structure just before ignition are as follows: The convective core is carbon depleted with a central carbon mass fraction of about 0.27 to 0.40 (Lesaffre et al., 2006, Fig. 8). The mass of the convective core depends on the central density and the ignition criterion and ranges from $0.84 M_{\odot}$ to $1.25 M_{\odot}$ (Lesaffre et al., 2006, Fig. 7). Due to the convection in the core, the composition is homogeneous in the core. In the outer layer of accreted material the carbon mass fraction is 0.5, because this is expected from steady He burning under these conditions.

2.5 Thermodynamical Properties of WD Matter

White dwarfs are the final stage of stellar evolution for low-mass stars and because nuclear burning has ceased, only the degeneracy pressure of the electrons stabilizes the white dwarf against gravitational collapse. This leads to a high compression and central densities in the WD of about 10^9 g/cm^3 . The temperature in the beginning depend on the evolution of the object but are below $\sim 10^9 \text{ K}$. During the explosion, nuclear burning can increase the temperature up to 10^{10} K . In order to compute thermodynamical properties at these extreme conditions, the equation of state has to take into account several contributions and is dominated by the electron gas, which is arbitrarily degenerate and relativistic. Other contributions can be attributed to the photon gas, the nuclei and electron-positron pair creation. These contributions have to be valid over a wide range of temperatures and densities.

The thermodynamic quantities are determined by specifying the temperature T , the density ρ , the mean number of nucleons per isotope $\bar{A} = (\sum Y_i)^{-1}$ and the mean charge per isotope $\bar{Z} = \bar{A} \sum Z_i Y_i$. If instead of temperature, the energy is given—as in most hydrodynamical simulations—the temperature can be computed iteratively.

Following Timmes & Arnett (1999), the total specific pressure and energy can be

expressed as a sum over the individual contributions,

$$\begin{aligned} p_{\text{eos}} &= p_{\text{el}} + p_{\text{pos}} + p_{\text{nuc}} + p_{\text{rad}}, \\ e_{\text{eos}} &= e_{\text{el}} + e_{\text{pos}} + e_{\text{nuc}} + e_{\text{rad}}, \end{aligned} \quad (2.36)$$

where the subscripts denote the contributions from electrons, positrons, nuclei and radiation, in this order.

The contributions from *electrons* and *positrons* as a noninteracting Fermi gas use the relativistic Fermi-Dirac integrals $F_k(\eta, \beta)$, defined as

$$F_k(\eta, \beta) = \int_0^\infty \frac{x^k \sqrt{1 + \frac{1}{2}\beta x}}{\exp(x - \eta) + 1} dx, \quad (2.37)$$

where $\beta = kT/(m_e c^2)$ is the relativity parameter and $\eta = \mu/kT$ the normalized chemical potential (k : Boltzmann constant, m_e : electron rest mass, c : vacuum speed of light). The contributions to pressure and energy due to free electrons and positrons are (Timmes & Arnett, 1999)

$$\begin{aligned} p_{\text{el}} &= \frac{16\pi\sqrt{2}}{3h^3} m_e^4 c^5 \beta^{5/2} \left[F_{3/2}(\eta, \beta) + \frac{1}{2}\beta F_{5/2}(\eta, \beta) \right], \\ e_{\text{el}} &= \frac{8\pi\sqrt{2}}{\rho h^3} m_e^4 c^5 \beta^{5/2} [F_{3/2}(\eta, \beta) + \beta F_{5/2}(\eta, \beta)], \\ p_{\text{pos}} &= \frac{16\pi\sqrt{2}}{3h^3} m_e^4 c^5 \beta^{5/2} \left[F_{3/2}\left(-\eta - \frac{2}{\beta}, \beta\right) + \frac{1}{2}\beta F_{5/2}\left(-\eta - \frac{2}{\beta}, \beta\right) \right], \\ e_{\text{pos}} &= \frac{8\pi\sqrt{2}}{\rho h^3} m_e^4 c^5 \beta^{5/2} \left[F_{3/2}\left(-\eta - \frac{2}{\beta}, \beta\right) + \beta F_{5/2}\left(-\eta - \frac{2}{\beta}, \beta\right) \right] + \frac{2m_e c^2 n_{\text{pos}}}{\rho}, \end{aligned} \quad (2.38)$$

where the number density of free positrons n_{pos} is given by

$$n_{\text{pos}} = \frac{8\pi\sqrt{2}}{h^3} m_e^3 c^3 \beta^{3/2} \left[F_{3/2}\left(-\eta - \frac{2}{\beta}, \beta\right) + \beta F_{5/2}\left(-\eta - \frac{2}{\beta}, \beta\right) \right]. \quad (2.39)$$

Due to the high densities, the *nuclei* and the electron gas can be assumed to be in thermal equilibrium, allowing to describe the completely ionized nuclei as a Maxwell-Boltzmann gas. The contribution to specific energy and pressure can be expressed as

$$e_{\text{nuc}} = \frac{3}{2} k T N_A \frac{1}{A}, \quad p_{\text{nuc}} = k T N_A \rho \frac{1}{A}, \quad (2.40)$$

where N_A denotes Avogadro's constant.

The *photons* are assumed to follow a black-body spectrum in local thermodynamic equilibrium, thus yielding the contributions according to the Stefan-Boltzmann law,

$$e_{\text{rad}} = \frac{4\sigma}{\rho c} T^4, \quad p_{\text{rad}} = \frac{4\sigma}{3c} T^4, \quad (2.41)$$

where σ is the Stefan-Boltzmann constant.

As the computation of these formulae is numerically too expensive, in simulations pre-tabulated values are used combined with an interpolation scheme. Details on the numerical implementation are given in Section 3.1.3.

3 Numerical Methods

3.1 Hydrodynamical Simulations

The key challenge in simulating thermonuclear supernova explosions is—similarly to other astrophysical phenomena—the multi-scale character of the problem. Firstly, the size of the WD progenitor is of the order of 10^8 cm, whereas the flame size of the deflagration for example is of the order of 10^{-4} cm (cf. Timmes & Woosley, 1992). As the microscopic processes of viscosity, heat conduction and chemical diffusion are very important for the propagation of deflagrations, but cannot be resolved, an approximate treatment for the flame has to be applied. In our simulations, we use the *level set method* (see Section 3.1.2)—treating the flame as a discontinuity given by the zero level set of a signed distance function.

Secondly, a large discrepancy exists between the time scales of nuclear burning and hydrodynamical evolution. In order to avoid resolving the shortest timescales, a simplified set of nuclear reactions is introduced as occurring instantaneously at the flame discontinuity. This is combined with a postprocessing step yielding the detailed nucleosynthetic abundances.

As pointed out by Müller (1998), one tries to solve the Euler equations instead of the Navier-Stokes equations, neglecting viscosity. However, some kind of numerical viscosity is introduced intrinsically through discretization of the Euler equations and this viscosity behaves differently from the one present in the Navier-Stokes equations.

3.1.1 Discretization of the Euler Equations

A very good introduction to the discretization of the Euler equations and to hyperbolic systems of conservation laws in general is given by LeVeque (1998).

In order to solve a differential equation numerically, a discretization of the domain of the differential equation is necessary. In the case of our partial differential equations, a computational grid is introduced in the spatial and temporal variables. For the sake of simplicity, we consider here an equidistant spacing $h = \Delta x = \Delta y = \Delta z$ in space and $k = \Delta t$ in time. Then the value of a vector of m physical quantities $q(x, y, z, t) \in \mathbb{R}^m$ is denoted by

$$q_{ijk}^n = q(x_i, y_j, z_k, t_n), \quad (3.1)$$

where the upper index denotes the temporal coordinate and the lower indices denote the spatial coordinates.

A more natural method of solving balance equations, which in the absence of sources are conservation laws, are *finite volume* methods. In these methods, the value q_i^n is

interpreted as an average of the function $q(x, t)$ over the finite interval $\mathcal{C}_i = [x_{i-1/2}, x_{i+1/2}]$ and not as an approximation to the function value itself:

$$q_i^n = \frac{1}{h} \int_{\mathcal{C}_i} q(x, t_n) dx \quad (3.2)$$

This can now be applied to the integral form of the balance equation (2.4) (without source term, for simplicity), taken over one interval and integrated over one time step,

$$\int_{\mathcal{C}_i} (q(x, t_{n+1}) - q(x, t_n)) dx = - \int_{t_n}^{t_{n+1}} [j(q(x_{i+1}, t)) - j(q(x_i, t))] dt. \quad (3.3)$$

Plugging in Equation (3.2), this can be cast in the flux-differencing form

$$q_i^{n+1} = q_i^n - \frac{k}{h} (J_{i+1}^n - J_i^n), \quad (3.4)$$

where J_i^n is an approximation to the flux integral

$$J_i^n \approx \frac{1}{k} \int_{t_n}^{t_{n+1}} j(q(x_i, t)) dt. \quad (3.5)$$

Equation (3.4) is now better suited to the problem of solving conservation laws. The change of q in a cell is only mediated by the flux to the neighbouring cells, which ensures exact conservation of the quantity on the numerical grid.

A popular method for solving Equation (3.4) in the case of the Euler equations is *Godunov's method*. The idea is that the values q^n at some time t_n are interpreted as values of a piecewise constant function $\tilde{q}^n(x, t_n)$. Now the flux function is defined using this piecewise constant function,

$$J_i^n = \frac{1}{k} \int_{t_n}^{t_{n+1}} j(\tilde{q}^n(x_i, t)) dt. \quad (3.6)$$

The solution to (3.6) consists now of solving the Riemann problem (for details on the Riemann problem, see e.g. LeVeque, 1998) at the interfaces of all grid cells separately, if the time step k is small enough: the fact that the solution to the Riemann problem is a similarity solution, i.e. it is constant along rays x/t , means that the value of \tilde{q}^n along the cell interface is constant—as long as no interference from neighbouring interfaces occurs. This results in the *CFL criterium* (named after Courant, Friedrichs, Lewy, see Courant et al., 1928) for the time step size

$$\Delta t \leq \frac{\Delta x}{s_{\max}}, \quad (3.7)$$

where s_{\max} is the maximum wave speed from the Riemann problem.

In order to compute the fluxes, an appropriate Riemann solver has to be employed. Moreover, there are also more elaborate schemes with a higher spatial order, using e.g. parabolae for the interpolation of the function q . The details of the numerical scheme and Riemann solver used in our supernova code LEAFS are given in Section 3.1.3.

3.1.2 Level Set Method

The *level set method* was introduced by Osher & Sethian (1988) in order to track hydrodynamical discontinuities. The basic idea of the level set method is that the front geometry is given by the set where a certain scalar function has the value 0. If the scalar function has an n -dimensional argument, this yields the front geometry as a $(n - 1)$ -dimensional hypersurface. The method was extended to flame fronts (e.g. deflagrations and detonations) by Smiljanovski et al. (1997). This extension allows the front to propagate in its normal direction in addition to the hydrodynamical advection.

The presentation here follows Reinecke et al. (1999b). Given the level set function $G : \mathbb{R}^n \rightarrow \mathbb{R}$ in n dimensions, the front geometry is expressed as the $(n - 1)$ -dimensional hypersurface Γ ,

$$\Gamma = \{\mathbf{r} \mid G(\mathbf{r}) = 0\}. \quad (3.8)$$

Equation (3.8) does not completely fix the function G ; additional constraints can be imposed. We request G to be a distance function, i.e. $|\nabla G(\mathbf{r})| = 1$. This implies that the level set function G is a smooth function, which has numerical advantages. This can be reached by requesting Now an equation has to be found governing the evolution of the level set function G in time. This equation must combine the hydrodynamical evolution and the additional propagation in the normal direction. Thus the total propagation velocity of a point P attached to the front is best split according to

$$\dot{\mathbf{x}}_P = \mathbf{v}_u + s_u \mathbf{n}, \quad (3.9)$$

where \mathbf{v}_u is the velocity of the unburnt material, s_u the propagation velocity of the front and $\mathbf{n} = \nabla G / |\nabla G|$ the normal vector to the front. At a point P attached to the front, the level set function does not change with respect to P :

$$\left(\frac{dG(\mathbf{r}, t)}{dt} \right)_P = \partial_t G(\mathbf{x}_P, t) + \dot{\mathbf{x}}_P \cdot \nabla G = 0 \quad (3.10)$$

This yields, combined with Equation (3.9) the equation for the temporal evolution of the level set function G ,

$$\partial_t G = -(\mathbf{v}_u + s_u \mathbf{n}) \cdot \nabla G. \quad (3.11)$$

Equation (3.11) is now solved in a split operator approach: the first part is due to advection with the fluid motion. Hence, the level set function G can be advected as a passive scalar in the PROMETHEUS implementation, similar to a chemical species. The second part is calculated separately using an upwind formula for the gradient and a pre-defined table or formula for the propagation speed s_u (for details, see Reinecke et al., 1999b).

As Equation (3.11) is strictly valid only at the front itself, it can only be applied in the vicinity of the front. Farther away from the front, a different numerical method has to be applied in order to ensure the distance function property of G . In each time step, a re-initialization of the level set function is applied in a pseudo-time approach (Sussman et al., 1994),

$$\frac{\partial G}{\partial \tau} = \frac{G}{|G| + \epsilon} (1 - |\nabla G|), \quad (3.12)$$

which essentially restores the distance function property of G (ϵ is an empirical parameter with a value in the order of the grid cell length). To avoid an artificial movement of the front, cells located in a belt of about three cells around the front are left nearly unchanged using a non-linear weighting function (for details, see Reinecke et al., 1999b).

The way nuclear reactions are treated is of central importance for this work, because we study how different initial compositions affect nuclear burning. In the level set approach, the nuclear burning is both supposed to happen instantaneously at the burning front, which is a discontinuity given by the zero level set of G . This approximation is very good especially for deflagrations, as deflagration flames are very thin under the conditions given here (on the order of 10^{-4} cm for a density of 1×10^9 g/cm³, cf. Timmes & Woosley, 1992). For detonations, the approximation is still good at high densities, where the flame width is small. But at lower densities, the flame width grows larger; for Si burning e.g. larger than the size of the WD (Gamezo et al., 1999). Consequently, on one hand, incomplete burning to intermediate mass elements or even only oxygen results. On the other hand, the internal wave structure of the detonation front should be taken into account, which is very complex and shows a cellular pattern in more than one dimension (Gamezo et al., 1999). This cellular pattern can affect the nucleosynthetic outcome and lead to an inhomogeneous distribution of the burnt material. But since the burning front is approximated by a discontinuity, these effects have to be neglected. Instead, the final outcome of the burning is taken from tables relating it to the density of the unburnt material. The burning tables with the abundances have to be created before the actual simulations. The burning front propagation velocity is also taken from a pre-created table for detonations and from a fit formula from Timmes & Woosley (1992) for deflagrations.

In each cell cut by the front, the volume fraction α of the unburnt fuel has to be determined in order to know how much fuel should be burned. In two dimensions, the level set function G , which is given in the center of the cell, is interpolated to the corners. Then the roots of this function are obtained by linear interpolation. Here, a topological ambiguity may occur, which is solved by taking the average of the two possible configurations (compare Reinecke et al., 1999b, Fig. 2). The fraction α is finally given as the area of the cell where $G < 0$.

As the number of topological ambiguities increases in three dimensions, a different method is chosen here (Reinecke, 2001). First, an average length \bar{r} in the cell with indices (i, j, k) is defined,

$$\bar{r} = (\Delta x_i \Delta y_j \Delta z_k)^{1/3}. \quad (3.13)$$

Now the volume fraction α_{ijk} of unburnt material is computed by comparing with the value of G_{ijk} , using the distance function property,

$$\alpha_{ijk} = \begin{cases} 1 & , G_{ijk} < -\bar{r} \\ 0 & , G_{ijk} > \bar{r} \\ \frac{1}{2} \left(1 - \frac{G_{ijk}}{\bar{r}}\right) & \text{otherwise.} \end{cases} \quad (3.14)$$

This value of α determines now the conversion of fuel to ashes and thus, the energy release. The new fractions of fuel X'_{fuel} and ashes X'_{ashes} are updated from the old

fractions X_{fuel} and X_{ashes} according to (Reinecke et al., 1999b)

$$\begin{aligned} X'_{\text{ashes}} &= \max(1 - \alpha, X_{\text{ashes}}), \\ X'_{\text{fuel}} &= 1 - X'_{\text{ashes}}. \end{aligned} \quad (3.15)$$

The use of the maximum operator in Equation (3.15) prevents “reverse burning” from fuel to ashes. This could otherwise occur due to discretization errors (Reinecke et al., 1999b). The resulting change in the total energy e_{tot} caused by the difference in binding energies of fuel and ashes is given by

$$e'_{\text{tot}} = e_{\text{tot}} + q(X'_{\text{ashes}} - X_{\text{ashes}}) \quad (3.16)$$

where q is the reaction q value, given by the difference in binding energies of the composition.

3.1.3 LEAFS

The code used for computing the hydrodynamical simulations of SNe Ia in this work is the LEAFS code (LEvelset based Astrophysical Flame Simulations), developed at the Max Planck Institute for Astrophysics in Garching. This program has undergone a major re-implementation by M. Reinecke which is described very well in his doctoral thesis (Reinecke, 2001), as well as in Reinecke et al. (1999a) and Reinecke et al. (2002a).

The code uses the Eulerian version of the *piecewise parabolic method* (PPM), developed by Colella & Woodward (1984), in the PROMETHEUS implementation by Fryxell et al. (1989). PPM is a finite volume scheme similar to Godunov’s method (see standard textbooks, e.g. LeVeque (1998) and Section 3.1.1), but uses parabolae for the reconstruction. This allows for a better representation of smooth gradients on the one hand and discontinuities on the other hand. Discontinuities, e.g. hydrodynamical shocks, are typically smeared out over three cells, rendering them quite sharp compared to other numerical schemes. In order to solve the multidimensional problem, dimensional splitting is applied, where the hydrodynamical equations are solved consequently for each direction. In order to preserve the symmetry of the scheme, the hydrodynamical sweeps are done twice in each time step, once in reverse order.

The Riemann problem is solved according to the method presented in Colella & Glaz (1985). Our approximate Riemann solver is capable of using a general convex equation of state—a crucial prerequisite for using it in the context of WD matter.

In order for the numerical scheme to be stable, the size of the time step has to fulfill the CFL criterion (3.7). As the speeds occurring in the solution of the Riemann problem are not easily available in the code, the criterion for determining the time step Δt uses the local velocity in the cell \mathbf{u} and the sound speed c_s :

$$\Delta t = C_{\text{CFL}} \left(\frac{|v_x|}{\Delta x} + \frac{|v_y|}{\Delta y} + \frac{|v_z|}{\Delta z} + c_s \sqrt{\frac{1}{(\Delta x)^2} + \frac{1}{(\Delta y)^2} + \frac{1}{(\Delta z)^2}} \right)^{-1}. \quad (3.17)$$

For two dimensions, the terms containing z are simply omitted. In order to ensure the stability of the system, the additional factor C_{CFL} is set to 0.8.

The equation of state used in the code is based on the Timmes equation of state (Timmes & Swesty, 2000) and includes contributions from an arbitrarily degenerate and relativistic electron-positron gas, a photon gas and an ideal Maxwell-Boltzmann gas of ions (compare Section 2.5). In order to speed up the computations—as the equation of state is the most expensive operation in the code in total—a simple bilinear interpolation is used instead of the biquintic interpolation proposed in Timmes & Swesty (2000).

Because of the large difference in scales, the deflagration and detonation burning fronts are treated as discontinuities with the *level set* approach (see Section 3.1.2). It is used as described by Reinecke et al. (1999b). Since the “complete implementation” mentioned in there has serious numerical difficulties, the “passive implementation” is used. The technical difficulties of the “complete implementation” occurring in SN Ia simulations are in part due to the degenerate equation of state and in part due to the errors in finding the volume fraction α of unburnt volume in a cell. This problem is even more serious in three dimensions, as several topological ambiguities complicate the computation of α .

In order to track the nucleosynthesis, in principle a nuclear network (compare Section 2.2.1) has to be included. But as this is computationally very expensive, a simple approach is chosen, as introduced by Reinecke et al. (2002a). The chemical composition is simplified and includes five species, namely α particles, ^{12}C , ^{16}O , “Mg”, representing intermediate mass elements (IME), and “Ni”, representing iron group elements (IGE). Directly behind the burning front, the composition of the volume fraction $1 - \alpha$, which is converted from fuel to ashes, is given by a table depending on the density of the unburnt material and on the initial composition of the cell. The table consists of entries equidistant in the logarithm of the density and the carbon mass fraction. Bilinear interpolation in these quantities is used to compute the final composition, which consists of C, O, IME and IGE. The fraction of α particles is determined in an additional step according to a table in order to account for the shift in binding energies in NSE (see Section 3.2.3).

The density which is used for looking up the abundances and propagation speeds is not unambiguously defined due to numerical reasons. As the burning fronts are smeared out over about three cells (a consequence of the PPM scheme), several methods can be used to estimate the burning density of the fuel. For deflagrations, the burning density is taken to be the local density, except if some neighbouring cell with a high fuel content exists with a higher density. This is a reasonable approximation as the density drop at the front is not too high and since this method seems to reduce the scatter occurring in the calibration of the abundance tables (Section 4.1.2; I. Seitenzahl, private communication). For detonations, this approximation is not reasonable, as a spike in the density is present at the location of the level set. One possibility is to look into cells in front of the smeared-out shock. A caveat of this method, however, is that the burning density is underestimated especially in the outer cells with a steep density gradient. Therefore, the burning density is frozen approximately four cells in front of the zero level set of the level set function and then advected as a passive scalar. This ensures that the effects of compression are avoided. The advection of the frozen burning density with the fluid flow is necessary especially in conjunction with the moving grid (see below), in order to have the right burning density passed to the detonation wave front.

The computational grid used in the discretization of the Euler equations was static in the simulations of Reinecke et al. (1999a, 2002a). It consisted of 256×256 grid cells and contained an equidistant inner part of 226×226 cells and exponentially growing cells in the outer part. As the WD expands rather fast because of the thermonuclear burning, this static grid allows tracking the expanding ejecta only up to 1.5 s. Another problem with this approach is that the flame is resolved only very coarsely at later times. This was improved by the “*co-expanding uniform grid approach*”, introduced in Röpke (2005) and applied to a set of 3D Chandrasekhar mass deflagration models in Röpke & Hillebrandt (2005). The technique is based on the work of Winkler et al. (1984) and Müller (1994) and introduces a grid moving with a velocity \mathbf{u}_{grid} following Röpke (2005). This point of view is more general than Lagrangian or Eulerian coordinates, which can be obtained by setting $\mathbf{u}_{\text{grid}} = \mathbf{u}$ and $\mathbf{u}_{\text{grid}} = 0$, respectively. If now $\frac{d}{dt}$ denotes the time derivative in the grid frame, the relation to the Eulerian derivative ∂_t is similar to the Lagrangian case,

$$\frac{d}{dt}q = \partial_t q + \mathbf{u}_{\text{grid}} \cdot \nabla q. \quad (3.18)$$

Using the moving grid transport theorem for a grid cell with volume V_{grid} (Röpke, 2005),

$$\frac{d}{dt} \iiint_{V_{\text{grid}}} q dV_{\text{grid}} = \iiint_{V_{\text{grid}}} (\partial_t q + \nabla \cdot (q \mathbf{u}_{\text{grid}})) dV_{\text{grid}}, \quad (3.19)$$

an integral form of the balance equation (2.5) is obtained,

$$\frac{d}{dt} \iiint_{V_{\text{grid}}} q dV_{\text{grid}} = - \oiint_{\partial V_{\text{grid}}} q \mathbf{u}_{\text{rel}} \cdot d\mathbf{S}_{\text{grid}} + \iiint_{V_{\text{grid}}} s_q dV_{\text{grid}}, \quad (3.20)$$

where $\mathbf{u}_{\text{rel}} = \mathbf{u} - \mathbf{u}_{\text{grid}}$ is the relative velocity. This is very similar to the usual balance equation in integral form (2.4) with the flux $j_q = q\mathbf{u}$ being replaced by $q\mathbf{u}_{\text{rel}}$. Equation (3.20) can now be discretized in the same way as the usual equation (2.4).

Using the expanding grid, Röpke (2005) was able to follow the expansion for 10 s and verified that the deviation from homologous expansion is rather small, below 10% for most parts of the star (cf. Röpke, 2005, Fig. 10). A further improvement to the approach was introduced in Röpke et al. (2006b), the use of a *moving hybrid grid*. This grid consists of two sub-grids and combines an equidistant inner grid and an exponentially spaced outer grid with the moving grid technique. In the beginning of the simulations, both grids move separately: the inner grid tracks the outer border of the deflagration flame and the outer grid tracks the expansion of the WD. As the flame grows in size, cells from the outer grid are merged into the inner grid when the sizes match. Finally, the grid is nearly uniform everywhere and tracks the expansion of the WD. This can also be seen in Figure 3.1: the left plot shows the grid in the beginning, which is equidistant in the inner part and exponentially spaced in the outer part. The right plot shows the grid in the end, where a nearly equidistant state is reached. This method allows for a high resolution in the inner part, thus resolving the flame much better than in the uniform moving grid approach. Moreover, the implementation of the new subgrid scale model (see below) is based on an equidistant grid. At the same time, the expansion of the WD can be followed for much longer time scales up to 100 s.

As the burnt matter behind the deflagration front has a lower density than the unburnt fuel, it is subject to the Rayleigh-Taylor instability and consequently also to the Kelvin-Helmholtz instability (compare Section 2.1.3). If one now compares a corresponding length scale l and velocity scale u to the viscosity ν , which is similar to liquids or gases on earth, the corresponding *Reynolds* number

$$\text{Re} = \frac{lu}{\nu} \quad (3.21)$$

can be as large as 5×10^{13} (Woosley et al., 2009). This means that the flow is highly turbulent.

As the numerical method given here can only resolve large scales, a model for the propagation of the front and the dissipation of energy on unresolved scales, a *subgrid scale model* (SGS model), has to be employed (Niemeyer & Hillebrandt, 1995; Schmidt et al., 2006a,b). The entire simulations are conducted in the spirit of large eddy simulations (LES). But instead of implementing the turbulent viscosity in the hydrodynamical scheme, the intrinsic numerical viscosity of the PPM scheme is used and the effect of turbulence is modeled through a turbulent energy.

The turbulent combustion regime which applies to most of the explosive burning is the so called *flamelet regime* (e.g. Röpke & Schmidt, 2009). In this regime, the flame surface is wrinkled by the turbulent structure of the flow. But as the Gibson length—the length scale of the smallest eddies—is larger than the flame width, the microscopic structure of the front is not altered by the turbulent flow. Thus, the propagation of the front is governed by the turbulent motion (Damköhler, 1940).

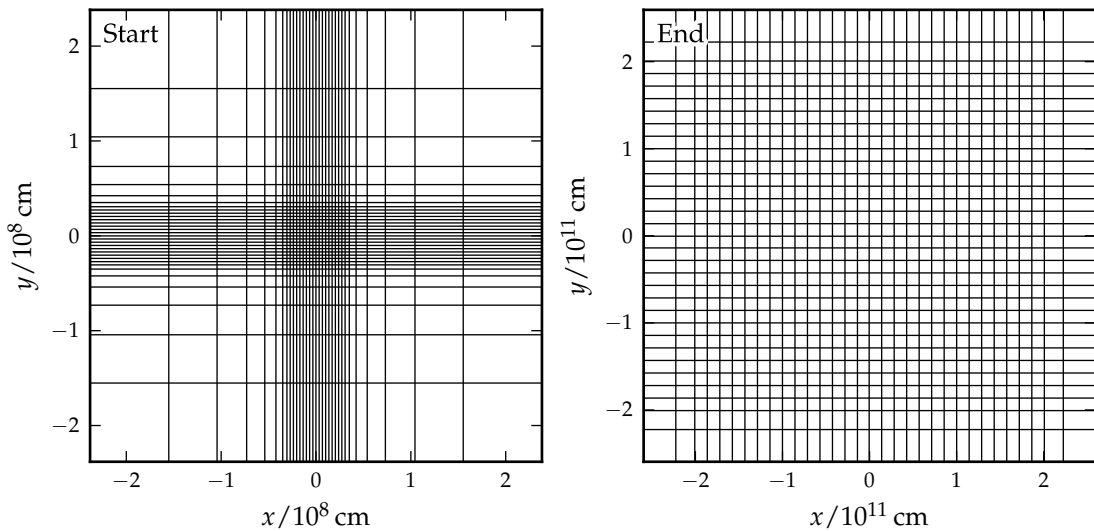


Figure 3.1 | Moving hybrid grid. In this figure, the computational grid at the beginning of a simulation (left) and at the end of a simulation (right) is compared. Shown here is the x - y plane of a full star 3D simulation with 512^3 grid cells. For better visualization, only every 16th grid border is shown. Since the grid is symmetrical in every direction, the grid cell borders in z direction are the same as in x and y .

A first SGS model was introduced by Niemeyer & Hillebrandt (1995). As the numerical scheme introduces an artificial dissipation at the length scale Δ , the grid spacing, the processes below this length scale remain unresolved. This SGS model tries to model the energy dissipation through turbulent motion on length scales below Δ down to the Gibson scale (see also Section 2.3.4). As the flame surface is enlarged to a fractal surface of fractal dimension $D \approx 2.3$, the burning rate and propagation velocity are enhanced dramatically compared to laminar burning. The propagation velocity s of the front in the model of Niemeyer & Hillebrandt (1995) is given by

$$s = \max(s_1, q_{\text{sgs}}), \quad (3.22)$$

where s_1 is the laminar burning speed (see Equation (2.34) and Timmes & Woosley, 1992) and q_{sgs} the size of SGS velocity fluctuations.

A more elaborate turbulence SGS model was proposed and implemented by Schmidt et al. (2006a,b). As this model is only implemented in three dimensions, the old SGS model by Niemeyer & Hillebrandt (1995) is still in use for the 2D simulations. The new model uses a filtering approach devised by Germano (1992), where the high frequency parts of the Fourier representation of all quantities are filtered out in order to represent the numerical quantities. The reason is that this part of the spectrum above the critical wave number $k_c = \pi/\Delta$ (Δ : grid resolution) is not present in the numerical representation of the quantity. This filtering leads to a set of equations needing closure relations that are determined locally. The flame propagation speed s is given in this model as

$$s = \left(s_1^2 + C_t q_{\text{sgs}}^2 \right)^{1/2}, \quad (3.23)$$

with s_1 being the same as in Equation (3.22) and q_{sgs} being the size of the velocity fluctuations in the new SGS model. The turbulent burning coefficient $C_t = 4/3$ is set according to Schmidt et al. (2006b). Equation (3.23) allows for a smooth transition between the laminar burning regime and the turbulence dominated flamelet regime: For small turbulent velocity fluctuations the flame propagates with the laminar burning speed $s \approx s_1$. For large SGS velocity fluctuations, the propagation speed is $s \approx 2q_{\text{sgs}}/\sqrt{3}$ and dominated by the turbulent energy.

In order to trigger a DDT, which is essential for delayed detonation models, the criterion described in Ciaraldi-Schoolmann et al. (2012) (see also Seitzzahl et al., 2012) is employed in our three-dimensional simulations. The flame surface for cells with a certain fuel and density range is estimated by assuming a fractal surface with fractal dimension $D = 2.36$. Using this flame surface, an effective detonation flame surface is calculated by multiplying the flame surface by the probability of high velocity fluctuations $\gtrsim 10^8$ cm/s to occur. If this effective surface exceeds a critical value calculated using a critical length for the detonation initiation (Seitzzahl et al., 2009) for a time longer than half an eddy turnover time, detonations are initiated. The number of initiated detonations is given by the ratio of the two flame surfaces. The detonations are initiated in the cells with the highest velocity fluctuations.

3.2 Nuclear Reactions

3.2.1 Nuclear Reaction Network

In order to solve a nuclear reaction network, Equations (2.12), a system of non-linear ordinary differential equations (ODEs), have to be solved. These equations turn out to be *stiff*. It is still somewhat unclear how to mathematically define stiffness, but a good overview of the problem is given in Higham & Trefethen (1993). In a nuclear reaction network, the stiffness is caused by the large discrepancies in the timescales of the different reaction rates.

When integrating a set of ODEs with an explicit method, the size of the time step is usually determined by requesting a certain accuracy to be reached. If now the constraint on the time step does not emerge from accuracy, but from stability of the numerical solution, the system of ODEs is said to be stiff—at least in a heuristic sense. In order to lift this constraint on the time step, implicit methods can be used. Implicit methods evaluate the right hand side of the set of ODEs at the new time value—as opposed to explicit methods—hence resulting in an implicit equation for the function value at the new time value (see also the discussion in Müller, 1998). Examples for implicit algorithms suited for integrating stiff ODEs are the backward Euler method or the algorithm described by Bader & Deuffhard (1983), which employs a semi-implicit midpoint rule.

3.2.2 Postprocessing

It is computationally too costly to calculate the detailed nucleosynthetic abundances coupled to hydrodynamics. Thus, hydrodynamical simulations are carried out with a simplified composition ensuring the energy conversion by the reactions is taken into account. This can be implemented either by coupling a small network to the hydrodynamics capturing the key reactions (as suggested in Müller, 1998) or by using the level set method, where the chemical reactions happen instantaneously at the burning front (see Section 3.1).

After the hydrodynamical simulation is finished, the detailed nucleosynthesis is computed in an additional postprocessing step. This was already done by Thielemann et al. (1986), who investigated detailed nucleosynthesis for Lagrangian mass shells in one dimensional deflagration models of SNe Ia. In more than one dimension, Nagataki et al. (1997) first used the concept of *tracer particles* in the field of Type II supernovae. As the main energy source for core collapse supernovae is gravitational binding energy, they neglected the impact of the nucleosynthesis on hydrodynamics and calculated the nucleosynthesis afterwards. To this end, “test particles” were included in the simulation following the hydrodynamical flow and recording density and temperature. These particles represent a certain mass of the star, when calculating the nucleosynthesis results in the postprocessing, but are just passively advected, having no impact on gravity or hydrodynamics. In the Lagrangian frame of these tracer particles, the only change in the specific abundances is caused by reactions. Thus, solving Equation (2.12) on the thermodynamic trajectory of a tracer particle yields the nucleosynthetic abun-

dances, i.e. the final abundances of that particle. Information about the nucleosynthesis of the entire explosion is recovered by summing over a sufficient number of tracer particles.

The tracer particle method used in our simulations is based on the work of Travaglio et al. (2004). A certain number of “marker particles” (this term was used in Travaglio et al., 2004) is distributed equidistantly in the mass coordinate $M(r)$, in the azimuthal angle ϕ and in $\cos(\theta)$ and passively advected during the hydrodynamical simulation. As in the hydrodynamical simulation the temperature is derived from the internal energy, which is directly computed, the temperature is re-computed from the energy also in the postprocessing step. The nuclear reaction network was implemented by F.-K. Thielemann and is described in more detail in Thielemann et al. (1996) and Iwamoto et al. (1999). The method used in this nuclear network for solving equations (2.12) is a backward Euler algorithm. Newer developments are the inclusion of new weak rates from Martínez-Pinedo et al. (2000) and Langanke & Martínez-Pinedo (2003), as described in Brachwitz et al. (2000) and Thielemann et al. (2003). The postprocessing algorithm is explained in Röpke et al. (2006a) and applies to the current simulations with the difference that the minimum temperature for actually using the network was lowered from 2×10^9 K to 4×10^8 K. The distribution of the tracer particles follows the new scheme of variable tracer masses introduced in Seitenzahl et al. (2010). The radially varying mass of the tracer particles allows for a better resolution in the outer layers of the WD, where the density is low, but the density gradient is rather steep.

In their study of three dimensional deflagrations, Röpke et al. (2006a) treated the metallicity of the progenitor as an additional parameter in order to examine the effect on the nucleosynthetic outcome. As synthetic spectra are regularly calculated from our models now, the detailed abundance structure especially in the outer layers must be accurately computed. Therefore, the detailed chemical composition of the Sun given in Asplund et al. (2009) is taken as initial metallicity. In order to take into account the metallicity of carbon and oxygen of the Sun, their mass fractions are added to the mass fraction of ^{22}Ne . Then the sum of the mass fractions of all elements beside carbon and oxygen (about 0.018 for solar composition) is subtracted from the ^{12}C mass fraction in order to ensure particle conservation.

The distribution of tracer particles in 2D simulations is chosen in 256 radial and 160 angular zones, resulting in $\sim 40\,900$ tracer particles (depending on the exact initial model), using the algorithm of Seitenzahl et al. (2010). In 3D simulations, 100 tracer particles are used in every direction (distributed equidistantly in $M(r)$, ϕ , and $\cos(\theta)$), thus resulting in a total number of $\sim 100\,000$ tracer particles (again depending on the exact initial model).

3.2.3 Nuclear Statistical Equilibrium

In SNe Ia models including an initial deflagration phase, nuclear statistical equilibrium (NSE) holds at the high densities and temperatures in the deflagration ashes. In the LEAFS code this is modeled by adapting the proportion of IGE and α particles according to a table provided by H.-Th. Janka (Reinecke et al., 2002a).

The nuclear network used in the postprocessing step includes a NSE solver that is used at temperatures above 6×10^9 K. The nuclear reaction network YANN (Yet another nuclear network, by R. Pakmor and P. Edelmann, Pakmor et al., 2012a), is used to compute the abundances at high densities while calculating the detonation propagation speeds (Section 3.3). This nuclear network also includes a NSE solver which is employed at temperatures above 6×10^9 K. The reaction rates in YANN are taken from the latest release of the REACLIB data base (Rauscher & Thielemann, 2000) and the weak rates from Langanke & Martínez-Pinedo (2001). In order to solve the nuclear network equation, a semi-implicit midpoint rule after Bader & Deuflhard (1983) is employed. In order to compute the detailed NSE composition, equations (2.16), (2.18) and (2.19) have to be solved. This is done using a Newton-Raphson method solving for μ_p and μ_n at a given density and temperature. The detailed abundances can then be computed from these quantities.

3.3 Iterative Computation of Abundance Tables

In order to create the tables needed by the level set method, an iterative procedure described by Fink et al. (2010) is employed (Figure 3.2). This iterative calibration is carried out separately for each burning mode—deflagration and detonation. First, a hydrodynamical simulation with an initial table is carried out. This initial table is constructed in a way that at almost all densities the fuel is burned to NSE, thus overestimating the reaction Q value. The objective of the iterative scheme now is to converge to a Q value table—and an abundance table, respectively—from above.

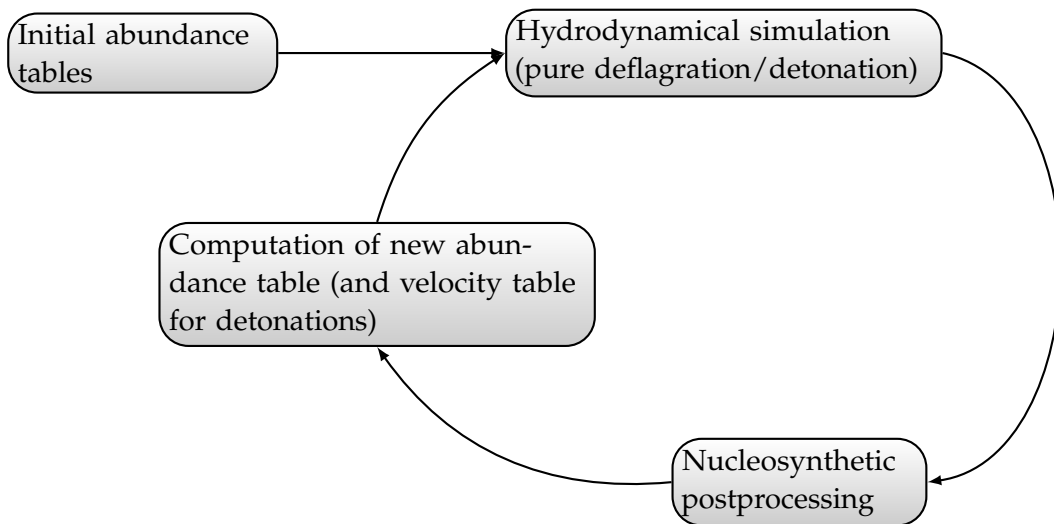


Figure 3.2 | Iterative calibration scheme. For the first run, an initial abundance table with a high reaction Q value is used. Then, hydrodynamical simulations and nucleosynthetic post-processing runs are carried out consequently. The abundance table for each hydrodynamical simulation is computed from the last nucleosynthesis results.

As described in Section 3.1.3, the level set method in our implementation needs an abundance table, where the simplified chemical composition behind the level set is given by the density of the unburnt fuel ahead of the front. Furthermore, the calibration is done in order to consistently model the nucleosynthetic yields, which should coincide with the simplified nucleosynthesis from the hydrodynamical simulations.

Now each step in this iterative procedure consists of three steps (Figure 3.2):

1. A hydrodynamical simulation is carried out using the abundance table from the previous step or the initial abundance table in the first step. This simulation includes Lagrangian tracer particles, which are advected with the flow. Until the calibration scheme is converged, the reaction Q value table for the level set method is (slightly) overestimated.
2. The detailed nucleosynthetic yields are computed using a postprocessing of the advected Lagrangian tracer particles (as explained in Section 3.2.2). This step uses only the temperature and density along the trajectories of the tracer particles.
3. In a third step, the detailed nucleosynthetic yields are used to compute a new abundance table and also a propagation velocity table in the case of detonations. For detonations, the nucleosynthetic yields are simply calculated for each tracer, giving the new table. For deflagrations, a binning is done in the density of the unburnt fuel. The detonation propagation velocities at high densities are calculated using the YANN NSE solver (Section 3.2.3).

These steps are iterated several times. The convergence of this scheme is theoretically founded on the fact that the density of the unburnt fuel shortly before the encounter with the burning front is not highly affected by the higher reaction Q value. As the rates are sensitive to this density, the postprocessing will yield a smaller and more realistic Q value. Finally, this should lead to convergence of the table.

After the sixth iteration, the changes are very small (especially for detonations, see Section 4.1), so that convergence is supposed to be achieved. The whole iterative calibration is carried out separately for each carbon mass fraction (from 0.2 to 0.9) and each burning mode (deflagration and detonation) in this work (see Section 4.1).

For the *deflagration calibration*, the initial model is chosen to be a Chandrasekhar mass WD with a homogeneous carbon mass fraction and an initial core density of $2.9 \times 10^9 \text{ g/cm}^3$. Solving for the hydrostatical equilibrium outwards gives a WD with a mass of $1.40 M_{\odot}$ and a radius of 1857 km. The hydrodynamical simulations are carried out in two-dimensional, axisymmetric geometry and use a grid with 512×1024 cells, which corresponds to a resolution of about 1 km in the inner part. The simulations use 40897 Lagrangian tracer particles which were distributed with variable masses according to Seitzzahl et al. (2010), improving the resolution in the outer parts with low densities. The tracer particles are distributed uniformly in volume in a mass shell between $1.050 M_{\odot}$ and $1.355 M_{\odot}$ and uniformly in mass anywhere else in the WD. This layer was chosen in order to better resolve the nucleosynthesis in the part with a steep density gradient.

For the *detonation calibration*, a sub-Chandrasekhar mass WD is chosen because the transition from complete burning (NSE conditions) to no burning happens at lower densities than for deflagrations. Here, the initial core density equals $1 \times 10^8 \text{ g/cm}^3$, which results in a WD with a mass of $1.17 M_{\odot}$ and a radius of 4323 km. The grid size was chosen to be 512^2 , which corresponds to a resolution in the inner part of about 9 km. Because of the supersonic nature of detonation fronts, a detonation of a WD is a one-dimensional problem if ignited centrally. Thus, a distribution of the Lagrangian tracer particles along one line is sufficient to capture the properties of the level set. For the calibration simulations, 200 tracer particles were placed along one line and distributed to be equidistant in the logarithm of the density.

The detonation propagation velocity is computed in an additional step assuming a Chapman-Jouguet detonation, where the detonation speed D is equal to the sound speed in the unburnt material. In principle, the equilibrium sound speed (as defined in (2.33)) should be taken here. But as the used equation of state does not depend strongly on the abundances of the individual species (only on \bar{A} and \bar{Z}), the equilibrium sound speed computed with respect to the changes of \bar{A} and \bar{Z} usually does not show a significant difference to the frozen sound speed. Therefore, we use the frozen sound speed for all calculations.

In order to find the detonation speed, the Rankine-Hugoniot jump conditions, equations (2.24) and (2.25), were solved using a two dimensional Newton-Raphson method in the density ρ and temperature T . In each step, energy and pressure were computed again from the equation of state. The reaction Q value (Δq in Equation (2.25)) at low densities is computed using the detailed nucleosynthesis abundances, whereas at high densities, the NSE solver from YANN is used. In the intermediate regime, both branches join smoothly. As pointed out by Khokhlov (1989), Gamezo et al. (1999) and Sharpe (1999), the structure of a one dimensional, steady detonation wave in degenerate C/O matter is of the pathological type at densities above $2 \times 10^7 \text{ g/cm}^3$ (see also Section 2.3.2). This is due to the Si-reaction becoming endothermic, thus causing a frozen sonic point in the reaction zone. This leads to higher velocities and energy releases for self-sustained pathological detonations. The propagation velocities and Q values have been calculated for material consisting of $X(^{12}\text{C}) = X(^{16}\text{O}) = 0.5$ by Gamezo et al. (1999). Because no values are available for different compositions—as needed in this work—and because the changes with respect to the Chapman-Jouguet solution are smaller than about 6% (compare Gamezo et al., 1999, Fig. 2), the pathological structure of the detonation wave-front has not been taken into account in this work. Moreover, in the delayed detonation scenario the detonation is triggered after the deflagration has already pre-expanded the WD. The density range in which the conditions for a DDT are met lies roughly between $0.5 \times 10^7 \text{ g cm}^{-3}$ and $1.5 \times 10^7 \text{ g cm}^{-3}$. Therefore, the largest part of the detonation wave propagates at densities below $2 \times 10^7 \text{ g cm}^{-3}$ and is mainly unaffected by the pathological nature at higher densities.

4 Results

4.1 Iterative Calibration

The iterative calibration is needed in order to generate the abundance and velocity tables that are essential for the level set method. The calibration is carried out as described in Section 3.3 and the results of these calibrations are presented in this section.

4.1.1 Detonations

The iterative procedure for calibrating the abundance tables has been carried out for carbon mass fractions between 0.2 and 0.9. As an example, the abundance table is plotted after each run in Figure 4.1 for $X_0(^{12}\text{C}) = 0.5$. Here the mass fractions of the elements in the simplified chemical composition used in the levelset method are plotted against the logarithmic density of the unburned material in front of the detonation front. This density is taken as the density of the corresponding tracer particle when crossing the levelset. The detailed nucleosynthesis results were matched to the simplified composition in a way that elements with similar binding energies were summed up.

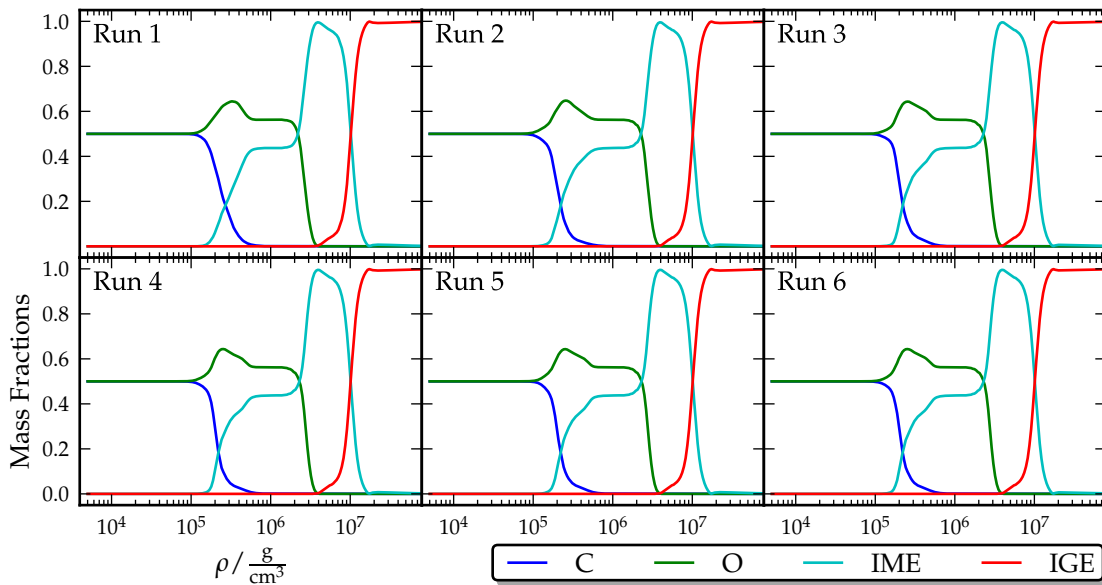


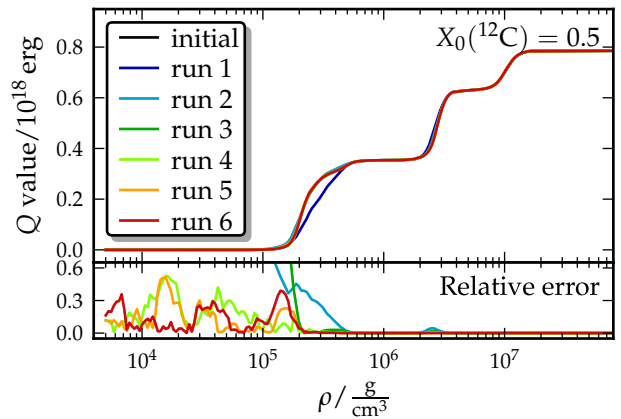
Figure 4.1 | Abundance tables for detonation calibration with $X_0(^{12}\text{C}) = 0.5$. Shown is the mass fraction of the simplified chemical composition over the logarithm of the density as calculated from the detailed nucleosynthesis postprocessing. The table named “Run 1” is used as input for the hydrodynamical run 2 and so on.

The carbon mass fraction was computed from ^{12}C , the oxygen mass fraction as the sum over ^{16}O and ^{20}Ne . The mass fractions of the IGE were computed as the sum over the elemental abundances from Ti to Mo (being the heaviest element in the network). The mass fractions of the IME were simply computed as the difference to 1 from all other mass fractions.

We start out with the initial guess of burning to IGE at almost all densities, but already after the first run, the main structure of the table emerges and changes only slightly in the subsequent runs. One can clearly distinguish the different burning stages: First, carbon burning begins at a density of about $1.2 \times 10^5 \text{ g cm}^{-3}$. At higher densities of about $2.0 \times 10^6 \text{ g cm}^{-3}$, oxygen burning starts and finally, at densities of about $7.5\text{--}8 \times 10^6 \text{ g cm}^{-3}$, silicon burning to NSE commences.

In order to examine the convergence of this iterative procedure, a comparison of the reaction Q value is more suitable. This Q value gives the nuclear energy disposed right behind the detonation front and is calculated as the difference of the nuclear energy of burned and unburned material. As the binding energy rises for higher elements up to iron group elements, the Q value rises from zero where no burning takes place to its maximum at full burning to NSE. An examination of the convergence of the abundance table for $X_0(^{12}\text{C}) = 0.5$ is given in Figure 4.2. Here, the Q values for all iteration runs are shown in the upper plot and the relative error of each table to its predecessor in the lower plot. The red curve shows the sixth iteration step which is also the final iteration. The shape of the curve after the first iteration is already very similar to that of the final iteration. The relative error decreases over the whole density range during the iterations and is close to 0 especially for densities above $\log(\rho/\frac{\text{g}}{\text{cm}^3}) = 5.4$. At lower densities, the relative error between the last iteration and its predecessor is not as small. This is probably due to the Q value being rather small rendering the convergence of this iterative procedure more difficult. Also, the initial guess of the abundance table is worst in this region. But because of the Q value being rather small, the influence of this part of the abundance table on the explosion dynamics is very limited, thus justifying the use of the table as given by the sixth iteration. The Q value of the initial table (black line) was chosen to lie well above the final Q value in order to ensure a convergence from above. This works quite well already in the first iteration step.

Figure 4.2 | Detonation Q value convergence. In the upper plot, the Q value of the detonation abundance table for $X_0(^{12}\text{C}) = 0.5$ is plotted for each iteration. In the lower plot, the relative error of the Q value compared to the previous run is shown. The relative error is computed as $|Q_{\text{old}} - Q_{\text{new}}| / Q_{\text{new}}$.



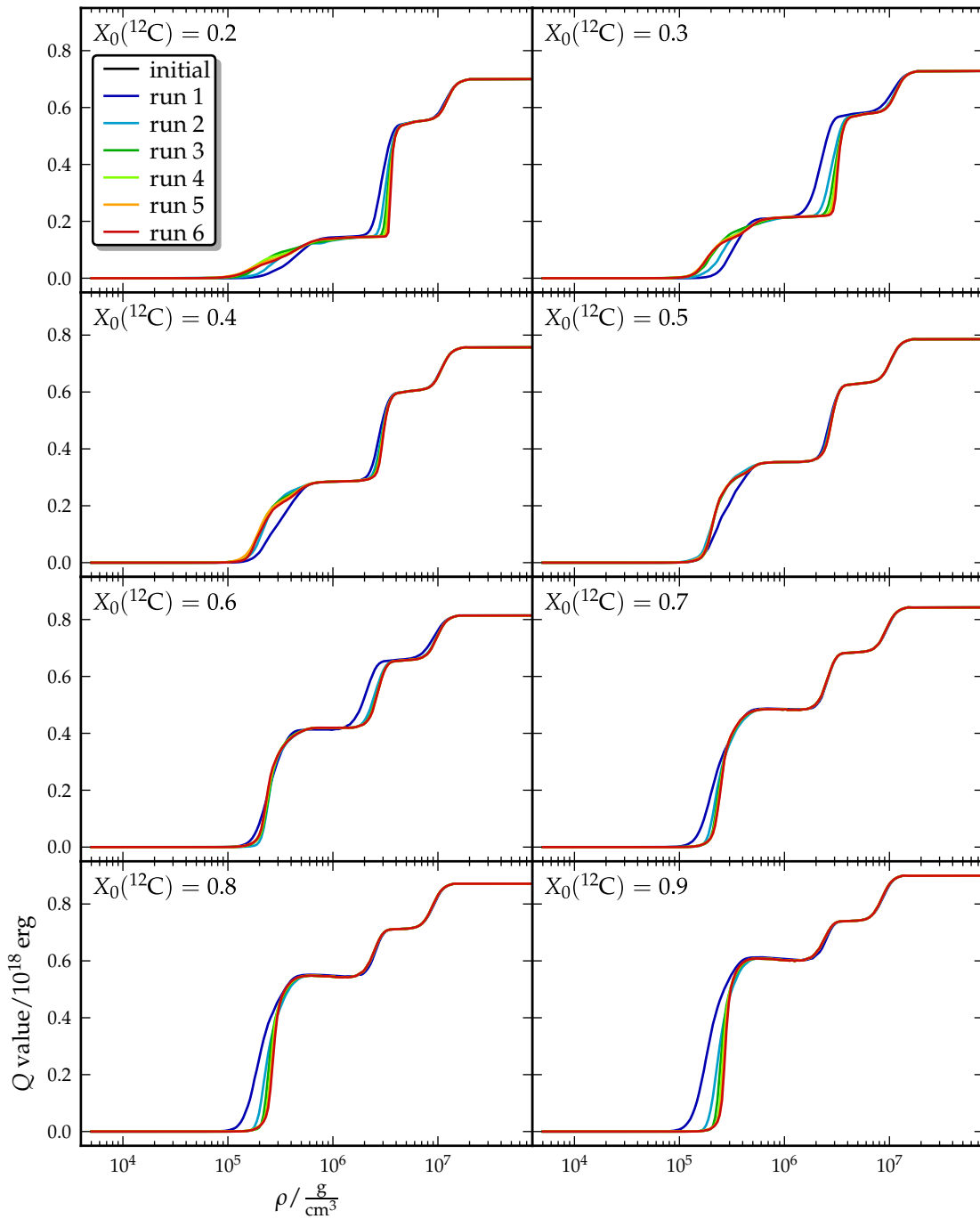


Figure 4.3 | Detonation Q value comparison. In each plot, the Q value of the detonation abundance table for a given carbon mass fraction is compared for the subsequent calibration runs. For each carbon mass fraction from 0.2 to 0.9, the Q value is plotted against the density of the unburned material.

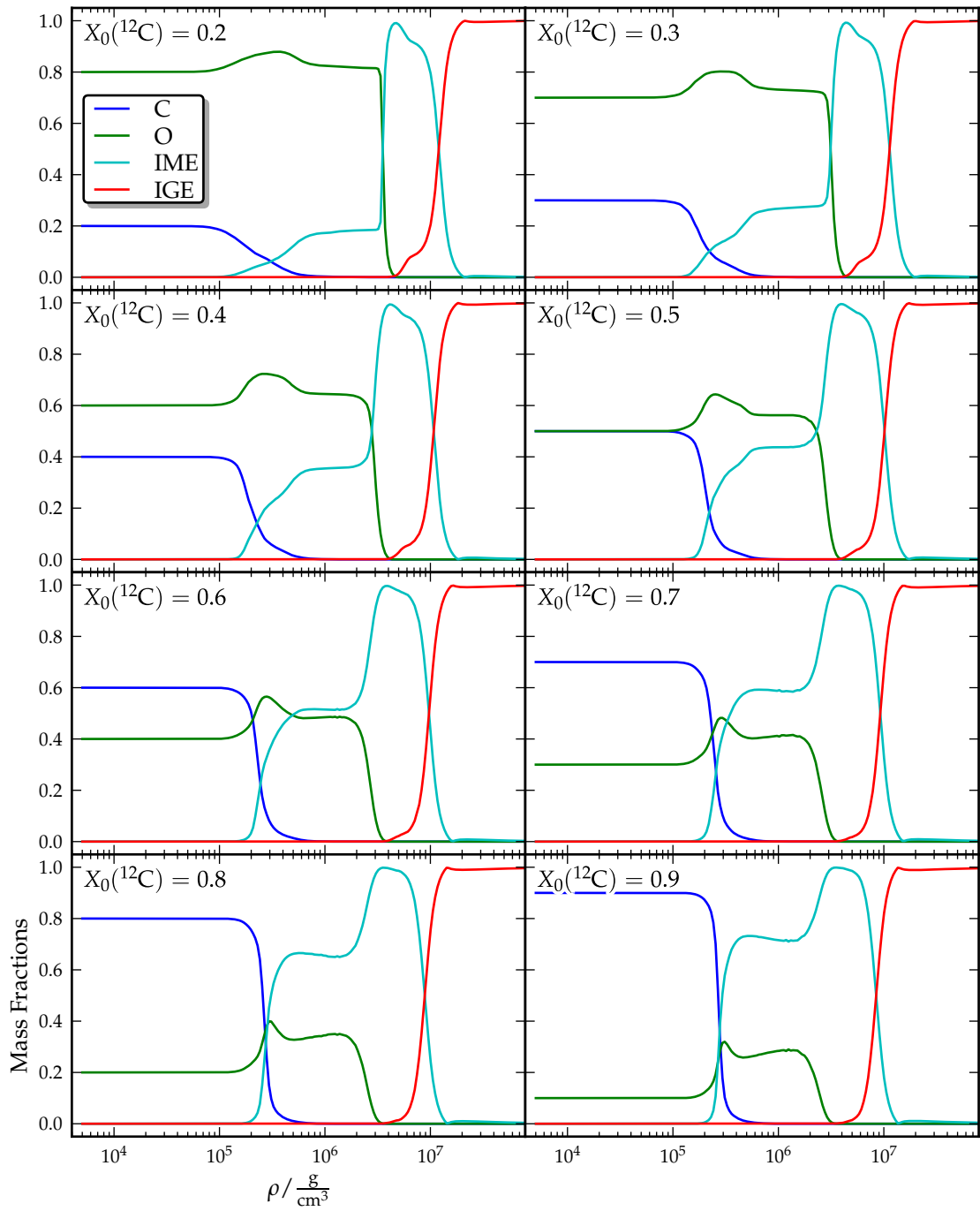


Figure 4.4 | Final detonation abundance tables. Each plot shows the abundance table for the corresponding initial carbon mass fraction ranging from 0.2 to 0.9. Plotted are the mass fractions of the simplified composition used by the levelset method against the logarithm of the density of the unburned fuel.

A comparison of the Q value tables of the separate iteration runs for carbon mass fractions from 0.2 to 0.9 is shown in Figure 4.3. The relative errors of the Q values are not shown here as they are similar to the case $X_0(^{12}\text{C}) = 0.5$ (see Figure 4.2). The tables behave very similarly for the separate carbon mass fractions and reasonable convergence can be assumed in all cases in the important density range.

The final abundance tables for the detonation calibration are given in Figure 4.4. Shown are the mass fractions of the simplified chemical composition used by the levelset method. The abundance tables share a similar overall shape with clearly separated transitions to the distinct burning stages: carbon burning, oxygen burning and silicon burning. The most noticeable difference in the abundance tables can be seen for the plateau emerging after the transition to carbon burning, with the logarithm of the density roughly being between 5.5 and 6.5. This plateau rises for higher initial carbon mass fractions, meaning the carbon burning produces higher amounts of intermediate mass elements at the same initial density for higher carbon mass fractions. On the one hand this affects the chemical outcome in the explosion process. On the other hand this raises the Q value rather strongly for higher carbon mass fractions especially in this region. Above the transition to oxygen burning—at a logarithmic density of about 6.5—the shape remains quite similar for all carbon mass fractions, albeit the transition to silicon burning shifts slightly to lower densities for higher carbon mass fractions.

The impact of the initial carbon mass fraction on the Q value table is threefold, as displays Figure 4.5 A:

1. The global reaction Q value rises with rising initial carbon mass fraction. This can be explained by the different binding energies of carbon and oxygen: The binding energy of carbon is lower than that of oxygen, resulting in a higher difference to the burning products. Hence, a higher carbon abundance in the fuel leads to more nuclear energy being released during the reaction—thus to a higher Q value.

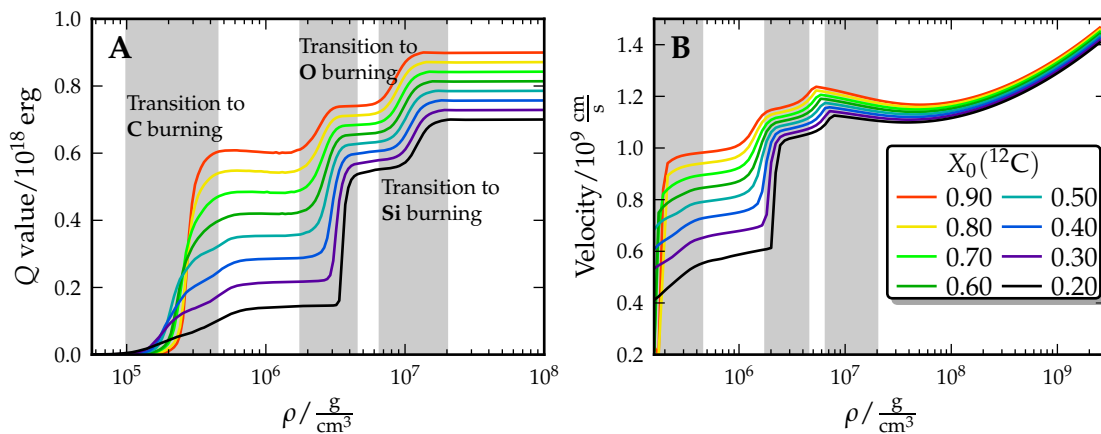


Figure 4.5 | Comparison of final detonation tables. Plotted are the final Q values (A) and detonation propagation velocities (B) for different carbon mass fractions against the density of the unburned material. The transition zones to the different burning stages—onset of carbon, oxygen and silicon burning—are marked in gray.

2. The increase in the Q value above the carbon burning threshold until the onset of oxygen burning is higher than the average increase. As stated above (also compare Figure 4.4), a higher production of intermediate mass elements is encountered for higher carbon mass fractions in this density range, consequently raising the Q value.
3. The transitions to the oxygen and silicon burning stages—marked in gray in Figure 4.5 A—shift to lower densities with higher carbon mass fractions. The transition to the carbon burning stage stays nearly constant. The shift of the oxygen and silicon burning threshold combined with the higher Q value for higher carbon mass fractions augments the explosion strength: more energy is released at even lower densities than for lower carbon mass fractions.

The detonation propagation velocity is affected by a varying carbon mass fraction mainly through the reaction Q value—which is used as input for the detonation speed computation (Section 3.3). For each carbon mass fraction, the detonation propagation velocity is plotted in Figure 4.5 B. A global tendency to higher velocities for higher carbon mass fractions can be recognized, being induced by the higher Q value (compare Figure 4.5 A). The largest differences in propagation speed are located in the density interval of carbon burning—also the location of the largest differences in the Q value.

The main consequences of the mentioned properties are that the detonation burning front decreases in strength and propagation velocity with decreasing carbon mass fraction.

4.1.2 Deflagrations

In order to generate the necessary abundance tables for the levelset method, the same iterative procedure has been employed as for detonations. Because the laminar burning speed has been computed in simulations, a fitting formula is taken from Timmes & Woosley (1992), which interpolates in density and carbon mass fraction. Hence, the additional step of computing the propagation velocities is not necessary in this case. But as discussed in Section 2.3.3, the flame propagation is dominated by the turbulent energy, hence the laminar burning speed is not very important for the deflagration.

The deflagration burning starts with laminar burning from the ignition kernels (using the C3 model by Reinecke et al., 1999a) and consequently evolves into turbulent burning, finally leading to a wrinkled flame. Due to the subsonic and turbulent propagation of the flame—opposed to the supersonic detonations—the iterative calibration does not converge as well as for detonations. As the flame structure is inherently multidimensional for deflagrations, a two dimensional distribution of tracer particles is used to track the nucleosynthesis. Since the propagation of the flame is subsonic, the tracer particles follow the expansion of the WD and at the time of the levelset crossing, their density has decreased from the initial value.

Moreover, the turbulent nature of the flame leads to a large scatter in the final outcomes of the tracer particles with respect to the density at the crossing time of the levelset. Hence, the final yields are binned in the logarithm of the burning density and in each

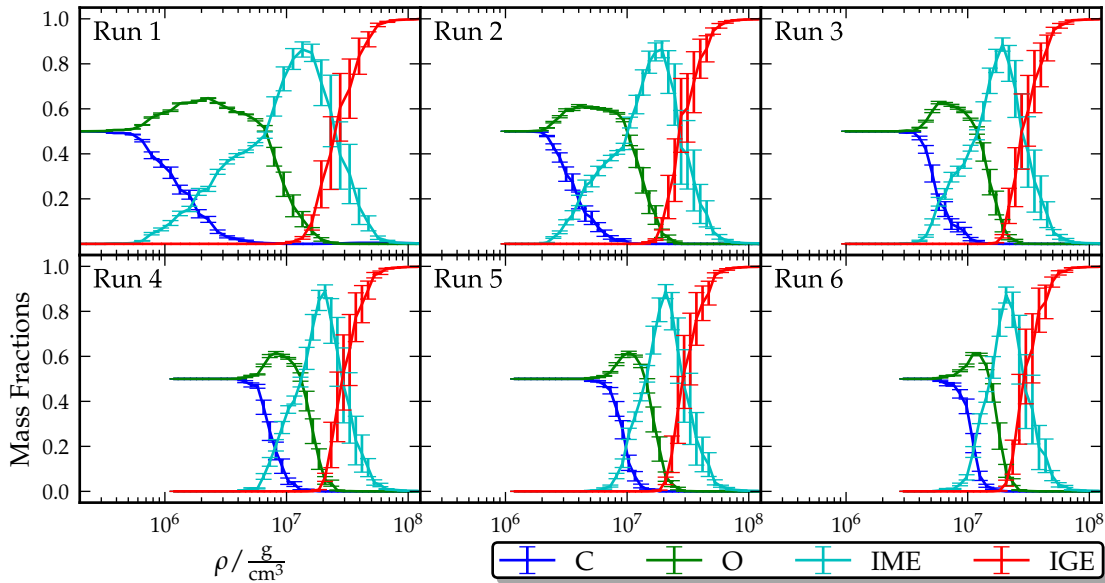


Figure 4.6 | Abundance tables for deflagration calibration with $X_0(^{12}\text{C}) = 0.5$. Shown is the mass fraction of the simplified chemical composition over the logarithm of the density as calculated from the detailed nucleosynthesis postprocessing. For each density bin, the average of the mass fraction for all tracer particles in this bin is computed. The error bars show the standard deviation in the corresponding interval.

density bin the average and standard deviation of the mass fractions are calculated. The scatter resulting in high standard deviations could be diminished by only taking into account tracer particles reaching their peak temperature at most 0.2 s after the levelset crossing. This method is demonstrated in Figure 4.6, where the abundance tables are compared for the consecutive iteration runs for $X(^{12}\text{C}) = 0.5$. The error bars display the standard deviation in the corresponding density bins. The overall shape of the abundance tables for the iteration runs is similar, although the transitions to the distinct burning stages shift more than in the detonation calibration. The error bars are in general not too large, so that the uncertainty of the abundance tables is not too high. They are somewhat larger at the silicon burning threshold, where still a certain amount of scatter remains. The error bars are similar for the other carbon mass fractions and are thus omitted in the following figures.

The large scatter occurring in the calibration of the deflagration tables is caused by the turbulent nature of the deflagration burning front. This leads to tracer particles, which do not simply cross the burning front, but are advected in the flow. As an example, one of these “pathological” tracer particles is examined in more detail in Figure 4.7. As can be seen from the hydrodynamical evolution (Figure 4.7 A, B, C), this particular tracer particle remains unburnt for a long time but is engulfed by the ashes. This leads to heating by diffusion of hot ashes into this small pocket of unburnt material. The tracer particle crosses the level set very late (~ 1.6 s), when the small pocket is finally burned out. The temporal evolution of the temperature (Figure 4.7 D) shows that the maximum

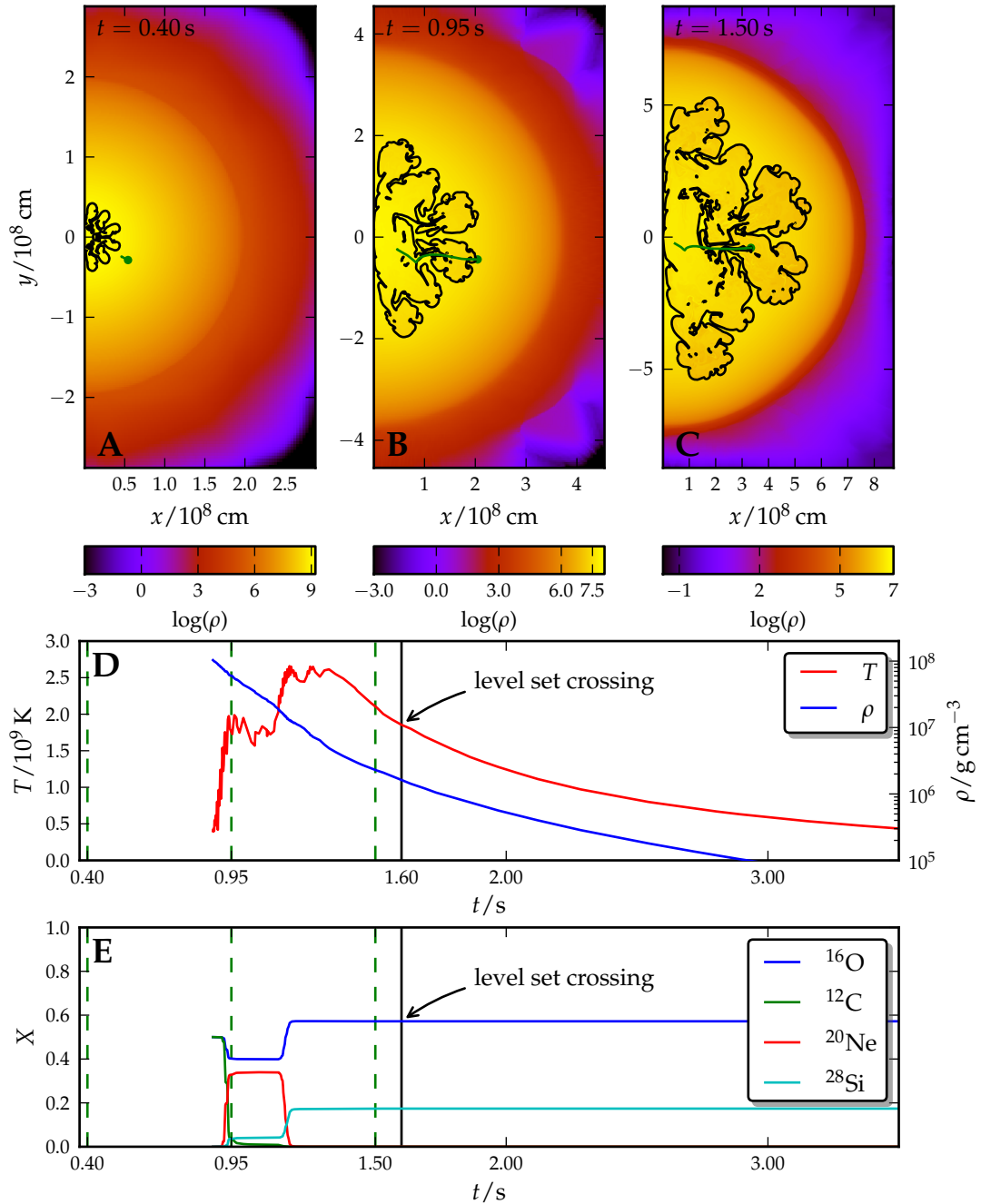


Figure 4.7 | A “pathological” tracer particle. The top row (panels A, B, C) shows the hydrodynamical evolution in the density of the last run of the deflagration calibration for $X(^{12}\text{C}) = 0.5$. The logarithm of the density is shown color-coded at the times 0.40 s, 0.95 s and 1.50 s. The green line shows the track of the tracer particle number 4796 up to the corresponding time. Panel D displays temperature (red) and density (blue) of the tracer particle in the course of time, panel E the chemical composition. The dashed green lines mark the positions of the hydrodynamical snapshots. The black line marks the point in time, when the tracer particle crosses the level set.

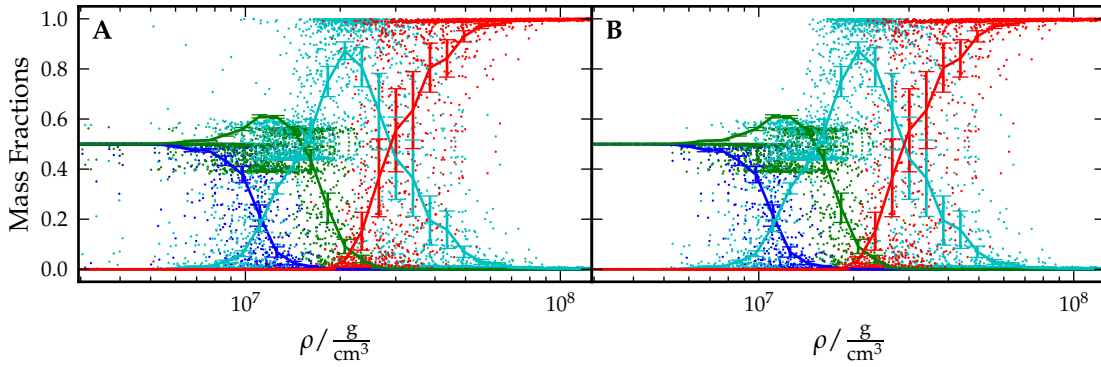


Figure 4.8 | Reducing scatter with a time restriction. Shown is the deflagration abundance table for $X(^{12}\text{C}) = 0.5$ for the sixth calibration run without (A) and with (B) a time restriction criterion for the selection of the tracer particles. The solid lines display the mean values with errors for the abundances. The number of tracer particles is 5727 (A) and 4220 (B), respectively. The scatter is reduced especially in the low density part.

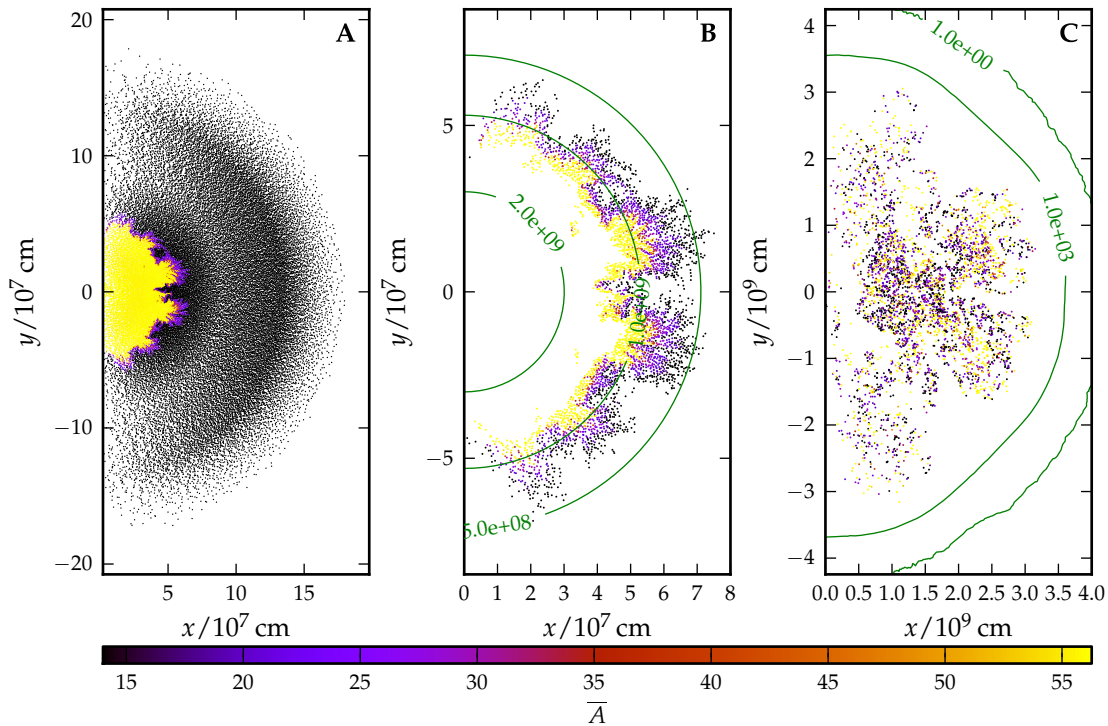


Figure 4.9 | Spatial distribution of selected tracer particles. Panel A displays the initial spatial distribution of all tracer particles, colored by their final mean atomic number \bar{A} . Panel B shows the initial, panel C the final spatial distribution of the selected tracer particles (as in Figure 4.8 B), colored by their final mean atomic number \bar{A} . Contour lines of the density are shown in green. The turbulent burning leads to a strong mixing in the final locations (C). The impact of the Rayleigh-Taylor “fingers” is visible in A and B.

of temperature occurs well before the level set crossing. The first spike in temperature already leads to a substantial amount of reactions (compare the chemical composition, Figure 4.7 E), as temperatures of several GK are reached. Now the reason why this tracer particle increases the scatter, is that the burning density is recorded at the level set crossing time (Figure 4.7 D), which does not correspond to the time—and hence, the density—where the reactions occur. This is just one example of a “pathological” tracer particle and many other, different cases may occur.

In order to reduce the scatter caused by similar tracer particles, an additional criterion was introduced. The time difference between maximum temperature and level set crossing must be positive, but smaller than 0.2 s. This ensures that the level set is first crossed before the burning starts. The effect of this restriction is visualized in Figure 4.8. The points in this plots show the final abundances of all tracers falling in this density range and the mean values with standard deviations for a binning in the density. The time restriction removes about 1500 tracer particles and reduces the scatter especially in the lower density range.

A detailed view of the tracer particles used in the calibration is shown in Figure 4.9. The final mean atomic number \bar{A} is shown for the tracer particles at the initial (A, B) and final positions (C). As can be seen in A, most tracer particles either do not burn at all (black) or burn to NSE (yellow). The intermediate range is shown in (B), where the tracers selected using the time restriction criterion are shown in their initial positions. The effect of the Rayleigh-Taylor instability can be clearly seen in the mushroom-shaped fingers. Panel C displays the final positions of the tracer particles which are strongly mixed due to the turbulent motion during the burning.

As in the detonation case, the comparison of different runs for each carbon mass fraction during the iterative procedure is facilitated by the use of reaction Q value tables. The comparison of these Q value tables in Figure 4.10 shows that the different burning stages are not obviously separated when looking at the Q value—whereas the abundance tables show the different burning stages. In contrast, this distinction is clearly seen in the abundance tables for detonations (compare Figure 4.3). Also, the change from one iteration to the next is higher and the convergence is slower than in the detonation case. Nevertheless, the difference in the reaction Q value between consecutive runs diminishes in the course of the calibration procedure and hence, the error made by assuming convergence after the sixth iteration should be small enough—at least compared to the errors introduced by other assumptions in the model. Moreover, the biggest changes in the tables are still at low densities below $\sim 10^7$ g/cm³. As the DDT leads to a ignition of a detonation at about this density, the fuel at lower densities is almost completely burned by the supersonic detonation. Therefore, this lower density regime does not have a big impact on the delayed detonation simulations presented in this work.

The reason why the convergence is not as good as in the detonation models lies partly in the subsonic and partly in the turbulent nature of the burning. As the burning proceeds subsonically, the WD is pre-expanded and the density ahead of the burning front decreases. But one reason for the iteration scheme to work well was that the burning density is not affected much by a higher Q value. Naturally, this is fulfilled for detonations better than for deflagrations. On the other side, the turbulent nature of the

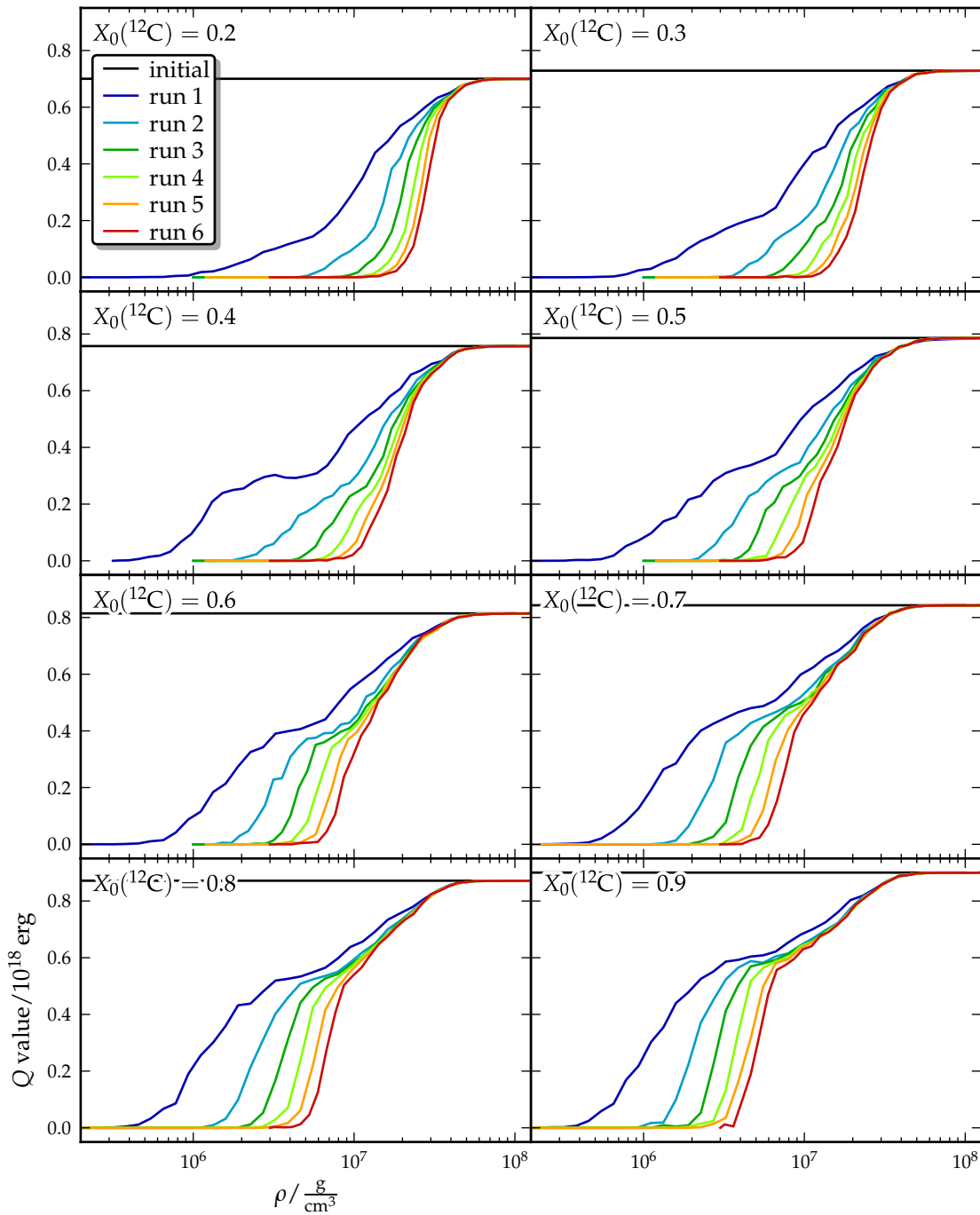


Figure 4.10 | Deflagration Q value comparison. In each plot, the Q value of the deflagration abundance table for a given carbon mass fraction is compared for the subsequent calibration runs. For each carbon mass fraction from 0.2 to 0.9, the Q value is plotted against the density of the unburned material.

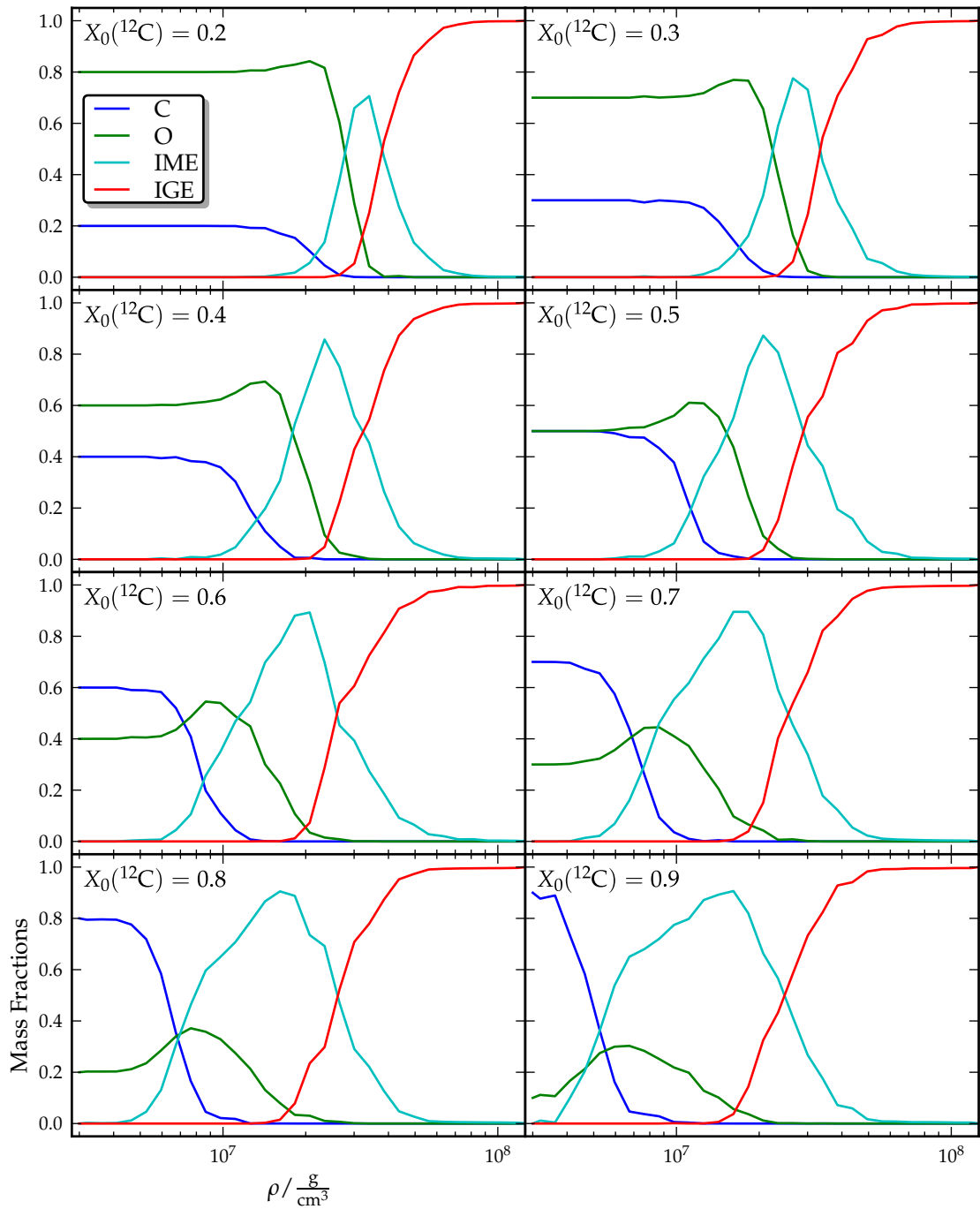


Figure 4.11 | Final deflagration abundance tables. Each plot shows the abundance table for the corresponding initial carbon mass fraction ranging from 0.2 to 0.9. Plotted are the mass fractions of the simplified composition used by the levelset method against the logarithm of the density of the unburned fuel.

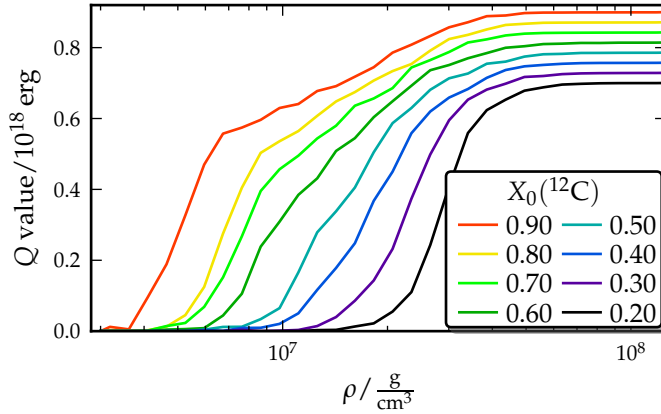


Figure 4.12 | Comparison of final deflagration tables. Plotted are the final Q values for different carbon mass fractions against the density of the unburned material.

burning front leads to random distributions of the tracer particles and thus to scatter occurring in the tables.

The final abundance tables after the last iteration run are shown in Figure 4.11, where the mass fractions for the simplified chemical composition are plotted against density. Here, similar tendencies as for the detonation tables (Figure 4.4) can be seen: the transitions to the distinct burning stages shift to lower densities for larger carbon mass fractions. Moreover, the plateau of IME production following the carbon burning threshold rises for higher carbon mass fractions, leading to a higher nuclear energy release. Unlike in the detonation abundance tables, also the transition to carbon burning shifts to lower densities for larger carbon mass fractions. Hence, the density range from the onset of carbon burning to complete burning to NSE is larger for higher carbon mass fractions.

These properties also show up in the comparison of the final reaction Q value tables for different carbon mass fractions in Figure 4.12. The energy deposition behind the burning front is greatest for the highest carbon mass fraction and then steadily decreases to lower carbon mass fractions. At high densities, when burning to NSE, this is explained by the lower binding energy of carbon compared to oxygen—being equal to a higher energy difference to the tightly bound NSE material. At lower densities, the higher Q value is on the one hand caused by the plateau in IME productions (similar to detonations), on the other hand by the shift of the burning transitions to lower densities. These burning thresholds are not clearly distinct in the Q value table.

This leads to the conclusion that turbulent deflagration burning is less vigorous for lower carbon mass fractions due to the lower energy release.

4.2 2D Simulations

In order to study the impact of the chemical composition on thermonuclear supernovae, a series of 2D simulations—hydrodynamics and postprocessing—with different initial composition models has been conducted using the supernova code LEAFS (Section 3.1.3). In principle, 3D simulations are more accurate, as they allow for a more realistic treatment of the turbulent flow. But as they are also computationally very expensive, only a small

Table 4.1 | DDT criteria used in the 2D simulations. For each DDT criterion, the minimum and maximum densities ρ_{\min} and ρ_{\max} as well as the critical Karlovitz number Ka_{crit} are given.

Criterion	$\rho_{\min}/10^7 \text{ gcm}^{-3}$	$\rho_{\max}/10^7 \text{ gcm}^{-3}$	Ka_{crit}
ddt1	0.6	1.2	250
ddt2	0.5	0.8	1000
ddt3	0.5	0.8	2250
ddt4	0.6	1.2	2250

Table 4.2 | Ignition configurations for 2D simulations. For each ignition condition, the number of kernels N_k (radius $r_k = 6 \text{ km}$) and the minimum distance between the midpoints of two adjacent kernels, r_{\min} , are given.

Name	N_k	r_{\min}/r_k
ddo3	100	0.5
ddo4	100	0.1
ddo5	50	0.8
ddo6	20	1.0
ddo7	80	0.8
ddo8	90	0.7
ddo9	150	0.3
dd10	60	0.7

number of 3D simulations could be computed (Section 4.3). The suite of 2D simulations includes simulations for different initial compositions with homogeneous carbon mass fractions as well as varying carbon mass fractions, which should be more realistic (cf. Section 2.4). The nucleosynthetic results of these models are given in Appendix A, Table A.1.

4.2.1 Initial Models

Using different initial models, the burning process has been modeled for several ignition conditions and DDT criteria. Each model name is composed of three parts:

1. The first part indicates the initial composition model. The composition of the models cXY is homogeneous with a carbon mass fraction of XY%. The central density is $2.9 \times 10^9 \text{ g/cm}^3$. The models rp1 and rp2 (“realistic progenitor”) are models with varying carbon mass fractions. The inner carbon mass fraction (rp1: 0.32, rp2: 0.28), which is homogeneous in the convective core of a certain mass (rp1: $0.98 M_{\odot}$, rp2: $1.07 M_{\odot}$), is smoothly joined to the outer accretion layer above $1.2 M_{\odot}$ with a carbon mass fraction of 0.5. The central density is taken to be $2.9 \times 10^9 \text{ g/cm}^3$ (rp1) and $4.7 \times 10^9 \text{ g/cm}^3$ (rp2). All these values are chosen to be consistent with Lesaffre et al. (2006). In order to study the effect of the size of the convective core, a series of initial models was created with varying sizes of the convective core. All models have an homogeneous initial temperature distribution with $T = 5 \times 10^5 \text{ K}$.

2. The second part denotes the DDT criterion which was employed in the corresponding simulation. The DDT criterion for 2D simulations is discussed in Section 3.1.3. A DDT is supposed to occur in cells which lie in a certain density range and have Karlovitz numbers above a critical value of Ka_{crit} . The detailed conditions employed here are given in Table 4.1 and are similar to the ones used by Kasen et al. (2009).
3. The last part of the model name gives the ignition configuration. The deflagration flame was ignited in a certain number of kernels N_k with a radius of $r_k = 6$ km, which were randomly distributed according to a Gaussian distribution in radius in an area with a maximum radius of 150 km. For each configuration, a minimum distance r_{min} between the ignition kernels was established. The properties of the different ignition conditions are given in Table 4.2. These conditions are the same as used by Kasen et al. (2009), although with a different labeling.

The hydrodynamical simulations are carried out in an axisymmetric configuration with a grid size of 512×1024 cells. Using the hybrid moving mesh technique, this corresponds to an initial resolution of 1.06 km in the innermost part. The tracer particles are distributed with variable tracer masses, as discussed in Section 3.1.3. This method yields about 41000 tracer particles for each simulation. In the postprocessing step, the solar metallicity by Asplund et al. (2009) was used as the initial composition. In order to preserve the particle number, the sum of the mass fractions of all elements above oxygen is subtracted from the initial carbon mass fraction.

4.2.2 Hydrodynamical Evolution

The hydrodynamical evolution of delayed detonation models is split into two parts—the deflagration phase and the detonation phase. The explosion starts with an ignition of the deflagration in a number of circular ignition kernels. After a short period of laminar burning, Rayleigh-Taylor instabilities emerge and speed up the flame propagation by inducing turbulence. Several such Rayleigh-Taylor fingers form while the hot ashes are rising to the surface of the WD. The form of these fingers is mostly dominated by the ignition kernels which are farthest away from the center. The turbulence induced by the Rayleigh-Taylor and Kelvin-Helmholtz instabilities leads to a highly convoluted and wrinkled flame. Since the deflagration burning front propagates subsonically, the whole WD is expanded during this phase. After the burning regime changes from the flamelet regime to the distributed burning regime, the deflagration turns into a detonation by spontaneous ignition of a detonation. This detonation consumes the rest of the WD and leads to a layered structure in the outer part of the ejecta.

Three examples for the hydrodynamical evolution of 2D models are shown in Figure 4.13. The models were selected by requesting a similar ^{56}Ni mass and thus a similar brightness. Each row shows the evolution of one model. The first three columns show plots of the density at different times; the deflagration and detonation flame fronts are indicated by the zero level sets of the corresponding level set functions. One characteristic feature of 2D simulations, which can be seen here, is that the mixing of hot ashes and

4 Results

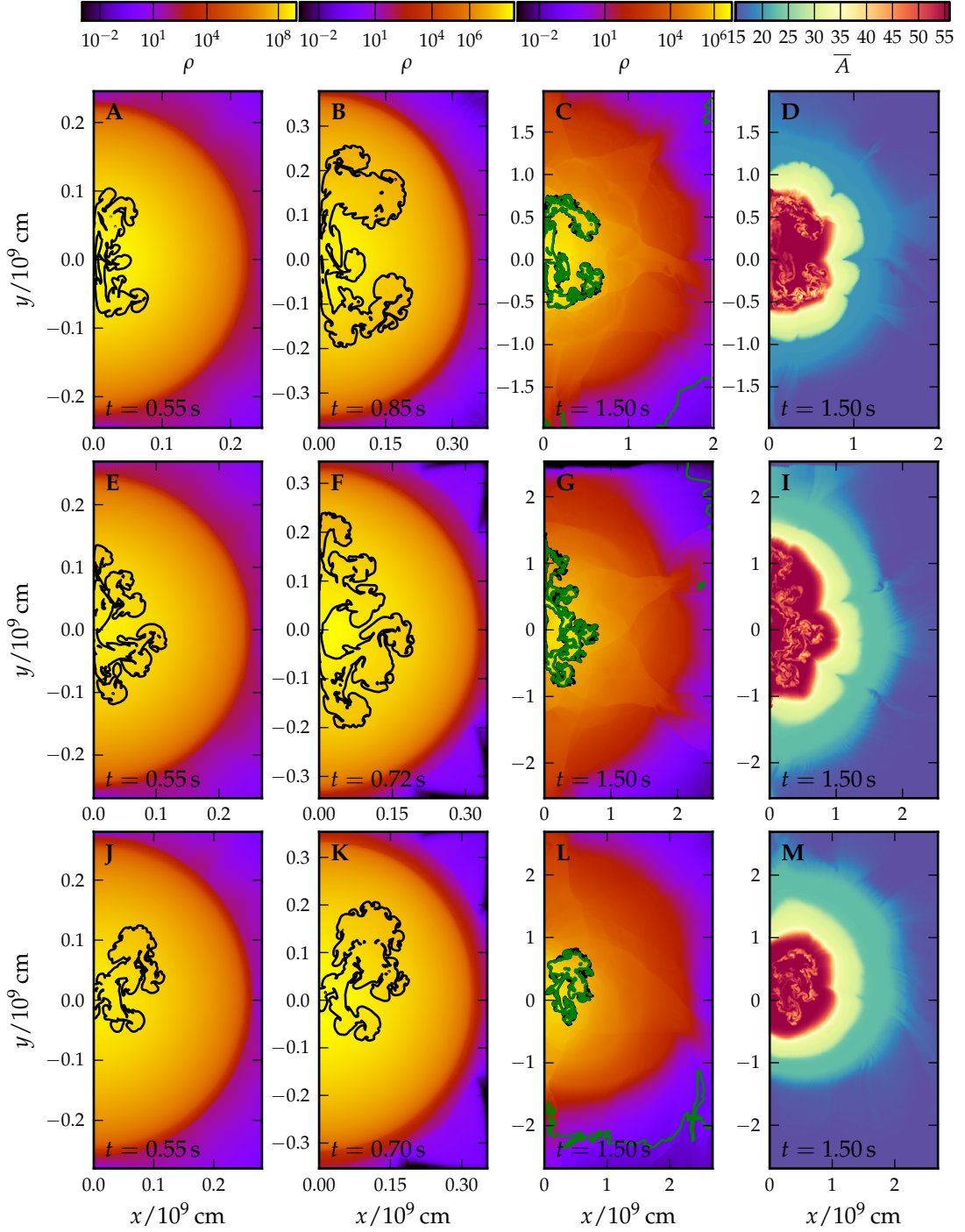


Figure 4.13 | Hydrodynamical evolution of three 2D models. The first three columns show the density, the last column the mean atomic number of the hydrodynamical models at the denoted times. The level sets of the deflagration and detonation are plotted in black and green, respectively. The second column is at the time of the first DDT. The first row (A-D) plots the model `c30_ddt2_ddo4` ($M(^{56}\text{Ni}) = 0.784 M_{\odot}$), the second row (E-I) the model `c50_ddt2_ddo8` ($M(^{56}\text{Ni}) = 0.725 M_{\odot}$) and the third row (J-M) the model `rp1_ddt1_ddo7` ($M(^{56}\text{Ni}) = 0.734 M_{\odot}$).

fuel is not as strong as in 3D simulations. Depending on their hydrodynamical evolution, the detonation is initiated at different times. The states just before the DDT are displayed in the second column, where the form of the deflagration flame front depends on the initial distribution of ignition kernels. The third column shows the three models at 1.5 s, after the detonation consumed almost all remaining fuel. In the outer layers, tapered structures are visible, where the density is higher. These result from merging detonation wavefronts, when the hydrodynamical shocks of each wavefront propagate through the ashes of the other wavefront. In the last column, the mean atomic number \bar{A} indicates the simplified chemical composition as obtained from the hydrodynamical simulations. In the outer parts, a layered structure can be seen, which is caused by the detonation propagating through the low-density outer parts of the star. In the core, iron group elements are formed and the burning products of the deflagration and the detonation are mixed. In the outer layers, IME and some O are synthesized until the density drops below the corresponding threshold.

Differences between the three models, which can be attributed to their initial composition and not to other factors—such as the ignition configuration and DDT criterion—can

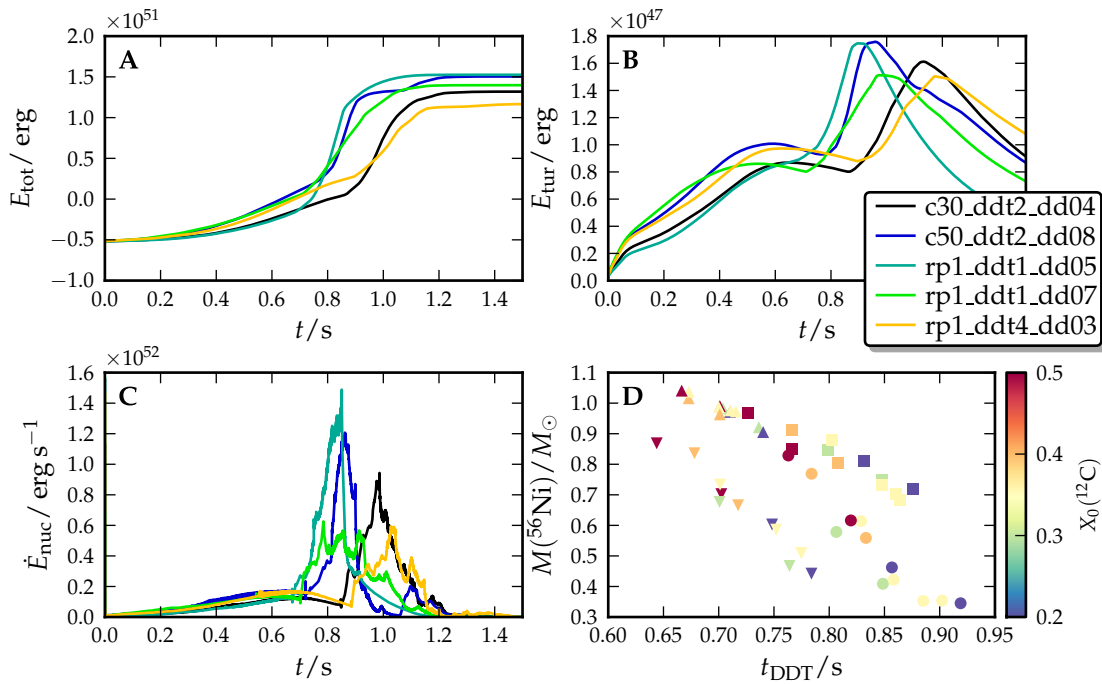


Figure 4.14 | Global properties of 2D simulations. In the first three panels, global properties are plotted against the simulation time for five models (the three models from Figure 4.13, one bright model, rp1_ddt1_dd05, with $M(^{56}\text{Ni}) = 1.04 M_{\odot}$ and one faint model, rp1_ddt4_dd03, with $M(^{56}\text{Ni}) = 0.353 M_{\odot}$). Panel A displays the total energy, panel B the turbulent energy and panel C the nuclear energy generation rate. Panel D shows the total ^{56}Ni mass against the time of the first DDT for selected ignition conditions (circles: ddo3, squares: ddo4, upward triangles: ddo5, downward triangles: ddo7) and selected initial models (c20, c30, c40, c50, rp1). The models are colored by their initial total carbon mass fraction.

be seen especially in the outer layers. The model with a homogeneous carbon mass fraction of 0.3 (top row) shows more unburnt material in the outer layers in the final state, as indicated by the lower mean atomic number. The model with a homogeneous composition of $X_0(^{12}\text{C}) = 0.5$ shows more intermediate mass elements and also oxygen at higher radii (i.e. at higher velocities). The realistic progenitor composition model (rp1) shows properties in between these two extremes.

Some global properties of the same three models are depicted in Figure 4.14 together with one bright model (rp1_ddt1_ddo5, $M(^{56}\text{Ni}) = 1.04 M_\odot$) and one faint model (rp1_ddt4_ddo3, $M(^{56}\text{Ni}) = 0.353 M_\odot$). Panel A shows the evolution of the total energy of the WD during the explosion phase. All models have final total energies above 10^{51} erg and are thus completely unbound. The initiation of the detonation in the DDT can be seen at the point where the total energy rises sharply. The faintest model (yellow) has the latest DDT time and also the lowest total energy release. The brightest model, on the other hand, shows the earliest DDT time and the highest energy release. In panel B, the turbulent energy from the subgrid scale model is shown. Before the DDT is initiated, this energy can be interpreted as a measure of the strength of the deflagration. One can see in general, that a strong deflagration phase—accompanied by a strong pre-expansion—may lead to fainter models, if the DDT occurs late enough. The second peak in the turbulent energy is caused by the detonation wave burning the remaining fuel. The nuclear energy generation rate is shown in panel C. As most of the nuclear energy is consumed very fast during the detonation, the energy generation rate peaks shortly after the initiation of the detonation. In general, the brighter models have a higher peak at earlier times.

Panel D of Figure 4.14 shows the total ^{56}Ni mass against the DDT time, colored by the total initial carbon mass fraction for selected ignition conditions (ddo3, ddo4, ddo5, ddo7) and selected initial models (c20, c30, c40, c50, rp1). This shows that for the same initial conditions, the ^{56}Ni masses decrease with larger DDT times. This is due to the pre-expansion of the WD being more pronounced at later times. Another trend visible here is that the DDT times are larger for lower carbon mass fractions for same ignition conditions. This indicates that the deflagration phase for lower carbon mass fractions evolves weaker and thus, the conditions for a DDT are reached later. The more pronounced pre-expansion then leads to lower ^{56}Ni masses.

The ignition conditions affect the produced ^{56}Ni mass through the evolution of the deflagration phase, which is influenced by the number and distribution of the ignition kernels. In general, a high number of ignition kernels induces a strong deflagration phase and contrarily for a low number of ignition kernels. Hence, analogously to above, a lower number of ignition kernels produces brighter events with higher ^{56}Ni masses. This can also be seen in Figure 4.14 D, where the upward triangles (ddo5, 50 ignition spots) are all above the circles (ddo3, 100 ignition spots), thus producing more ^{56}Ni .

4.2.3 Nucleosynthetic Yields

A summary of the most important nucleosynthetic yields from the postprocessing is given in Table A.1. The simulations cover a wide range of ^{56}Ni masses from $\sim 0.35 M_\odot$ to $\sim 1.05 M_\odot$, corresponding to a wide range in luminosities. Thus, they reproduce

a certain spread in brightness which is necessary to explain observations finding a diversity of SNe Ia (cf. Section 1.2).

The impact of the chemical composition on the ^{56}Ni yields for homogeneous progenitor compositions is compared in Figure 4.15 for two different DDT criteria. This figure clearly shows that the total ^{56}Ni mass decreases with decreasing carbon mass fraction for the same initial conditions. This is due to the different hydrodynamical evolution, as discussed in Section 4.2.2. For a smaller carbon mass fraction, the deflagration phase is less vigorous because of the lower reaction energy deposition (cf. the Q value table in Figure 4.12). This leads to a later initiation of the detonation as seen in Figure 4.14 D. Hence, the WD undergoes a stronger pre-expansion and the detonation wave burns material at lower densities and thus, less ^{56}Ni is produced. Moreover, the shift of the transition to Si burning to higher densities for lower carbon mass fractions acts in the same direction.

It can also be seen from Figure 4.15 that the progenitor composition affects models with lower ^{56}Ni masses more than simulations with higher ^{56}Ni masses. As discussed above, brighter events tend to result from weak deflagration phases with a weak pre-expansion, where the detonation is ignited early and burns a high amount of material to ^{56}Ni . As the deflagration phase is weak for these ignition conditions, it is not affected as strongly by the different C abundance as the stronger deflagration phases. Thus, the chemical composition mainly affects the detonation by shifting the transitions to the different burning stages. This only leads to a somewhat smaller amount of ^{56}Ni being produced. This can also be seen in Figure 4.14 D, where the upward triangles (corresponding to the bright ddo5 models) only show a small spread in the ^{56}Ni mass.

The detailed nucleosynthetic yield from three models are compared to the solar composition in Figure 4.16, which compares the mass fractions normalized to ^{56}Fe . The chemical composition of the Sun is taken from Asplund et al. (2009). The three models are the same as in Figure 4.13 and are similarly bright. The nucleosynthetic

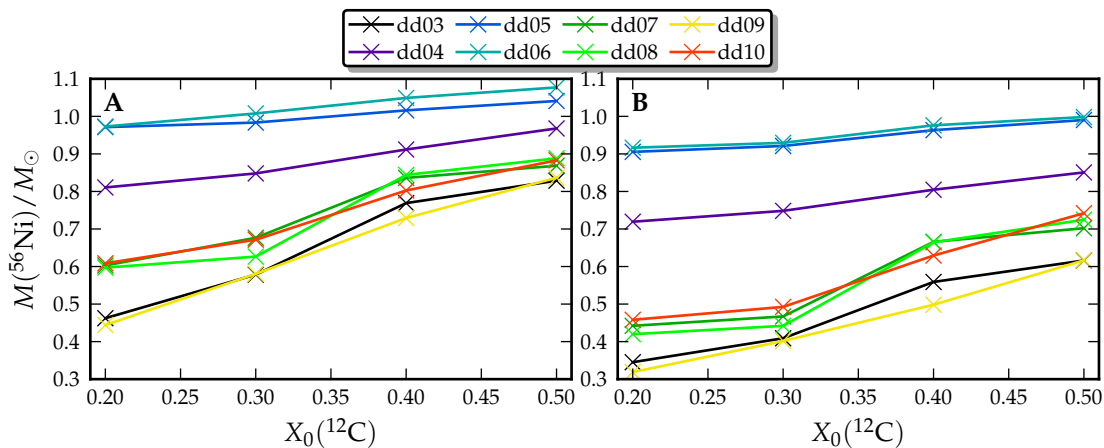


Figure 4.15 | ^{56}Ni masses for homogeneous 2D progenitor models. The total ^{56}Ni mass is plotted for different ignition conditions against the initial carbon mass fraction of the progenitor. Panel **A** displays the ^{56}Ni masses for the DDT criterion ddt1, panel **B** for ddt2.

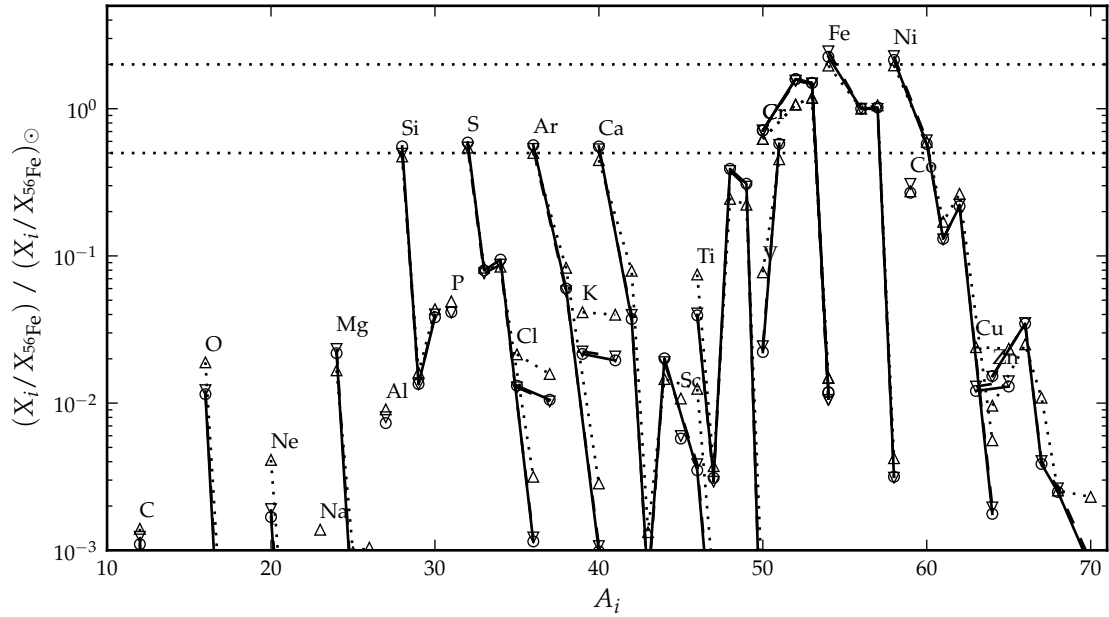


Figure 4.16 | Comparison of nucleosynthetic yields to solar composition for 2D models. The mass fractions of all isotopes normalized to ^{56}Fe are compared to the solar abundances from Asplund et al. (2009) and plotted against the mass number. Shown are the same models as in Figures 4.13 and 4.19: c30_ddt2_ddo4 (upward triangles/dotted lines), c50_ddt2_ddo8 (circles/solid lines) and rp1_ddt1_ddo7 (downward triangles/dashed lines). The horizontal dotted lines indicate over-/underproduction by a factor of two compared to the solar values.

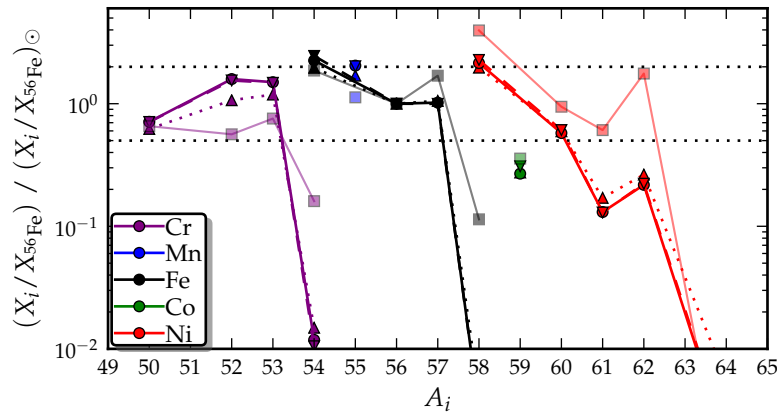


Figure 4.17 | Detailed comparison of iron group abundances to solar composition for 2D models. The mass fractions of iron group nuclei normalized to ^{56}Fe are compared to the solar abundances from Asplund et al. (2009) and plotted against the mass number. Shown are the same models as in Figures 4.13 and 4.19: c30_ddt2_ddo4 (upward triangles/dotted lines), c50_ddt2_ddo8 (circles/solid lines) and rp1_ddt1_ddo7 (downward triangles/dashed lines), as well as the W7 model (transparent squares/thin solid lines, Maeda et al., 2010). The horizontal dotted lines indicate over-/underproduction by a factor of two compared to the solar values.

yields from the postprocessing are followed until 2 Gyr after the explosion by decaying the corresponding radioactive nuclei. Figure 4.16 shows that the three models are very similar concerning their overall nucleosynthetic yields. Some intermediate mass nuclei (^{28}Si , ^{32}S , ^{36}Ar , ^{40}Ca) are produced at a level of roughly half the solar values. All these are α -nuclei being produced in the α -chain. The highest abundances occur in the iron group nuclei. These are given in more detail in Figure 4.17. Most Cr, Fe and Ni isotope abundances differ from the solar value less than by a factor of 2 (indicated by the dotted lines). Depending on the ratio of SNe Ia to SNe Ibc and SNe II, a certain overproduction of iron group nuclei is allowed when explaining the solar abundances in the galactic chemical evolution (Iwamoto et al., 1999). In Figure 4.17, the abundances are also compared to a recent version of the W7 model by Maeda et al. (2010). This model is known for reproducing observed spectra quite well, but was computed using a parametrized deflagration speed in one dimension. One can see that all Ni isotopes have lower abundances in our models compared to W7. This reduces the overproduction of ^{58}Ni , but shows an underproduction of neutron-rich nuclei.

The initial metallicity of the WD progenitor has a large impact on the nucleosynthesis results (e.g. Timmes et al., 2003; Travaglio et al., 2005). They find that the ^{56}Ni mass decreases linearly with the metallicity. In order to derive consistent conclusions, the effect of the metallicity on the hydrodynamical simulations has to be accounted for,

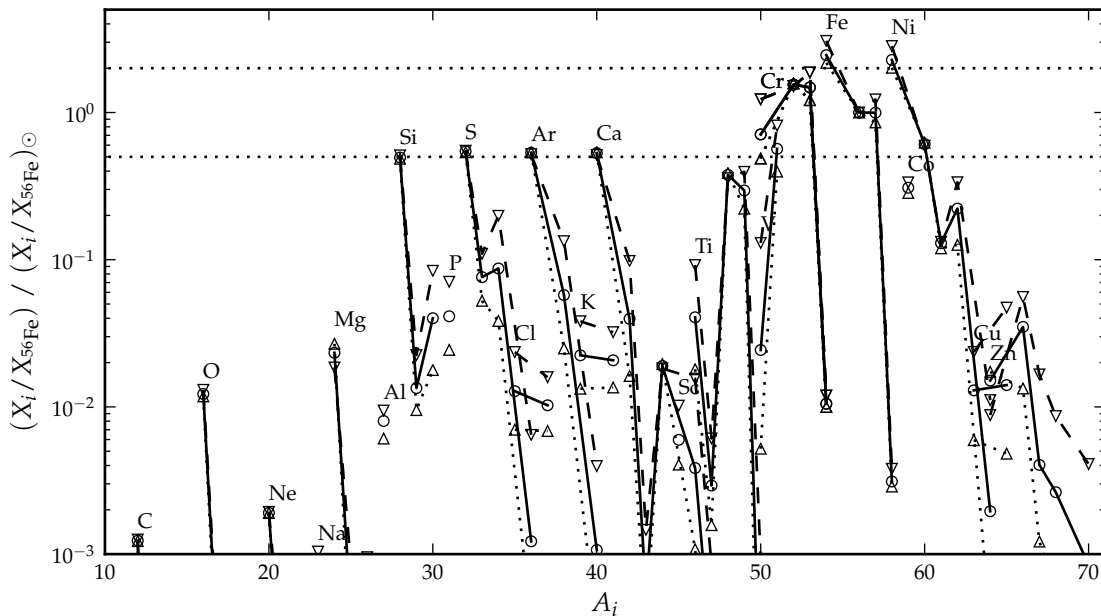


Figure 4.18 | Comparison of nucleosynthetic yields to solar composition for different metallicities. The mass fractions of all isotopes normalized to ^{56}Fe are compared to the solar abundances from Asplund et al. (2009) and plotted against the mass number. Shown are nucleosynthetic yields from the rp1_ddt1_ddo7 model with different initial metallicity in the postprocessing: solar metallicity Z_{\odot} (circles/solid lines), $0.5 Z_{\odot}$ (upward triangles/dotted lines) and $2 Z_{\odot}$ (downward triangles/dashed lines). The horizontal dotted lines indicate over-/underproduction by a factor of two compared to the solar values.

which influences the equation of state and thus the hydrodynamical evolution. This will be examined in detail in a forthcoming diploma thesis by A. Michel. In order to study the effect of metallicity on the nucleosynthesis of the current models, a simplified treatment has been employed: in the postprocessing, the initial composition was set to the solar composition by Asplund et al. (2009) and to scaled versions of these abundances by a factor of 0.5 and 2. The same trend is in Timmes et al. (2003) and Travaglio et al. (2005) is found that higher metallicities produce less ^{56}Ni : The model with half the solar metallicity produced $0.776 M_{\odot}$ ^{56}Ni , the model with solar metallicity $0.758 M_{\odot}$ and the model with double the solar metallicity $0.725 M_{\odot}$. A comparison of the corresponding nucleosynthetic yields (normalized to ^{56}Fe) to the solar composition is displayed in Figure 4.18 for the model `rp1_ddt1_ddo7`. A general trend of higher metallicity is the higher production of neutron-rich isotopes. At the same time, the two isotopes ^{54}Fe and ^{58}Ni have higher abundances compared to the abundance of ^{56}Fe .

4.2.4 Distribution of Ejecta in Velocity Space

In order to compute synthetic light curves and spectra, the distribution of the composition of the ejecta in the velocity space is important, as it determines the wavelengths of the escaping photons. After the end of our simulations at 100 s, the expansion of the ejecta is nearly homologous, i.e. the velocity of the ejecta is proportional to the radius and constant for each fluid element.

The detailed nucleosynthetic yields from the three models with similar ^{56}Ni masses as in Figure 4.13 have been averaged over all angles resulting in a one-dimensional distribution in velocity space at 100 s (Figure 4.19). The general structure is similar in all three models and consists of a core containing ^{56}Ni as well as some stable iron group elements. On top of the nickel core, layers of Si, O and C follow. One difference in the distributions is a shift in velocities due to the different kinetic energies. The `c30_ddt2_ddo4` model has the lowest asymptotic kinetic energy (1.33×10^{51} erg), followed by `rp1_ddt1_ddo7` (1.40×10^{51} erg) and `c50_ddt2_ddo8` (1.51×10^{51} erg), as expected from the initial composition (see also Table A.1). The ^{56}Ni , e.g., extends only up to $\sim 14\,500$ km/s for the `c30` model, but up to $\sim 17\,000$ km/s for the `c50` model. The `rp1` model lies in between these two models. One can also see a shift in the velocities of ^{28}Si , which decrease from the `c50` model over the `rp1` model to the `c30` model. Another difference is visible in the outer layers, where the `c30` model has a large amount of unburnt material compared to the other two models. This is due to the shift in transition densities in the detonation abundance tables, as the detonation in these outer layers does not produce IME for $X_0(^{12}\text{C}) = 0.3$, but only burns a certain amount of carbon to oxygen. In the other two models, initially consisting of material with $X_0(^{12}\text{C}) = 0.5$ in the outer layers, burning to IME is still possible for the detonation, and small amounts of IME are produced up to very high velocities. The density structure of the three models is relatively similar, but it falls off more rapidly for models with lower explosion energy.

These three models all have ^{56}Ni up to high velocities of roughly $15\,000$ km/s, which is probably too high. Seitenzahl et al. (2012) find in their study of three-dimensional models that the nickel extends only to velocities lower than $12\,000$ km/s. The high

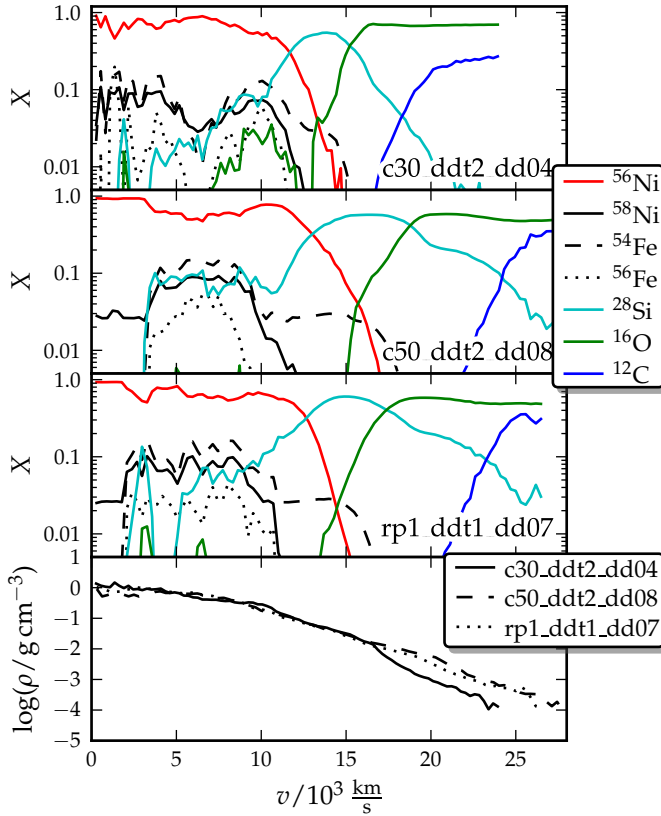


Figure 4.19 | Ejecta morphology in velocity space for similar nickel mass. The top three panels show angular averaged mass fractions of important isotopes in velocity space for the same models as in Figure 4.13, which have similar ^{56}Ni yields. The bottom panel shows the logarithm of the density for the three models in velocity space.

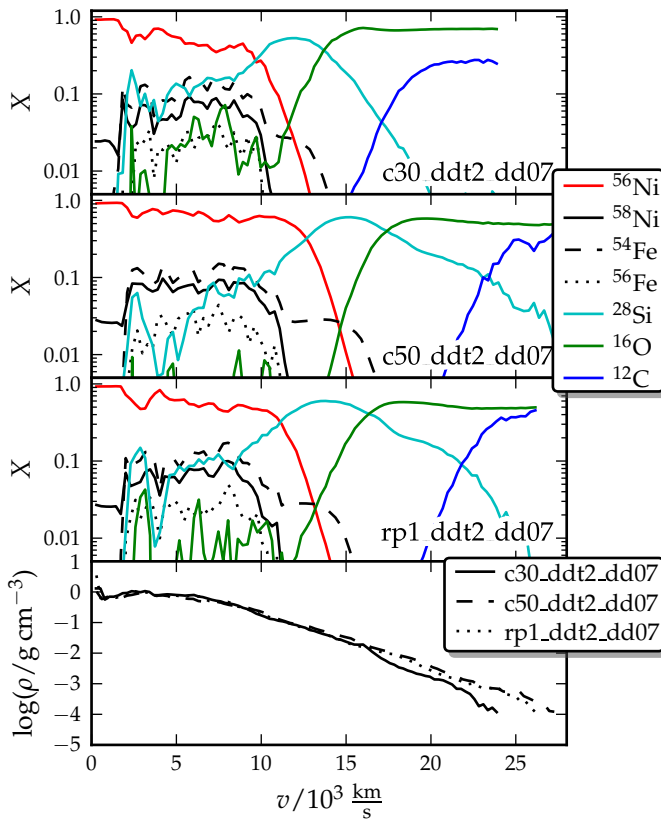


Figure 4.20 | Ejecta morphology in velocity space for same ignition configurations. The top three panels show angular averaged mass fractions of important isotopes in velocity space for the three models `c30_ddt2_dd07`, `c50_ddt2_dd07` and `rp1_ddt2_dd07`, with ^{56}Ni masses of 0.467, 0.702 and 0.586 solar masses, respectively. The bottom panel shows the logarithm of the density for the three models in velocity space.

Table 4.3 | Light curve properties. B_{\max} gives the absolute magnitude in the B band, $t(B_{\max})$ the rise time from explosion to B band maximum. $\Delta m_{15}(B)$ is the difference in magnitudes in the B band from maximum to 15 d after maximum, a characteristic quantity often compared by observers.

Model	B_{\max}	$t(B_{\max})/d$	$\Delta m_{15}(B)$
c30_ddt2_ddo4	-19.48	18.9	1.40
c50_ddt2_ddo8	-19.45	15.8	1.34
rp1_ddt1_ddo7	-19.42	17.2	1.31

velocities could also be due to the rather high ^{56}Ni mass of about $0.73 M_{\odot}$ produced in these models, which is near the upper bound for normal SNe Ia.

In Figure 4.20, three models with same ignition configuration and DDT criteria are compared. Here, one can see the same effect of the velocities shifting down for lower carbon mass fraction due to the lower kinetic energy, but more pronounced than for the models above. Also the composition in the outer layer is similar to the discussion above. In the inner layer, however, the rp1 model here is very similar to the c30 model, as the composition is similar ($X_0(^{12}\text{C}) = 0.32$ and 0.3 , respectively). Moreover, the velocities of the nickel core do not extend as far outwards as for the brighter models: in the c30_ddt2_ddo7 model up to $\sim 13\,000$ km/s, in the rp1_ddt2_ddo7 model up to $\sim 14\,000$ km/s and in the c50_ddt2_ddo7 model up to $\sim 15\,000$ km/s.

4.2.5 Synthetic Light Curves and Spectra

In order to compare the hydrodynamical simulations directly to observations of supernovae, calculations of radiative transfer through the ejecta have to be carried out, in order to compute synthetic light curves and spectra.

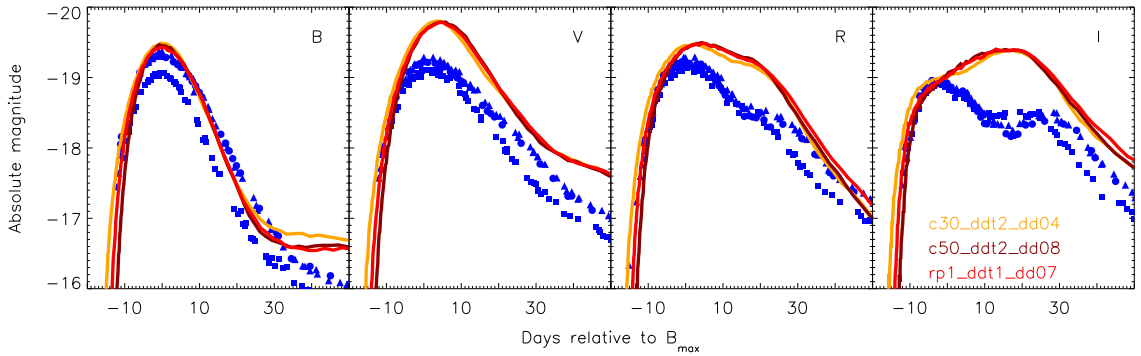


Figure 4.21 | Synthetic light curves for 2D models. The synthetic light curves in the B , V , R and I bands of the three models from Figures 4.13 and 4.19 are compared to three normal SNe Ia (in blue: o3du, o4eo and o5cf). The light curves are shifted in time to coincide at B band maximum. Note that the light curves are too red, especially in the R band. I thank M. Kromer for providing the synthetic light curves.

For the three models with similar ^{56}Ni mass (cf. Figure 4.13), radiative transfer calculations were performed by M. Kromer who kindly provided the synthetic light curves and spectra presented here. The calculations were done using the code ARTIS (Sim, 2007; Kromer & Sim, 2009), a multi-dimensional Monte-Carlo code modelling time-dependent radiative transfer. It follows the propagation of γ rays emitted mainly by ^{56}Ni and the subsequent reprocessing of radiation into the optical, including all relevant absorption and re-emission processes. Since the code does not use free parameters, a direct comparison of the synthetic light curves and spectra with observed data is possible.

Synthetic spectra computed with this code are for example used by Röpke et al. (2012) in order to compare synthetic spectra of a delayed detonation model and a violent merger model to the observed spectrum of SN 2011fe.

For this work, the ejecta distributions and density structure in velocity space shown in Figure 4.19 have been used as input for radiative transfer calculations. Although information about the somewhat asymmetric distribution of the ejecta is lost by angular averaging, this method has been chosen as it allows for computations which are not too expensive.

The resulting light curves are presented in Figure 4.21 together with light curves of three observed supernovae. Important properties are summarized in Table 4.3. All three models have a similar peak brightness in the B band of about -19.45 magnitudes. $\Delta m_{15}(B)$ shows slight differences for all three models. The rise time, however, differs by several days ranging from 15.8 d to 18.9 d. Although the light curve in the B band fits quite well up to about 30 d after B band maximum, the light curves in the redder bands are overestimated. Especially in the V band, the maximum is about 0.5 magnitudes too large. This may be explained by analyzing the ejecta morphology in the velocity space (Figure 4.19). The light curve is powered by the γ rays emitted in the radioactive decay of ^{56}Ni , which are reprocessed by material in the outer layers. In all models, stable iron group elements extend to high velocities also above the nickel core. These elements, including Cr, Ti and also Ni in the optically thin region absorb radiation at wavelengths in the UV and re-emit the radiation at higher wavelengths. This process probably causes the light curves to be very red compared to observed spectra.

This leads to the conclusion that the distribution of iron group elements in these models range up to velocities which are too high in order to explain light curves of normal SNe Ia.

This effect can also be seen in the synthetic spectra at B band maximum, which are compared to SN 2002er in Figure 4.22. SN 2002er is a normal Type Ia supernova with an estimate for the ^{56}Ni mass of $0.69 M_{\odot}$ (Kotak et al., 2005). One can see that the flux at short wavelengths $\lesssim 3600 \text{ \AA}$ is too low compared to the observed spectrum, whereas at higher wavelengths, roughly between 5000 \AA and 6000 \AA , it is too high. Nevertheless, the main spectral features are reproduced. The Si II lines at rest wavelengths of 6347 \AA and 6371 \AA (cf. Section 1.2) show up as the blue-shifted part of a P Cygni profile at about 6000 \AA to 6100 \AA . The blueshift of the absorption depends on the velocity of silicon in the explosion ejecta; higher blueshifts correspond to higher silicon velocities. The spectra show that the Si velocity is highest for the c50_ddt2_ddo8 model with the largest kinetic

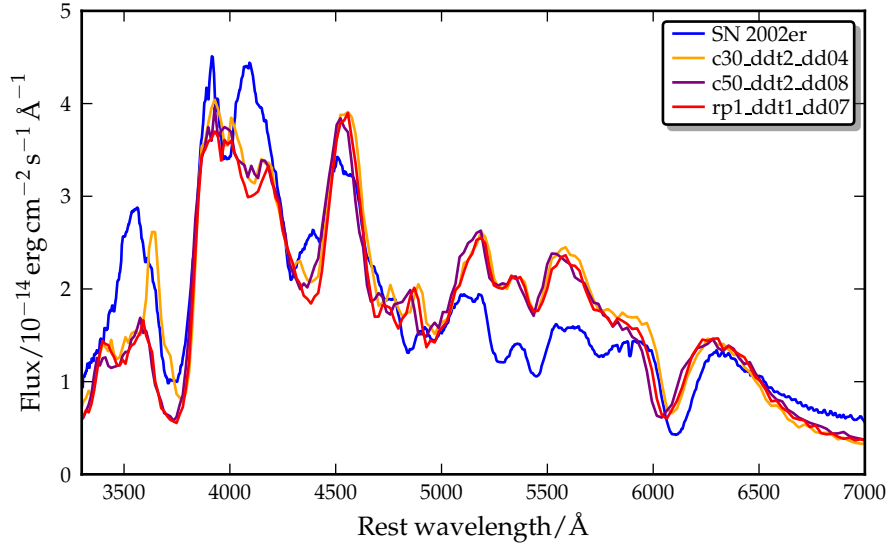


Figure 4.22 | Synthetic spectra for 2D models. Synthetic spectra at B band maximum of the three models from Figures 4.13 and 4.19 are compared to the spectrum of the normal SN Ia 2002er, which was taken from Kotak et al. (2005). I am grateful to S. Hachinger for providing the de-redshifted and de-reddened spectrum and to M. Kromer for providing the synthetic spectra.

energy, less for the `rp1_ddt1_dd07` model and least for the `c30_ddt2_dd04` model with the smallest kinetic energy. This clearly shows a trend among the models; the Si line of the `c30` model is near at the position of the observed line. When comparing the models to the observed SN 2002er, one has to take into account that SN 2002er produced only $0.69 M_{\odot}$ of ^{56}Ni , which is less than the models produced. Hence, the kinetic energy of the ejecta of SN 2002er could be less than in the models presented here.

Although the light curves are too red, the 2D delayed detonation models reproduce the main spectral features. Moreover, a lower initial carbon mass fraction can result in Si material at lower velocities, thus matching better the observed Si line velocity.

4.3 3D Simulations

As especially the turbulent deflagration phase is intrinsically three-dimensional, 3D simulations are necessary for a more realistic description of thermonuclear explosions. As these simulations are computationally demanding, only 5 three-dimensional simulations have been conducted. These include two simulations with progenitors having a homogeneous initial composition of $X(^{12}\text{C}) = 0.3$ and 0.5 , respectively. The other simulations are computed for a progenitor with a varying carbon mass fraction for different ignition conditions and DDT criteria. The final nucleosynthetic yields from the postprocessing calculations are given in Table 4.4.

4.3.1 Initial Models

Similar to the 2D models, the 3D models are determined by three components:

1. The first component is identical to the 2D simulations and denotes the same initial progenitor systems as for the 2D simulations.
2. The DDT criterion as the second component is different in three dimensions (Section 3.1.3) compared to two dimensions. Shortly summarized, all cells at the front lying in a certain density and fuel content range are used to calculate an effective surface of the front. If the ratio of this value to the total flame front surface exceeds a certain threshold for half an eddy turnover time, a detonation is initiated in the cells with the highest velocity fluctuations. For the DDT, the same parameters as in Seitzzahl et al. (2012) are used, except for the fuel content range, which is taken to be 0.3 to 0.7, and the density range, which is tabulated in Table 4.5.
3. The last part corresponds to the initial ignition configuration of the deflagration, which determines the strength of the deflagration phase. The same initial configurations are chosen as in Seitzzahl et al. (2012). The number in the last part of the name denotes the number of ignition kernels.

All 3D simulations have been carried out as full star simulations on a grid with 512^3 cells. This corresponds to an initial resolution of 2.14 km in the inner part of the hybrid moving grid. Approximately one million tracer particles are distributed according to the variable tracer mass method (Section 3.1.3). As for the two-dimensional simulations, the initial composition for the postprocessing was chosen to include the solar metallicity by Asplund et al. (2009).

Table 4.4 | Nucleosynthetic yields for 3D simulations. Given are the total nucleosynthetic yields of each model. The model name consists of three parts. The first part describes the progenitor structure, where the cXY denotes a homogeneous composition with a carbon mass fraction of XY% and rp1 denotes the realistic progenitor model one. The second part indicates the DDT criterion employed, as given in Table 4.5. The third part gives the initial ignition configuration (as in Seitzzahl et al., 2012); the number denotes the number of ignition kernels. $E_{\text{kin,a}}$ is the asymptotic kinetic energy of the ejecta, which is the sum of the final nuclear energy, the initial internal energy and the initial gravitational energy (being negative).

Model	$\frac{M(\text{IGE})}{M_{\odot}}$	$\frac{M(^{56}\text{Ni})}{M_{\odot}}$	$\frac{M(\text{IME})}{M_{\odot}}$	$\frac{M(^{16}\text{O})}{10^{-2}M_{\odot}}$	$\frac{M(^{12}\text{C})}{10^{-3}M_{\odot}}$	$\frac{E_{\text{kin,a}}}{10^{51} \text{ erg}}$
c30_ddt1_No100	0.909	0.675	0.407	7.80	2.29	1.30
c50_ddt1_No100	1.03	0.812	0.327	3.47	0.943	1.55
rp1_ddt1_I0040	0.897	0.681	0.418	7.93	2.94	1.34
rp1_ddt4_I0200	0.939	0.676	0.413	4.56	1.31	1.39
rp1_ddt6_No100	0.944	0.710	0.403	5.03	1.30	1.38

Table 4.5 | DDT criteria used in the 3D simulations. For each DDT criterion, the minimum and maximum densities ρ_{\min} and ρ_{\max} are given.

Criterion	$\rho_{\min}/10^7 \text{ gcm}^{-3}$	$\rho_{\max}/10^7 \text{ gcm}^{-3}$
ddt1	0.5	0.8
ddt4	0.8	1.1
ddt6	0.7	1.0

4.3.2 Hydrodynamical Evolution

The hydrodynamical evolution of three-dimensional models is similar to two-dimensional models. First, a deflagration flame propagates subsonically outwards until a detonation is initiated. Because of the intrinsic, three-dimensional nature of the turbulent burning, three-dimensional models are better suited for this problem. Moreover, in our supernova code `LEAFS`, the subgrid scale model and the DDT criterion are more elaborate for three-dimensional simulations (Section 3.1.3).

The hydrodynamical evolution of three 3D models is visualized in Figure 4.23. Each column shows the evolution for one model at $t = 0.55 \text{ s}$ (first row), t_{DDT} (second row) and $t = 1.50 \text{ s}$ (last row). Each plot displays the mean atomic number, where red regions correspond to IGE, green and yellow regions to IME and blue regions to unburnt material. Panel C shows an early state for the `rp1_ddt6_No100` model and the transition from the inner convective core with a carbon mass fraction of 0.32 to the outer accreted layer with a carbon mass fraction of 0.5 is clearly visible. The second row shows the highly convoluted flame structure of the deflagration front at the time when the first detonation is initiated. The last row shows the structure of each model after the detonation consumed most of the unburnt fuel. The detonation ashes—consisting in the outer parts of IME—encompass the deflagration ashes in large regions.

The evolution of the three models is rather similar; this can be attributed to the fact that all three models employ the same ignition configuration. Despite this, the `c50` model shows a remarkable asymmetry after the deflagration phase (panel E) and also after the detonation phase (panel H).

Global properties of all five models are analyzed in Figure 4.24. The evolution of the total energy shows a similar behaviour as in the two-dimensional models, although the rise after the DDT is not as steep. Furthermore, the time of the first DDT generally is later than in the 2D simulations. This is due to the three-dimensional modelling: in the axisymmetric 2D simulations, in principle tori are burned with a much larger volume than the three-dimensional ignition kernels have. Therefore, the evolution of the deflagration is faster in two dimensions than in three dimensions. One can also note that all models have final total energies above 10^{51} erg and are thus completely unbound. Panel B shows the temporal evolution of the turbulent energy from the subgrid scale model. One can see that for more ignition kernels (`Io200` model), the deflagration phase is stronger. The nuclear energy generation rate is shown in panel C. Similar to the 2D simulations, the nuclear energy generation peaks shortly after the detonation is initiated. For earlier DDT times, the spike in the rate is higher, which is caused by the detonation

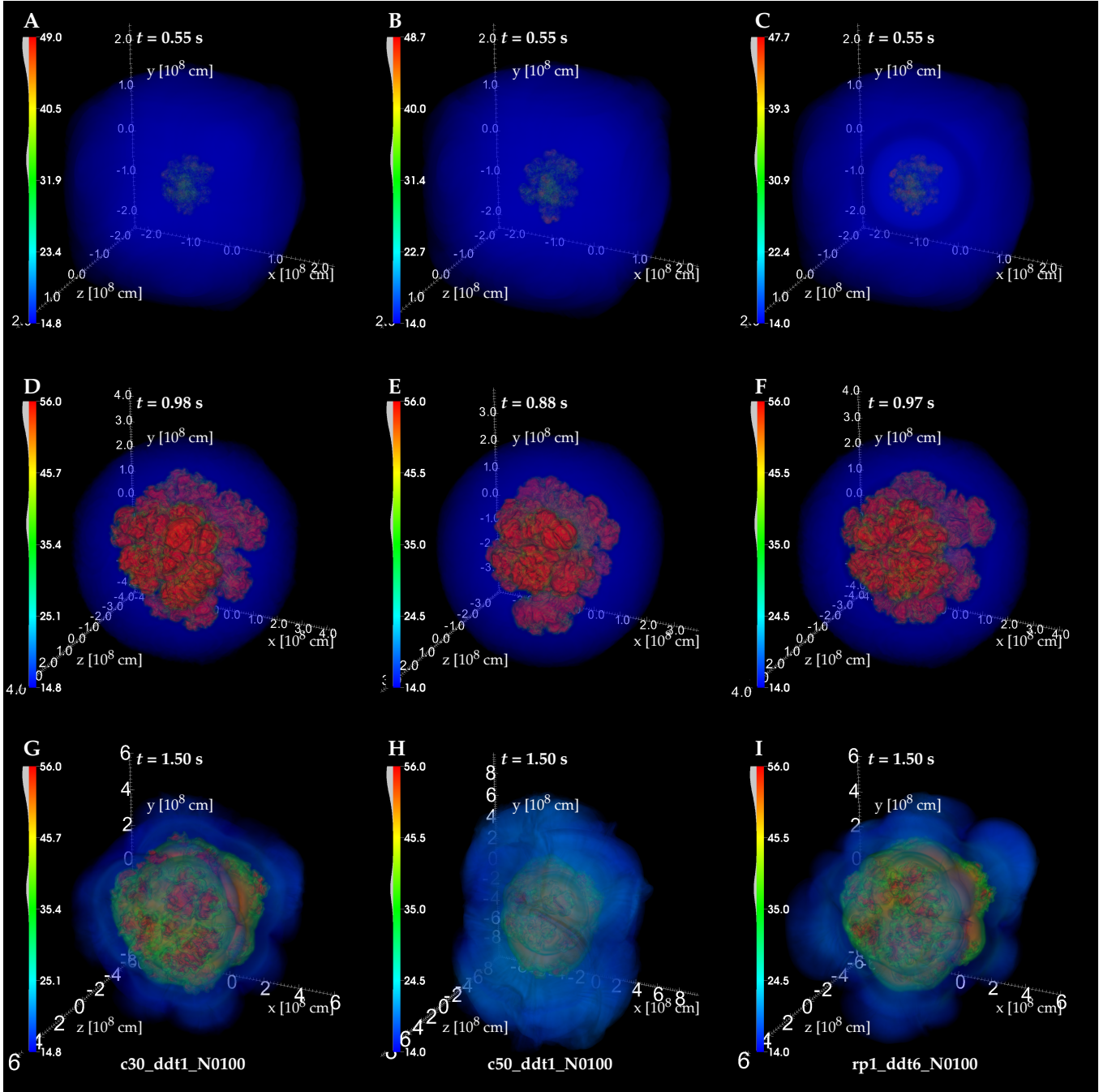


Figure 4.23 | Hydrodynamical evolution of three 3D models. Each plot shows a volume rendering of the mean atomic number \bar{A} of a certain snapshot of the corresponding hydrodynamical simulation. The axes indicate the spatial coordinates in 10^8 cm. The blue regions indicate carbon and oxygen, the green and yellow regions intermediate mass elements and the red region iron group elements. The leftmost column (A, D, G) shows the model c30_ddt1_N0100, the central column (B, E, H) shows the model c50_ddt1_N0100 and the rightmost column (C, F, I) shows the model rp1_ddt6_N0100. The time is printed for each snapshot. The second row (D, E, F) shows the abundance structure at the time of the first DDT for each model.

4 Results

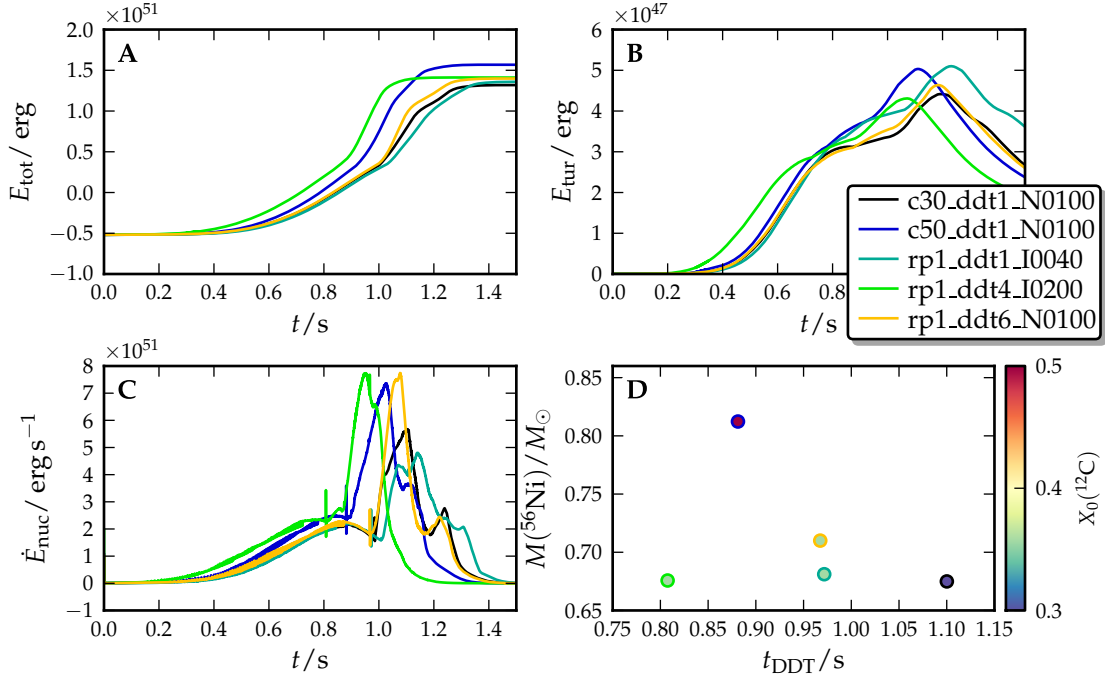


Figure 4.24 | Global properties of 3D simulations. In the first three panels, global properties are plotted against the simulation time for all 3D models (compare Table 4.4). Panel A displays the total energy, panel B the turbulent energy and panel C the nuclear energy generation rate. Panel D shows the total ^{56}Ni mass against the time of the first DDT for all models. The models are colored by their initial averaged carbon mass fraction and the edge color indicates the model with the same colors as used in A–C.

consuming higher density fuel as at later times and thus having a greater energy release. Panel D displays the total ^{56}Ni mass over the DDT time. A similar trend as in the 2D models can be seen: for similar initial conditions, a model with lower carbon mass fraction undergoes the DDT later, thus producing a smaller amount of ^{56}Ni .

A comparison of the rp1_ddt1_I0040 model with the rp1_ddt4_I0200 model shows that a model with more ignition kernels and thus a stronger deflagration phase can produce the same amount of ^{56}Ni as a model with a weaker deflagration phase, if the DDT is initiated earlier in a higher density range.

4.3.3 Nucleosynthetic Yields

The detailed nucleosynthetic abundances for all five models are summarized in Table 4.4. As in the 2D simulations, models with lower carbon mass fractions tend to produce less ^{56}Ni for the same initial conditions. For similar ^{56}Ni mass, on the other hand, lower kinetic energies are reached. Moreover, the models with lower carbon mass fraction in the core produce more IME and have also more unburnt material (C, O).

For the same three models as in Figure 4.23, the nucleosynthetic abundances are compared to the solar abundances (Asplund et al., 2009) in Figure 4.25. The mass

fraction of each isotope was computed by following the radioactive decays for 2 Gyr. All mass fractions have been normalized to the mass fraction of ^{56}Fe , which is the main stable decay product of ^{56}Ni . The most abundant isotopes are the iron group nuclei, especially Cr, Fe and Ni. The three models mainly differ in the abundances of intermediate mass elements from Mg to Ti. The models with a lower carbon mass fraction in the core (c30 and rp1) produce more IME compared to ^{56}Fe than the c50 model. For most isotopes, this is even more pronounced in the c30 model (upward triangles). Similarly to the 2D simulations, the abundances of the α isotopes from ^{28}Si to ^{40}Ca are higher than half the solar values for the c30 and rp1 models and slightly below for the c50 model.

The details of the nucleosynthetic yields for the iron group nuclei are shown in Figure 4.26. In general, most isotopes lie in a range of over- or underproduction of solar abundances by a factor of two, except for the most neutron-rich isotopes. The c50 model (circles) shows smaller abundances of most Cr isotopes, but higher abundances of some Ni isotopes. The other two models have similar abundances (triangles). Compared to the abundances of the W7 model (squares), less Ni and Co isotopes are produced, but some Cr and Mn abundances are higher. ^{58}Ni is only overproduced by a factor of two, compared to a factor of four in the W7 model. As explained for the 2D simulations, this can explain the iron abundance in the solar system through galactic chemical evolution.

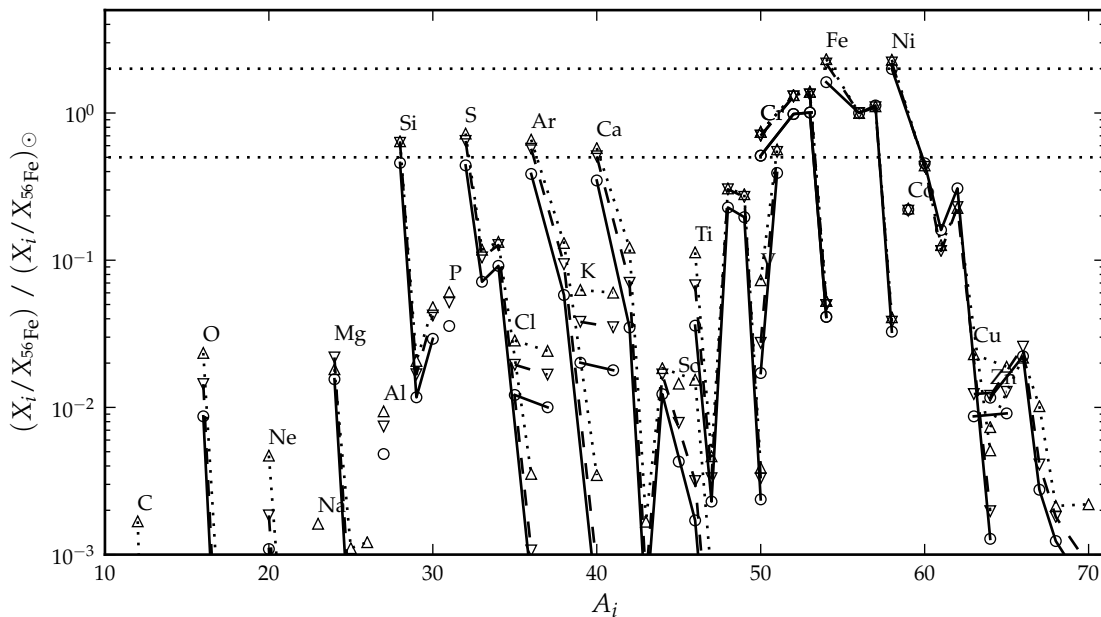


Figure 4.25 | Comparison of nucleosynthetic yields to solar composition for 3D models. The mass fractions of all isotopes normalized to ^{56}Fe are compared to the solar abundances from Asplund et al. (2009) and plotted against the mass number. Shown are the models c30_ddt1_No100 (upward triangles/dotted lines), c50_ddt1_No100 (circles/solid lines) and rp1_ddt6_No100 (downward triangles/dashed lines). The horizontal dotted lines indicate over- and underproduction by a factor of two compared to the solar values.

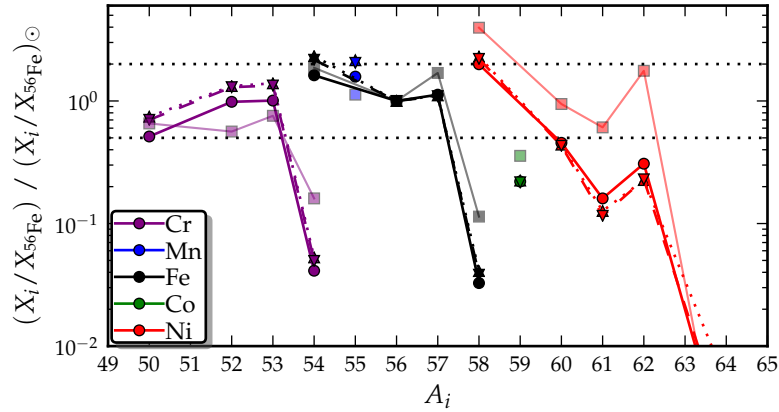


Figure 4.26 | Comparison of iron group nuclei to solar composition for 3D models. The mass fractions of iron group nuclei normalized to ^{56}Fe are compared to the solar abundances from Asplund et al. (2009) and plotted against the mass number. Shown are the models c30_ddt1_No100 (upward triangles/dotted lines), c50_ddt1_No100 (circles/solid lines) and rp1_ddt6_No100 (downward triangles/dashed lines), as well as the W7 model (transparent squares/thin solid lines, Maeda et al., 2010). The horizontal dotted lines indicate over- and underproduction by a factor of two compared to the solar values.

4.3.4 Distribution of Ejecta in Velocity Space

For the three-dimensional models, no synthetic spectra were computed, as the radiative transfer calculations are computationally very demanding in three dimensions. This is because of the high number of photon packets which are necessary to obtain high quality synthetic spectra. Due to time restrictions, these calculations could not be done in the course of this diploma thesis, but will be engaged in the future.

Nevertheless, one can compare the structure of the ejecta in velocity space, which determines the synthetic light curves and spectra. The results of mapping the detailed nucleosynthetic yields and the density profile from the hydrodynamical simulation are presented in Figure 4.27 (c30_ddt1_No100), Figure 4.28 (c50_ddt1_No100), Figure 4.29 (rp1_ddt6_No100), Figure 4.31 (rp1_ddt4_I0200) and Figure 4.30 (rp1_ddt1_I0040). The plots show the density and mass fractions in the v_x - v_z -plane for $v_y = 0$. Although these plots do not capture the full information of the three-dimensional models, they are better suitable for a detailed analysis than 3D plots of volume rendered quantities (e.g. Figure 4.23), where the scales cannot be analyzed as well as in two-dimensional plots.

All models show a similar global structure: an inner core consisting of stable iron elements and ^{56}Ni is surrounded by layers of intermediate mass elements (Si is shown as an example), oxygen and carbon. Apart from this global structure, all models show characteristic features and also asymmetries in varying degrees. The density and the C, O and Si abundances in the outer layers show irregularities in the circular structure which can be attributed to merging detonation wavefronts. The higher densities in these regions result from the hydrodynamical shocks propagating through the ashes of the other detonation wave. A good example for this process is demonstrated in Figure 4.27, where near the $v_z = 0$ -plane, two big depressions in the circular structure are visible in

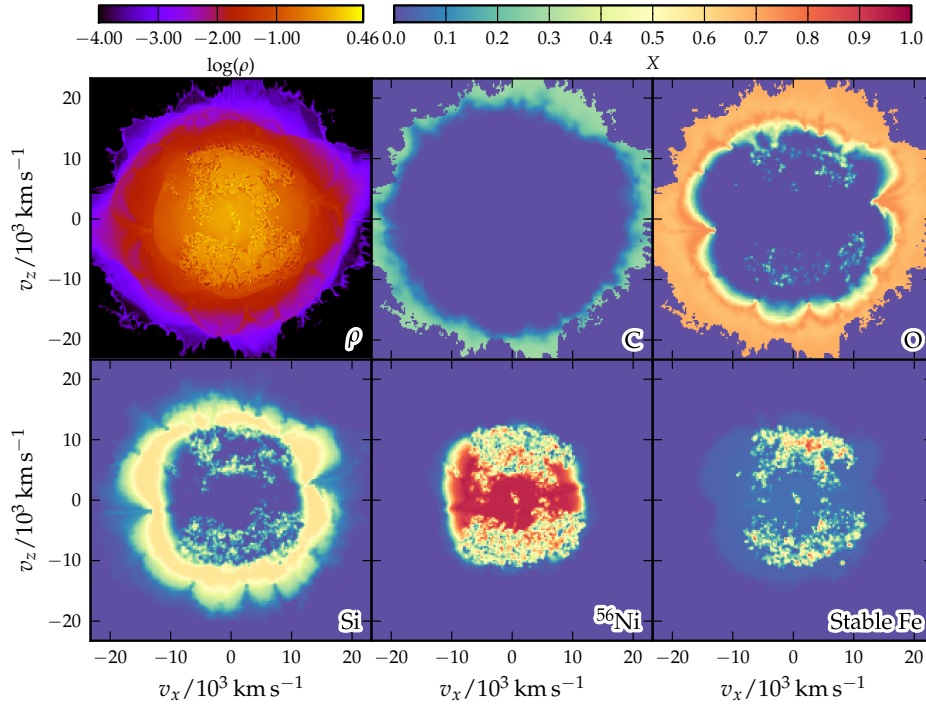


Figure 4.27 | Ejecta morphology in velocity space for c30_ddt1_No100. Shown are slices in the v_x - v_z -plane ($v_y = 0$) for the density from the hydrodynamical simulation (top left panel) and the nucleosynthetic yields from the postprocessing step, which were mapped to a grid with 200^3 cells at the end of the simulation ($t = 100$ s). The mass fractions of C, O and Si are sums over all corresponding isotopes. The last panel shows the mass fraction of “stable Fe”, which was computed as the mass fraction of all IGE minus the mass fractions of the radioactive isotopes ^{56}Ni , ^{56}Co , ^{52}Fe and ^{48}Cr . In the outer regions, where the density is below 10^{-4} g/cm 3 , all abundance values have been set to zero. For this model, $M(^{56}\text{Ni}) = 0.675 M_{\odot}$.

the Si and O mass fractions. The same structures can also be seen in the density plot and show higher densities.

As the c30 model is the only model with a carbon mass fraction of 0.3 also in the outer layers, it shows unburnt oxygen at a mass fraction of 0.7, as opposed to the other models which show unburnt oxygen at a mass fraction of 0.5. The first three models, c30_ddt1_No100 (Figure 4.27), c50_ddt1_No100 (Figure 4.28) and rp1_ddt6_No100 (Figure 4.29), are all ignited with the same initial configuration. This leads to similar features resulting from the deflagration: the distribution of stable iron—mainly resulting from the deflagration phase at high densities—shows an asymmetry comparing v_x - and v_z -directions. The deflagration burns only in the upper and lower hemisphere, at least in this plane. As can be seen in the ^{56}Ni mass fractions, the core area consists mainly of ^{56}Ni resulting from the detonation wave consuming the unburnt material in the core. A similar feature can be seen for the model rp1_ddt1_I0040 (Figure 4.30), where the deflagration ashes are concentrated in an outer shell concentrated in the upper hemisphere. A core of ^{56}Ni resulting from the detonation is found in the center, slightly shifted to the lower hemisphere. The model rp1_ddt4_I0200 with more ignition sparks shows a

4 Results

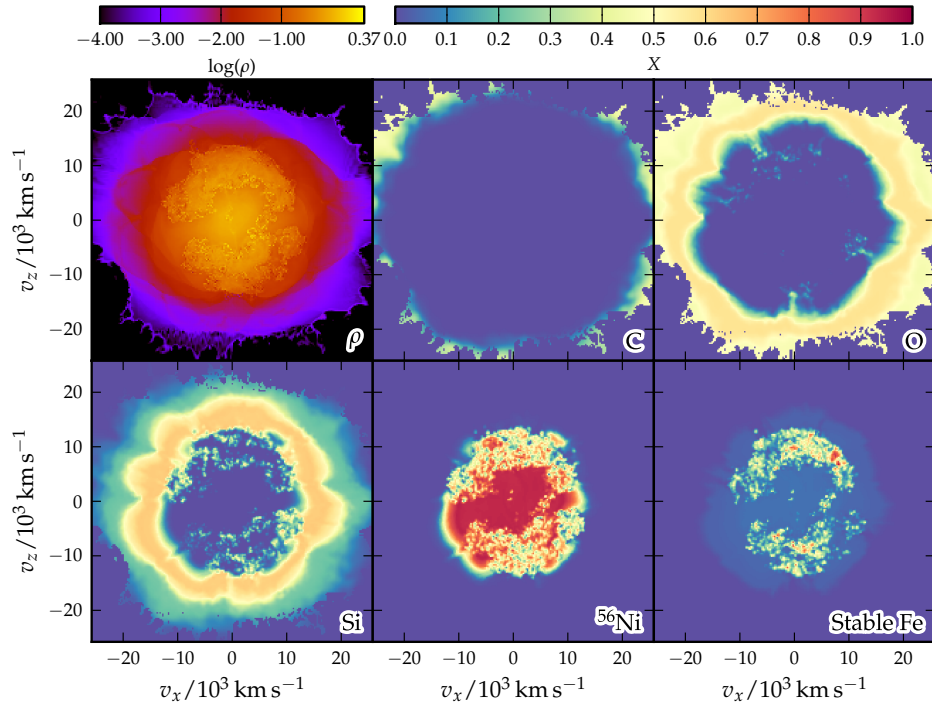


Figure 4.28 | Ejecta morphology in velocity space for `c50_ddt1_N0100`. For a description of the plots, see Figure 4.27. For this model, $M(^{56}Ni) = 0.812 M_{\odot}$.

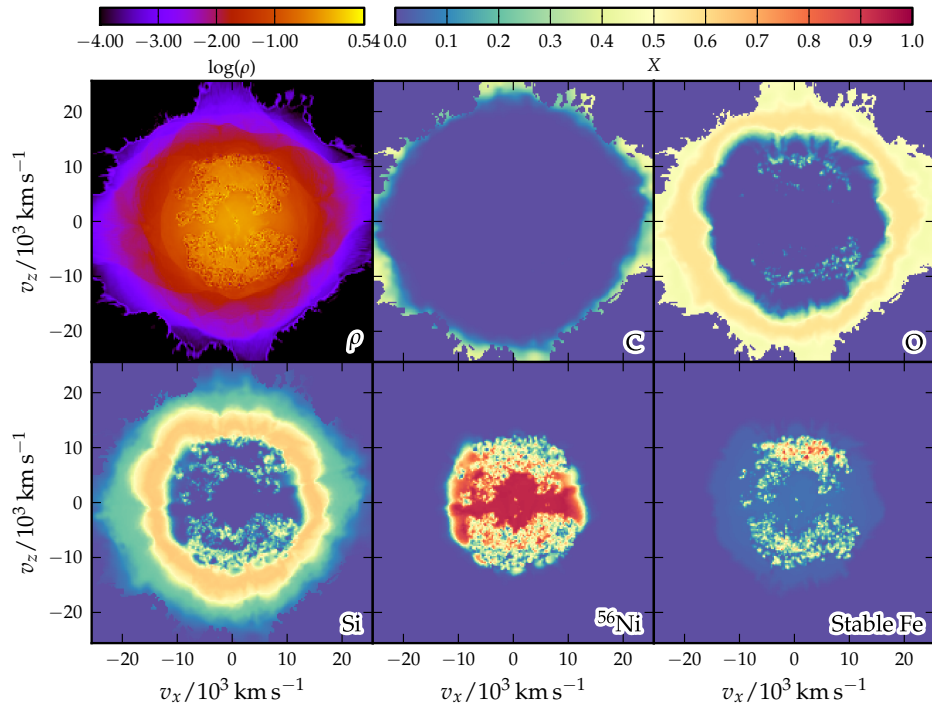


Figure 4.29 | Ejecta morphology in velocity space for `rp1_ddt6_N0100`. For a description of the plots, see Figure 4.27. For this model, $M(^{56}Ni) = 0.681 M_{\odot}$.

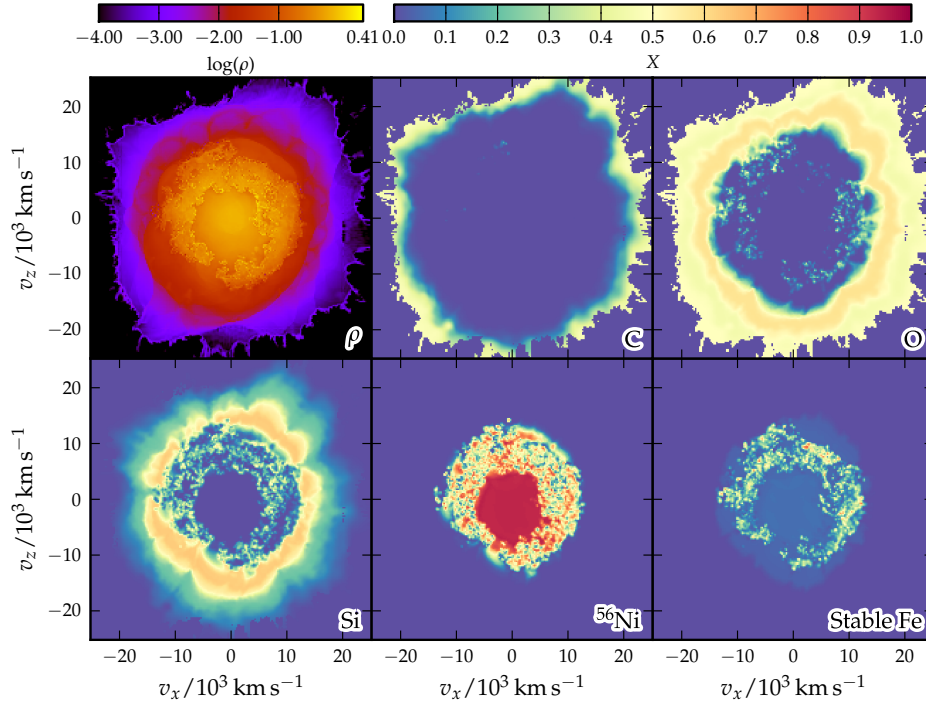


Figure 4.30 | Ejecta morphology in velocity space for `rp1_ddt1_I0040`. For a description of the plots, see Figure 4.27. For this model, $M(^{56}Ni) = 0.676 M_{\odot}$.

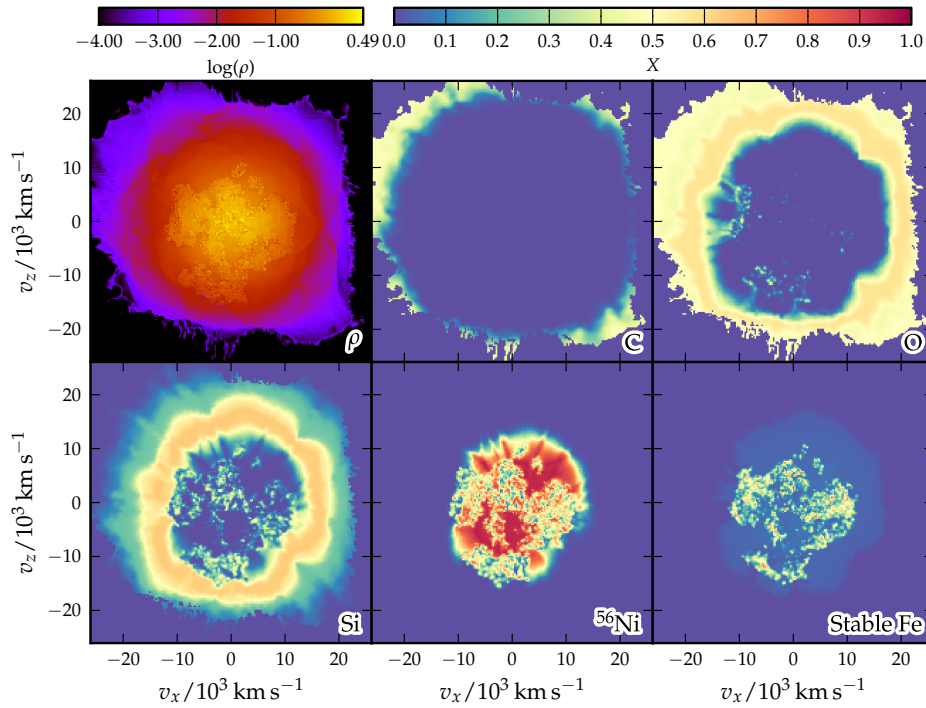


Figure 4.31 | Ejecta morphology in velocity space for `rp1_ddt4_I0200`. For a description of the plots, see Figure 4.27. For this model, $M(^{56}Ni) = 0.710 M_{\odot}$.

stronger deflagration phase. This leads to a more complete deflagration burning near the center (Figure 4.31), producing more stable IGE in the core. The whole core is also more mixed in this model compared to the other models.

Comparing the velocities of the ^{56}Ni core, the c50 model shows the highest velocities up to $\sim 15\,000$ km/s, whereas the other models show lower velocities up to $\sim 12\,000$ km/s or $\sim 13\,000$ km/s. These velocities are somewhat smaller than in the 2D models compared in Figure 4.19, although one has to take into account the different nickel mass of the models. This may also have an impact on the light curves, which are too red in the 2D models (Figure 4.21) because of iron group elements being present at comparatively high velocities. As these velocities are lower in the 3D models, the light curves may be not as red, but this has to be confirmed in radiative transfer calculations.

The Si material shows up at the lowest velocities for the c30 model and at the highest velocities for the c50 model. The rp1 models lie in between these two extremes, but show also small abundances of Si at higher velocities, similar to the c50 model. This should lead to a similar effect in the spectra as for the 2D models (Figure 4.22): the Si II feature should shift to lower velocities and thus higher wavelengths, which is required by observations. Radiative transfer calculations will be necessary in order to be able to finally compare the synthetic spectra to observed spectra and see the effect on the Si II feature.

5 Conclusions

In this diploma thesis, I examined the impact of the progenitor white dwarf's composition on thermonuclear supernovae. To this end, the modelling of burning fronts was improved to account for different chemical compositions. This improved modelling was then applied to large scale, two- and three-dimensional simulations of thermonuclear explosions of Chandrasekhar-mass WDs in the delayed detonation model.

Varying progenitor compositions were taken into account since stellar evolution results predict a WD with a carbon depleted core (Section 2.4). Opposed to current simulations using the same code (e.g. Seitenzahl et al., 2012), which assume homogeneous progenitors, this work presents a more realistic treatment of the initial composition.

Apart from implementing a more realistic treatment of the progenitor composition and examining its effect on the explosion process, the objectives of this diploma thesis are on the one hand to compare the outcome of the simulations with observables—light curves and spectra—in order to see if the improved modelling also leads to a better agreement with the process in Nature. On the other hand, it is important to check if the variability predicted in the stellar evolution models for the initial composition leads to a variability in the outcome, thus helping to understand the diversity of Type Ia supernovae.

5.1 Properties of Burning Fronts

The burning fronts—deflagrations and detonations—are modeled in our numerical scheme using the level set method as a discontinuity given by the zero level set of a signed distance function. The nuclear energy is released directly behind the front and is taken from tables. These tables were created for different chemical compositions of the WD using an iterative calibration scheme (Section 4.1) in order to be able to model burning fronts for different—also varying—chemical compositions.

The initial carbon mass fraction of the fuel affects the total energy release mainly in two ways:

- Due to different binding energies, the total energy release of burning to NSE is lower for lower carbon mass fractions. The iterative calibration leads to an overall lower energy release at all densities.
- The transitions to the different burning stages (carbon burning, oxygen burning, silicon burning) shift to higher densities for lower carbon mass fractions.

Thus, the explosion strength of deflagrations and detonations is reduced for lower carbon mass fractions.

5.2 Impact on Simulations of Delayed Detonations

These new tables have been used to examine the impact of different initial compositions—homogeneous and varying—on thermonuclear explosion models in two (Section 4.2) and three dimensions (Section 4.3). The main global impact of the chemical composition is that lower initial carbon mass fractions lead to a lower mass of produced ^{56}Ni for the same ignition conditions. Moreover, the asymptotic kinetic energy is reduced. The reason for this lies in the lower energy release of the burning fronts. The deflagration develops weaker for lower carbon mass fractions, hence leading to a later deflagration-to-detonation transition. At later times, the pre-expansion of the WD by the deflagration is stronger, thus the densities are lower. Therefore, the detonation produces less ^{56}Ni at these lower densities.

This connection of the initial composition to the total ^{56}Ni mass showed that a variety of models with different ^{56}Ni masses are obtained for different initial compositions. Thus, some part of the diversity of SNe Ia in luminosity may be explained by variations in the initial composition.

The total nucleosynthetic yields of the models after the decay of most radioactive isotopes may be able to explain the solar abundances pattern relative to ^{56}Fe . The difference in the abundance patterns between different progenitor compositions is not very pronounced. Here, the impact of metallicity was found to be stronger.

The light curves and spectra of thermonuclear explosions are determined by the morphology of the ejecta in velocity space. The delayed detonation models show a layered structure with a core consisting mainly of ^{56}Ni and stable iron group elements and with shells of intermediate mass elements—most prominently silicon—, of oxygen and of carbon on top of this core. The maximum velocities of the ^{56}Ni and IGE core lie in a range of 12 000 km/s to 17 000 km/s and are higher for initial models with higher carbon mass fractions. Furthermore, the 3D simulations suggest somewhat lower velocities than the 2D simulations. The structure of Si in the ejecta determines the characteristic Si II absorption feature and depends on the initial composition. Homogeneous models with $X_0(^{12}\text{C}) = 0.3$ show lower velocities than homogeneous models with $X_0(^{12}\text{C}) = 0.5$, where also some Si is present out to high velocities. More realistic progenitor models featuring a carbon depleted core with $X_0(^{12}\text{C}) = 0.32$ and an outer accretion shell with $X_0(^{12}\text{C}) = 0.5$ show an intermediate behaviour. The velocity of the region with the maximum abundances lies in between the two homogeneous models, but some Si is also present up to high velocities.

For three two-dimensional models, radiative transfer calculations yield synthetic light curves and spectra, which are compared to observed light curves and spectra. The absolute magnitudes in the B band and the rise times compare well to observations. The light curves show agreement around maximum light in the B band, but are too bright in the redder bands, especially in the V band. This might be due to ^{56}Ni and other iron group elements being present up to rather high velocities, thus distributing the flux from the blue part of the spectrum to the redder parts. The spectra of these three models are compared to the normal supernova 2002er. They reproduce the main features of the spectrum, although they are too red. For lower initial carbon mass fraction, the

Si II absorption feature shifts to lower velocities and thus to higher wavelengths. This matches better to the observed spectrum.

Thus, it has been shown that a more realistic modelling of the initial chemical composition leads to models which compare better to an observed supernova than the generic progenitor setups used in multidimensional SN Ia simulations before.

5.3 Outlook

In order to examine the impact of the initial composition on synthetic observables in more detail, more three-dimensional models have to be computed accompanied by radiative transfer calculations. These 3D models will allow for a more realistic treatment of the hydrodynamics and the radiative transfer.

The properties of the burning fronts depending on the initial composition can also be used for studying the impact of the initial composition on other explosion scenarios, such as the sub-Chandrasekhar-mass double detonation models or the violent merger models.

As the nucleosynthetic yields depend strongly on the initial metallicity of the progenitor, the impact of metallicity on the realistic progenitor models presented in this work should be examined in more detail. This will also help to improve modeling of the chemical evolution of galaxies.

A Nucleosynthetic Yields for 2D Simulations

Table A.1 | Nucleosynthetic yields for 2D simulations. Given are the total nucleosynthetic yields of each model. The model name consists of three parts. The first part describes the progenitor structure, where the cXY denotes a homogeneous composition with a carbon mass fraction of XY%, rp1 and rp2 denote the realistic progenitor models one and two (see also Section 4.2.1). The second part indicates the DDT criterion employed, as given in Table 4.1. The third part gives the initial ignition configuration (cf. Table 4.2). $E_{\text{kin,a}}$ is the asymptotic kinetic energy of the ejecta, which is the sum of the final nuclear energy, the initial internal energy and the initial gravitational energy (being negative). The last lines show the yields for the models with scaled initial metallicity in the postprocessing (cf. Section 4.2.3).

Model	$\frac{M(\text{IGE})}{M_{\odot}}$	$\frac{M(^{56}\text{Ni})}{M_{\odot}}$	$\frac{M(\text{IME})}{M_{\odot}}$	$\frac{M(^{16}\text{O})}{10^{-1}M_{\odot}}$	$\frac{M(^{12}\text{C})}{10^{-3}M_{\odot}}$	$\frac{E_{\text{kin,a}}}{10^{51} \text{ erg}}$
c20_ddt1_ddo3	0.704	0.462	0.537	1.46	4.87	1.09
c20_ddt1_ddo4	1.05	0.811	0.282	0.614	1.87	1.28
c20_ddt1_ddo5	1.22	0.971	0.142	0.351	0.980	1.35
c20_ddt1_ddo6	1.15	0.973	0.198	0.445	1.16	1.32
c20_ddt1_ddo7	0.869	0.603	0.418	1.02	3.90	1.18
c20_ddt1_ddo8	0.850	0.597	0.441	0.982	3.83	1.18
c20_ddt1_ddo9	0.708	0.444	0.544	1.36	5.02	1.11
c20_ddt1_dd10	0.879	0.609	0.417	0.951	3.14	1.19
c30_ddt1_ddo3	0.828	0.579	0.483	0.848	2.04	1.26
c30_ddt1_ddo4	1.09	0.848	0.264	0.446	0.988	1.38
c30_ddt1_ddo5	1.23	0.984	0.143	0.255	0.560	1.45
c30_ddt1_ddo6	1.19	1.01	0.179	0.288	0.446	1.42
c30_ddt1_ddo7	0.945	0.677	0.378	0.716	2.18	1.31
c30_ddt1_ddo8	0.881	0.626	0.439	0.752	2.23	1.29
c30_ddt1_ddo9	0.850	0.580	0.462	0.829	2.22	1.28
c30_ddt1_dd10	0.943	0.672	0.388	0.643	1.68	1.32
c40_ddt1_ddo3	1.02	0.769	0.332	0.428	1.04	1.44
c40_ddt1_ddo4	1.15	0.912	0.214	0.290	0.632	1.50
c40_ddt1_ddo5	1.26	1.02	0.115	0.188	0.494	1.54
c40_ddt1_ddo6	1.23	1.05	0.145	0.192	0.308	1.53
c40_ddt1_ddo7	1.11	0.836	0.248	0.427	1.22	1.47
c40_ddt1_ddo8	1.10	0.844	0.254	0.397	1.19	1.47
c40_ddt1_ddo9	1.00	0.729	0.345	0.510	1.57	1.43
c40_ddt1_dd10	1.08	0.803	0.279	0.400	1.03	1.46
c50_ddt1_ddo3	1.08	0.829	0.282	0.327	1.05	1.55
c50_ddt1_ddo4	1.21	0.968	0.166	0.198	0.470	1.60
c50_ddt1_ddo5	1.29	1.04	0.0951	0.134	0.378	1.63
c50_ddt1_ddo6	1.26	1.08	0.122	0.126	0.270	1.62
c50_ddt1_ddo7	1.14	0.869	0.224	0.336	1.11	1.57
c50_ddt1_ddo8	1.15	0.888	0.222	0.295	0.983	1.57
c50_ddt1_ddo9	1.11	0.837	0.254	0.331	0.995	1.56

Table A.1 | *Continued.*

Model	$\frac{M(\text{IGE})}{M_{\odot}}$	$\frac{M(^{56}\text{Ni})}{M_{\odot}}$	$\frac{M(\text{IME})}{M_{\odot}}$	$\frac{M(^{16}\text{O})}{10^{-1}M_{\odot}}$	$\frac{M(^{12}\text{C})}{10^{-3}M_{\odot}}$	$\frac{E_{\text{kin,a}}}{10^{51} \text{ erg}}$
c50_ddt1_dd10	1.16	0.883	0.213	0.269	0.834	1.58
c20_ddt2_dd03	0.575	0.345	0.552	2.45	12.3	0.973
c20_ddt2_dd04	0.954	0.719	0.334	1.02	4.27	1.21
c20_ddt2_dd05	1.15	0.905	0.195	0.486	1.90	1.32
c20_ddt2_dd06	1.09	0.916	0.225	0.761	2.64	1.26
c20_ddt2_dd07	0.700	0.442	0.518	1.64	8.38	1.08
c20_ddt2_dd08	0.662	0.420	0.543	1.76	8.98	1.07
c20_ddt2_dd09	0.571	0.319	0.590	2.16	10.5	1.01
c20_ddt2_dd10	0.721	0.458	0.508	1.56	6.82	1.10
c30_ddt2_dd03	0.646	0.409	0.600	1.44	4.23	1.17
c30_ddt2_dd04	0.984	0.748	0.340	0.704	2.13	1.33
c30_ddt2_dd05	1.16	0.921	0.193	0.387	1.03	1.42
c30_ddt2_dd06	1.11	0.930	0.238	0.522	1.13	1.37
c30_ddt2_dd07	0.725	0.467	0.534	1.29	5.28	1.20
c30_ddt2_dd08	0.687	0.442	0.579	1.24	4.66	1.20
c30_ddt2_dd09	0.660	0.402	0.595	1.34	5.22	1.19
c30_ddt2_dd10	0.756	0.493	0.526	1.10	3.66	1.23
c40_ddt2_dd03	0.803	0.559	0.515	0.780	2.46	1.35
c40_ddt2_dd04	1.04	0.805	0.308	0.454	1.31	1.45
c40_ddt2_dd05	1.21	0.963	0.162	0.266	0.847	1.52
c40_ddt2_dd06	1.16	0.976	0.210	0.313	0.666	1.49
c40_ddt2_dd07	0.931	0.666	0.398	0.653	2.58	1.40
c40_ddt2_dd08	0.918	0.664	0.419	0.585	2.13	1.40
c40_ddt2_dd09	0.761	0.498	0.549	0.847	2.84	1.34
c40_ddt2_dd10	0.899	0.629	0.434	0.630	2.03	1.38
c50_ddt2_dd03	0.862	0.616	0.478	0.559	2.00	1.46
c50_ddt2_dd04	1.09	0.851	0.276	0.302	0.886	1.56
c50_ddt2_dd05	1.23	0.990	0.143	0.193	0.688	1.61
c50_ddt2_dd06	1.18	0.998	0.196	0.223	0.571	1.58
c50_ddt2_dd07	0.969	0.702	0.377	0.500	2.09	1.50
c50_ddt2_dd08	0.977	0.725	0.378	0.414	1.62	1.51
c50_ddt2_dd09	0.884	0.616	0.462	0.508	2.01	1.48
c50_ddt2_dd10	1.01	0.742	0.345	0.391	1.40	1.52
rp1_ddt1_dd03	0.864	0.614	0.479	0.536	1.77	1.34
rp1_ddt1_dd04	1.12	0.880	0.249	0.275	0.867	1.46
rp1_ddt1_dd05	1.29	1.04	0.0983	0.138	0.365	1.52
rp1_ddt1_dd06	1.22	1.03	0.161	0.188	0.404	1.49
rp1_ddt1_dd07	1.00	0.734	0.349	0.446	1.84	1.40
rp1_ddt1_dd08	1.01	0.751	0.347	0.406	1.47	1.40
rp1_ddt1_dd09	0.906	0.634	0.441	0.497	1.87	1.37
rp1_ddt1_dd10	0.972	0.700	0.382	0.431	1.44	1.39
rp1_ddt2_dd03	0.661	0.422	0.628	1.05	3.41	1.25
rp1_ddt2_dd04	0.970	0.734	0.372	0.535	1.75	1.39
rp1_ddt2_dd05	1.23	0.987	0.145	0.201	0.653	1.50
rp1_ddt2_dd06	1.13	0.956	0.228	0.351	0.833	1.44
rp1_ddt2_dd07	0.850	0.586	0.478	0.668	2.95	1.34
rp1_ddt2_dd08	0.783	0.533	0.538	0.737	2.75	1.32

Table A.1 | *Continued.*

Model	$\frac{M(\text{IGE})}{M_{\odot}}$	$\frac{M(^{56}\text{Ni})}{M_{\odot}}$	$\frac{M(\text{IME})}{M_{\odot}}$	$\frac{M(^{16}\text{O})}{10^{-1}M_{\odot}}$	$\frac{M(^{12}\text{C})}{10^{-3}M_{\odot}}$	$\frac{E_{\text{kin,a}}}{10^{51} \text{ erg}}$
rp1_ddt2_dd09	0.694	0.434	0.610	0.894	3.83	1.28
rp1_ddt2_dd10	0.785	0.521	0.530	0.794	2.76	1.31
rp1_ddt3_dd03	0.584	0.354	0.643	1.62	5.32	1.17
rp1_ddt3_dd04	0.939	0.704	0.393	0.630	2.24	1.37
rp1_ddt3_dd05	1.22	0.973	0.156	0.229	0.744	1.49
rp1_ddt3_dd06	1.11	0.937	0.237	0.465	1.44	1.43
rp1_ddt3_dd07	0.768	0.509	0.540	0.845	3.86	1.30
rp1_ddt3_dd08	0.648	0.406	0.636	1.08	4.38	1.25
rp1_ddt3_dd09	0.617	0.363	0.654	1.20	5.04	1.23
rp1_ddt3_dd10	0.703	0.445	0.580	1.09	3.94	1.26
rp1_ddt4_dd03	0.584	0.353	0.658	1.48	5.03	1.18
rp1_ddt4_dd04	0.917	0.683	0.408	0.695	2.36	1.36
rp1_ddt4_dd05	1.22	0.976	0.153	0.224	0.752	1.49
rp1_ddt4_dd06	1.10	0.923	0.254	0.430	1.29	1.42
rp1_ddt4_dd07	0.768	0.509	0.540	0.845	4.20	1.30
rp1_ddt4_dd08	0.644	0.403	0.638	1.09	4.46	1.25
rp1_ddt4_dd09	0.617	0.363	0.653	1.20	5.55	1.23
rp1_ddt4_dd10	0.699	0.440	0.582	1.11	4.05	1.25
rp2_ddt1_dd03	0.886	0.556	0.470	0.539	1.56	1.32
rp2_ddt1_dd04	1.15	0.833	0.234	0.245	0.776	1.43
rp2_ddt1_dd05	1.29	0.970	0.101	0.149	0.408	1.48
rp2_ddt1_dd06	1.21	0.984	0.179	0.191	0.497	1.45
rp2_ddt1_dd07	1.00	0.638	0.361	0.472	2.03	1.36
rp2_ddt1_dd08	1.03	0.695	0.338	0.370	1.33	1.38
rp2_ddt1_dd09	0.933	0.575	0.426	0.498	1.69	1.34
rp2_ddt1_dd10	0.979	0.613	0.385	0.450	1.68	1.36
rp2_ddt2_dd03	0.722	0.403	0.572	1.12	3.05	1.22
rp2_ddt2_dd04	1.06	0.745	0.304	0.461	1.48	1.38
rp2_ddt2_dd05	1.24	0.921	0.145	0.213	0.717	1.46
rp2_ddt2_dd06	1.11	0.892	0.251	0.449	1.15	1.39
rp2_ddt2_dd07	0.848	0.494	0.478	0.798	3.36	1.29
rp2_ddt2_dd08	0.857	0.526	0.480	0.701	2.47	1.31
rp2_ddt2_dd09	0.751	0.403	0.561	0.944	3.19	1.26
rp2_ddt2_dd10	0.829	0.471	0.496	0.820	3.00	1.29
rp2_ddt3_dd03	0.655	0.343	0.584	1.62	4.90	1.16
rp2_ddt3_dd04	1.03	0.722	0.313	0.606	2.02	1.36
rp2_ddt3_dd05	1.21	0.892	0.172	0.238	0.949	1.45
rp2_ddt3_dd06	1.08	0.856	0.276	0.560	1.59	1.36
rp2_ddt3_dd07	0.739	0.391	0.544	1.18	5.66	1.22
rp2_ddt3_dd08	0.758	0.432	0.541	1.06	3.89	1.25
rp2_ddt3_dd09	0.726	0.380	0.572	1.07	3.84	1.24
rp2_ddt3_dd10	0.751	0.398	0.541	1.12	4.19	1.24
rp2_ddt4_dd03	0.654	0.343	0.581	1.65	5.00	1.16
rp2_ddt4_dd04	1.03	0.721	0.314	0.604	2.02	1.36
rp2_ddt4_dd05	1.21	0.892	0.172	0.238	0.986	1.45
rp2_ddt4_dd06	1.08	0.856	0.276	0.560	1.59	1.36
rp2_ddt4_dd07	0.739	0.391	0.544	1.18	5.69	1.22
rp2_ddt4_dd08	0.757	0.432	0.541	1.06	3.89	1.25

Table A.1 | *Continued.*

Model	$\frac{M(\text{IGE})}{M_{\odot}}$	$\frac{M(^{56}\text{Ni})}{M_{\odot}}$	$\frac{M(\text{IME})}{M_{\odot}}$	$\frac{M(^{16}\text{O})}{10^{-1}M_{\odot}}$	$\frac{M(^{12}\text{C})}{10^{-3}M_{\odot}}$	$\frac{E_{\text{kin,a}}}{10^{51} \text{ erg}}$
rp2_ddt4_dd09	0.725	0.380	0.570	1.08	4.43	1.24
rp2_ddt4_dd10	0.754	0.401	0.538	1.11	4.41	1.24
rp1_ddt1_dd07_1Z _⊙	1.00	0.734	0.349	0.446	1.84	1.40
rp1_ddt1_dd07_0.5Z _⊙	1.00	0.752	0.352	0.440	1.87	
rp1_ddt1_dd07_2Z _⊙	1.01	0.699	0.340	0.455	1.79	

Bibliography

- Arnett, D., & Livne, E. 1994a, *ApJ*, 427, 315
- . 1994b, *ApJ*, 427, 330
- Asplund, M., Grevesse, N., Sauval, A. J., & Scott, P. 2009, *ARA&A*, 47, 481
- Bader, G., & Deuflhard, P. 1983, *Numerische Mathematik*, 41, 373
- Benz, W., Cameron, A. G. W., Press, W. H., & Bowers, R. L. 1990, *ApJ*, 348, 647
- Bessell, M. S. 1990, *PASP*, 102, 1181
- Blinnikov, S. I., & Khokhlov, A. M. 1986, *Soviet Astronomy Letters*, 12, 131
- Blondin, S., Kasen, D., Röpke, F. K., Kirshner, R. P., & Mandel, K. S. 2011, *MNRAS*, 417, 1280
- Brachwitz, F., Dean, D. J., Hix, W. R., Iwamoto, K., Langanke, K., Martínez-Pinedo, G., Nomoto, K., Strayer, M. R., Thielemann, F.-K., & Umeda, H. 2000, *ApJ*, 536, 934
- Brahe, T. 1573, *De nova et nullius aevi memoria prius visa stella, iam pridem á nato Christo 1572, mense Novembri primum conspecta, contemplatio mathematica* (Kopenhagen: Laurentius Benedictus)
- Branch, D. 1998, *ARA&A*, 36, 17
- Branch, D., Fisher, A., & Nugent, P. 1993, *AJ*, 106, 2383
- Chandrasekhar, S. 1931, *ApJ*, 74, 81
- Ciaraldi-Schoolmann, F., Seitenzahl, I. R., & Röpke, F. K. 2012, *MNRAS*, submitted
- Clavin, P. 2004, *Chaos*, 14, 825
- Clifford, F. E., & Tayler, R. J. 1965, *MmRAS*, 69, 21
- Colella, P., & Glaz, H. M. 1985, *Journal of Computational Physics*, 59, 264
- Colella, P., & Woodward, P. R. 1984, *Journal of Computational Physics*, 54, 174
- Colgate, S. A., & McKee, C. 1969, *ApJ*, 157, 623
- Courant, R., Friedrichs, K. O., & Lewy, H. 1928, *Math. Ann.*, 100, 32
- Damköhler, G. 1940, *Z. f. Elektroch.*, 46, 601

Bibliography

- Dilday, B., Howell, D. A., Cenko, S. B., Silverman, J. M., Nugent, P. E., Sullivan, M., Ben-Ami, S., Bildsten, L., Bolte, M., Endl, M., Filippenko, A. V., Gnat, O., Horesh, A., Hsiao, E., Kasliwal, M. M., Kirkman, D., Maguire, K., Marcy, G. W., Moore, K., Pan, Y., Parrent, J. T., Podsiadlowski, P., Quimby, R. M., Sternberg, A., Suzuki, N., Tytler, D. R., Xu, D., Bloom, J. S., Gal-Yam, A., Hook, I. M., Kulkarni, S. R., Law, N. M., Ofek, E. O., Polishook, D., & Poznanski, D. 2012, *Science*, 337, 942
- Fickett, W., & Davis, C. 1979, *Detonation*, ed. D. H. Sharp & L. M. Simmons, Los Alamos Series in Basic and Applied Sciences (University of California Press)
- Filippenko, A. V. 1997, *ARA&A*, 35, 309
- Fink, M. 2010, PhD thesis, Technical University of Munich
- Fink, M., Hillebrandt, W., & Röpke, F. K. 2007, *A&A*, 476, 1133
- Fink, M., Röpke, F. K., Hillebrandt, W., Seitenzahl, I. R., Sim, S. A., & Kromer, M. 2010, *A&A*, 514, A53
- Fryxell, B. A., Müller, E., & Arnett, W. D. 1989, *Hydrodynamics and nuclear burning*, MPA Green Report 449, Max-Planck-Institut für Astrophysik, Garching
- Gamezo, V. N., Wheeler, J. C., Khokhlov, A. M., & Oran, E. S. 1999, *ApJ*, 512, 827
- Gamow, G., & Schoenberg, M. 1941, *Physical Review*, 59, 539
- Germano, M. 1992, *Journal of Fluid Mechanics*, 238, 325
- Golombek, I., & Niemeyer, J. C. 2005, *A&A*, 438, 611
- Green, D. A., & Stephenson, F. R. 2003, in *Lecture Notes in Physics*, Vol. 598, *Supernovae and Gamma-Ray Bursters*, ed. K. W. Weiler (Berlin Heidelberg New York: Springer-Verlag), 7–19, (preprint available: astro-ph/0301603)
- Hachisu, I., Kato, M., & Nomoto, K. 1999, *ApJ*, 522, 487
- Han, Z., & Podsiadlowski, P. 2004, *MNRAS*, 350, 1301
- Higham, D. J., & Trefethen, L. N. 1993, *BIT Numerical Mathematics*, 33, 285
- Hillebrandt, W., & Niemeyer, J. C. 2000, *ARA&A*, 38, 191
- Höflich, P., & Khokhlov, A. 1996, *ApJ*, 457, 500
- Höflich, P., Wheeler, J. C., & Thielemann, F. K. 1998, *ApJ*, 495, 617
- Homeier, D., Koester, D., Hagen, H., Jordan, S., Heber, U., Engels, D., Reimers, D., & Dreizler, S. 1998, *A&A*, 338, 563
- Howell, D. A., Sullivan, M., Nugent, P. E., Ellis, R. S., Conley, A. J., Le Borgne, D., Carlberg, R. G., Guy, J., Balam, D., Basa, S., Fouchez, D., Hook, I. M., Hsiao, E. Y., Neill, J. D., Pain, R., Perrett, K. M., & Pritchett, C. J. 2006, *Nature*, 443, 308

- Iben, Jr., I., & Tutukov, A. V. 1984, *ApJS*, 54, 335
- Iwamoto, K., Brachwitz, F., Nomoto, K., Kishimoto, N., Umeda, H., Hix, W. R., & Thielemann, F.-K. 1999, *ApJS*, 125, 439
- Jordan, IV, G. C., Fisher, R. T., Townsley, D. M., Calder, A. C., Graziani, C., Asida, S., Lamb, D. Q., & Truran, J. W. 2008, *ApJ*, 681, 1448
- Jordan, IV, G. C., Graziani, C., Fisher, R. T., Townsley, D. M., Meakin, C., Weide, K., Reid, L. B., Norris, J., Hudson, R., & Lamb, D. Q. 2012, *ArXiv e-prints*
- Kasen, D., Röpke, F. K., & Woosley, S. E. 2009, *Nature*, 460, 869
- Kerzendorf, W. E., Schmidt, B. P., Asplund, M., Nomoto, K., Podsiadlowski, P., Frebel, A., Fesen, R. A., & Yong, D. 2009, *ApJ*, 701, 1665
- Khokhlov, A. M. 1988, *Ap&SS*, 149, 91
- . 1989, *MNRAS*, 239, 785
- . 1991a, *A&A*, 245, 114
- . 1991b, *A&A*, 246, 383
- . 1991c, *A&A*, 245, L25
- . 2000, preprint: astro-ph/0008463
- Kobayashi, C., & Nomoto, K. 2009, *ApJ*, 707, 1466
- Kotak, R., Meikle, W. P. S., Pignata, G., Stehle, M., Smartt, S. J., Benetti, S., Hillebrandt, W., Lennon, D. J., Mazzali, P. A., Patat, F., & Turatto, M. 2005, *A&A*, 436, 1021
- Kromer, M., Fink, M., Stanishev, V., Taubenberger, S., Ciaraldi-Schoolman, F., Pakmor, R., Röpke, F. K., Ruiter, A. J., Seitenzahl, I. R., Sim, S. A., Blanc, G., Elias-Rosa, N., & Hillebrandt, W. 2012, *ArXiv e-prints*
- Kromer, M., & Sim, S. A. 2009, *MNRAS*, 398, 1809
- Kromer, M., Sim, S. A., Fink, M., Röpke, F. K., Seitenzahl, I. R., & Hillebrandt, W. 2010, *ApJ*, 719, 1067
- Landau, L. D., & Lifschitz, E. M. 1983, *Lehrbuch der theoretischen Physik*, Vol. 10, *Physikalische Kinetik* (Berlin: Akademie Verlag)
- . 2007, *Lehrbuch der theoretischen Physik*, Vol. 6, *Hydrodynamik* (Frankfurt am Main: Harri Deutsch Verlag)
- Langanke, K., & Martínez-Pinedo, G. 2001, *Atomic Data and Nuclear Data Tables*, 79, 1
- . 2003, *Reviews of Modern Physics*, 75, 819

Bibliography

- Leibundgut, B. 2000, *A&A Rev.*, 10, 179
- Lesaffre, P., Han, Z., Tout, C. A., Podsiadlowski, P., & Martin, R. G. 2006, *MNRAS*, 368, 187
- Lesaffre, P., Podsiadlowski, P., & Tout, C. A. 2005, *MNRAS*, 356, 131
- LeVeque, R. J. 1998, in *Computational Methods for Astrophysical Flows*, ed. O. Steiner & A. Gaultschi, Saas-Fee Advanced Course 27 (Berlin Heidelberg New York: Springer), 1–159
- Li, W., Leaman, J., Chornock, R., Filippenko, A. V., Poznanski, D., Ganeshalingam, M., Wang, X., Modjaz, M., Jha, S., Foley, R. J., & Smith, N. 2011, *MNRAS*, 412, 1441
- Lisewski, A. M., Hillebrandt, W., & Woosley, S. E. 2000, *ApJ*, 538, 831
- Liu, Z. W., Pakmor, R., Röpke, F. K., Edelmann, P., Wang, B., Kromer, M., Hillebrandt, W., & Han, Z. W. 2012, *A&A*, 548, A2
- Lorén-Aguilar, P., Isern, J., & García-Berro, E. 2009, *American Institute of Physics Conference Series*, 1122, 320
- Maeda, K., Röpke, F. K., Fink, M., Hillebrandt, W., Travaglio, C., & Thielemann, F. 2010, *ApJ*, 712, 624
- Maoz, D., Sharon, K., & Gal-Yam, A. 2010, *ApJ*, 722, 1879
- Marietta, E., Burrows, A., & Fryxell, B. 2000, *ApJS*, 128, 615
- Martínez-Pinedo, G., Langanke, K., & Dean, D. J. 2000, *ApJS*, 126, 493
- Moore, K., & Bildsten, L. 2012, *ArXiv e-prints*
- Müller, E. 1994, in *Lecture Notes in Physics*, Vol. 433, *Galactic Dynamics and N-Body Simulations*, ed. G. Contopoulos, N. K. Spyrou, & L. Vlahos (Berlin Heidelberg: Springer-Verlag), 313–363
- . 1998, in *Computational Methods for Astrophysical Flows*, ed. O. Steiner & A. Gaultschi, Saas-Fee Advanced Course 27 (Berlin Heidelberg New York: Springer), 343–494
- Nagataki, S., Hashimoto, M., Sato, K., & Yamada, S. 1997, *ApJ*, 486, 1026
- Niemeyer, J. C., & Hillebrandt, W. 1995, *ApJ*, 452, 769
- Niemeyer, J. C., & Woosley, S. E. 1997, *ApJ*, 475, 740
- Nomoto, K. 1980, *Space Science Reviews*, 27, 563
- . 1982, *ApJ*, 253, 798
- Nomoto, K., & Kondo, Y. 1991, *ApJ*, 367, L19

- Nomoto, K., Thielemann, F.-K., & Yokoi, K. 1984, *ApJ*, 286, 644
- Nugent, P., Sullivan, M., Bersier, D., Howell, D. A., Thomas, R., & James, P. 2011a, *The Astronomer's Telegram*, 3581, 1
- Nugent, P. E., Sullivan, M., Cenko, S. B., Thomas, R. C., Kasen, D., Howell, D. A., Bersier, D., Bloom, J. S., Kulkarni, S. R., Kandrashoff, M. T., Filippenko, A. V., Silverman, J. M., Marcy, G. W., Howard, A. W., Isaacson, H. T., Maguire, K., Suzuki, N., Tarlton, J. E., Pan, Y.-C., Bildsten, L., Fulton, B. J., Parrent, J. T., Sand, D., Podsiadlowski, P., Bianco, F. B., Dilday, B., Graham, M. L., Lyman, J., James, P., Kasliwal, M. M., Law, N. M., Quimby, R. M., Hook, I. M., Walker, E. S., Mazzali, P., Pian, E., Ofek, E. O., Gal-Yam, A., & Poznanski, D. 2011b, *Nature*, 480, 344
- Osher, S., & Sethian, J. A. 1988, *Journal of Computational Physics*, 79, 12
- Paczynski, B. 1972, *Astrophys. Lett.*, 11, 53
- Pakmor, R., Edelmann, P., Röpke, F. K., & Hillebrandt, W. 2012a, *MNRAS*, 424, 2222
- Pakmor, R., Hachinger, S., Röpke, F. K., & Hillebrandt, W. 2011, *A&A*, 528, A117+
- Pakmor, R., Kromer, M., Röpke, F. K., Sim, S. A., Ruiter, A. J., & Hillebrandt, W. 2010, *Nature*, 463, 61
- Pakmor, R., Kromer, M., Taubenberger, S., Sim, S. A., Röpke, F. K., & Hillebrandt, W. 2012b, *ApJ*, 747, L10
- Pakmor, R., Röpke, F. K., Weiss, A., & Hillebrandt, W. 2008, *A&A*, 489, 943
- Patat, F., Chandra, P., Chevalier, R., Justham, S., Podsiadlowski, P., Wolf, C., Gal-Yam, A., Pasquini, L., Crawford, I. A., Mazzali, P. A., Pauldrach, A. W. A., Nomoto, K., Benetti, S., Cappellaro, E., Elias-Rosa, N., Hillebrandt, W., Leonard, D. C., Pastorello, A., Renzini, A., Sabbadin, F., Simon, J. D., & Turatto, M. 2007, *Science*, 317, 924
- Perlmutter, S., Aldering, G., Goldhaber, G., Knop, R. A., Nugent, P., Castro, P. G., Deustua, S., Fabbro, S., Goobar, A., Groom, D. E., Hook, I. M., Kim, A. G., Kim, M. Y., Lee, J. C., Nunes, N. J., Pain, R., Pennypacker, C. R., Quimby, R., Lidman, C., Ellis, R. S., Irwin, M., McMahon, R. G., Ruiz-Lapuente, P., Walton, N., Schaefer, B., Boyle, B. J., Filippenko, A. V., Matheson, T., Fruchter, A. S., Panagia, N., Newberg, H. J. M., Couch, W. J., & The Supernova Cosmology Project. 1999, *ApJ*, 517, 565
- Perlmutter, S., Gabi, S., Goldhaber, G., Goobar, A., Groom, D. E., Hook, I. M., Kim, A. G., Kim, M. Y., Lee, J. C., Pain, R., Pennypacker, C. R., Small, I. A., Ellis, R. S., McMahon, R. G., Boyle, B. J., Bunclark, P. S., Carter, D., Irwin, M. J., Glazebrook, K., Newberg, H. J. M., Filippenko, A. V., Matheson, T., Dopita, M., Couch, W. J., & The Supernova Cosmology Project. 1997, *ApJ*, 483, 565
- Pfannes, J. M. M., Niemeyer, J. C., & Schmidt, W. 2010a, *A&A*, 509, A75+

Bibliography

- Pfannes, J. M. M., Niemeyer, J. C., Schmidt, W., & Klingenberg, C. 2010b, *A&A*, 509, A74+
- Phillips, M. M. 1993, *ApJ*, 413, L105
- Phillips, M. M., Li, W., Frieman, J. A., Blinnikov, S. I., DePoy, D., Prieto, J. L., Milne, P., Contreras, C., Folatelli, G., Morrell, N., Hamuy, M., Suntzeff, N. B., Roth, M., González, S., Krzeminski, W., Filippenko, A. V., Freedman, W. L., Chornock, R., Jha, S., Madore, B. F., Persson, S. E., Burns, C. R., Wyatt, P., Murphy, D., Foley, R. J., Ganeshalingam, M., Serduke, F. J. D., Krisciunas, K., Bassett, B., Becker, A., Dilday, B., Eastman, J., Garnavich, P. M., Holtzman, J., Kessler, R., Lampeitl, H., Marriner, J., Frank, S., Marshall, J. L., Miknaitis, G., Sako, M., Schneider, D. P., van der Heyden, K., & Yasuda, N. 2007, *PASP*, 119, 360
- Plewa, T., Calder, A. C., & Lamb, D. Q. 2004, *ApJ*, 612, L37
- Rauscher, T., & Thielemann, F.-K. 2000, *Atomic Data and Nuclear Data Tables*, 75, 1
- Reichl, L. 2009, *A Modern Course in Statistical Physics*, Physics Textbook (Weinheim: Wiley-VCH)
- Reinecke, M., Hillebrandt, W., & Niemeyer, J. C. 1999a, *A&A*, 347, 739
- . 2002a, *A&A*, 386, 936
- Reinecke, M., Hillebrandt, W., Niemeyer, J. C., Klein, R., & Gröbl, A. 1999b, *A&A*, 347, 724
- Reinecke, M., Hillebrandt, W., Niemeyer, J. C., Röpke, F., Schmidt, W., & Sauer, D. 2002b, in *Proceedings of the 11th Workshop on "Nuclear Astrophysics"*, Ringberg Castle, ed. W. Hillebrandt & E. Müller, MPA/P13 (Garching: Max-Planck-Institut für Astrophysik), 54–56
- Reinecke, M. A. 2001, PhD thesis, Technical University of Munich, available at <http://tumb1.biblio.tu-muenchen.de/publ/diss/allgemein.html>
- Riess, A. G., Filippenko, A. V., Challis, P., Clocchiatti, A., Diercks, A., Garnavich, P. M., Gilliland, R. L., Hogan, C. J., Jha, S., Kirshner, R. P., Leibundgut, B., Phillips, M. M., Reiss, D., Schmidt, B. P., Schommer, R. A., Smith, R. C., Spyromilio, J., Stubbs, C., Suntzeff, N. B., & Tonry, J. 1998, *AJ*, 116, 1009
- Riess, A. G., Filippenko, A. V., Li, W., Treffers, R. R., Schmidt, B. P., Qiu, Y., Hu, J., Armstrong, M., Faranda, C., Thouvenot, E., & Buil, C. 1999, *AJ*, 118, 2675
- Röpke, F. K. 2003, PhD thesis, Technical University of Munich
- . 2005, *A&A*, 432, 969
- . 2007, *ApJ*, 668, 1103

- Röpke, F. K., Gieseler, M., Reinecke, M., Travaglio, C., & Hillebrandt, W. 2006a, *A&A*, 453, 203
- Röpke, F. K., & Hillebrandt, W. 2004, *A&A*, 420, L1
- . 2005, *A&A*, 431, 635
- Röpke, F. K., Hillebrandt, W., Niemeyer, J. C., & Woosley, S. E. 2006b, *A&A*, 448, 1
- Röpke, F. K., Kromer, M., Seitenzahl, I. R., Pakmor, R., Sim, S. A., Taubenberger, S., Ciaraldi-Schoolmann, F., Hillebrandt, W., Aldering, G., Antilogus, P., Baltay, C., Benitez-Herrera, S., Bongard, S., Buton, C., Canto, A., Cellier-Holzem, F., Childress, M., Chotard, N., Copin, Y., Fakhouri, H. K., Fink, M., Fouchez, D., Gangler, E., Guy, J., Hachinger, S., Hsiao, E. Y., Chen, J., Kerschhaggl, M., Kowalski, M., Nugent, P., Paech, K., Pain, R., Pecontal, E., Pereira, R., Perlmutter, S., Rabinowitz, D., Rigault, M., Runge, K., Saunders, C., Smadja, G., Suzuki, N., Tao, C., Thomas, R. C., Tilquin, A., & Wu, C. 2012, *ApJ*, 750, L19
- Röpke, F. K., & Niemeyer, J. C. 2007, *A&A*, 464, 683
- Röpke, F. K., & Schmidt, W. 2009, in *Interdisciplinary Aspects of Turbulence*, ed. W. Hillebrandt & F. Kupka, *Lecture Notes in Physics* (Berlin: Springer-Verlag), 255–289
- Röpke, F. K., Woosley, S. E., & Hillebrandt, W. 2007, *ApJ*, 660, 1344
- Ruiter, A. J., Belczynski, K., & Fryer, C. 2009, *ApJ*, 699, 2026
- Ruiter, A. J., Belczynski, K., Sim, S. A., Hillebrandt, W., Fryer, C. L., Fink, M., & Kromer, M. 2011, *MNRAS*, 417, 408
- Ruiter, A. J., Sim, S. A., Pakmor, R., Kromer, M., Seitenzahl, I. R., Belczynski, K., Fink, M., Herzog, M., Hillebrandt, W., Röpke, F. K., & Taubenberger, S. 2012, *ArXiv e-prints*
- Ruiz-Lapuente, P. 2012, *Nature*, 481, 149
- Ruiz-Lapuente, P., Comeron, F., Méndez, J., Canal, R., Smartt, S. J., Filippenko, A. V., Kurucz, R. L., Chornock, R., Foley, R. J., Stanishev, V., & Ibata, R. 2004, *Nature*, 431, 1069
- Saio, H., & Nomoto, K. 1985, *A&A*, 150, L21
- . 1998, *ApJ*, 500, 388
- Schaefer, B. E., & Pagnotta, A. 2012, *Nature*, 481, 164
- Schmidt, B. P., Suntzeff, N. B., Phillips, M. M., Schommer, R. A., Clocchiatti, A., Kirshner, R. P., Garnavich, P., Challis, P., Leibundgut, B., Spyromilio, J., Riess, A. G., Filippenko, A. V., Hamuy, M., Smith, R. C., Hogan, C., Stubbs, C., Diercks, A., Reiss, D., Gilliland, R., Tonry, J., Maza, J., Dressler, A., Walsh, J., & Ciardullo, R. 1998, *ApJ*, 507, 46

Bibliography

- Schmidt, W., Niemeyer, J. C., & Hillebrandt, W. 2006a, *A&A*, 450, 265
- Schmidt, W., Niemeyer, J. C., Hillebrandt, W., & Röpke, F. K. 2006b, *A&A*, 450, 283
- Seitenzahl, I. R., Ciaraldi-Schoolmann, F., Röpke, F. K., Fink, M., Hillebrandt, W., Kromer, M., Pakmor, R., Ruiter, A. J., & Sim, S. A. 2012, *MNRAS*, submitted
- Seitenzahl, I. R., Meakin, C. A., Townsley, D. M., Lamb, D. Q., & Truran, J. W. 2009, *ApJ*, 696, 515
- Seitenzahl, I. R., Röpke, F. K., Fink, M., & Pakmor, R. 2010, *MNRAS*, 407, 2297
- Sharpe, G. J. 1999, *MNRAS*, 310, 1039
- Shen, K. J., & Bildsten, L. 2007, *ApJ*, 660, 1444
- Shen, K. J., Kasen, D., Weinberg, N. N., Bildsten, L., & Scannapieco, E. 2010, *ApJ*, 715, 767
- Shore, S. N. 2007, *Astrophysical Hydrodynamics*, 2nd edn. (Berlin: Wiley-VCH), 452
- Sim, S. A. 2007, *MNRAS*, 375, 154
- Sim, S. A., Röpke, F. K., Hillebrandt, W., Kromer, M., Pakmor, R., Fink, M., Ruiter, A. J., & Seitenzahl, I. R. 2010, *ApJ*, 714, L52
- Smiljanovski, V., Moser, V., & Klein, R. 1997, *Combustion Theory Modelling*, 1, 183
- Stein, J., & Wheeler, J. C. 2006, *ApJ*, 643, 1190
- Sternberg, A., Gal-Yam, A., Simon, J. D., Leonard, D. C., Quimby, R. M., Phillips, M. M., Morrell, N., Thompson, I. B., Ivans, I., Marshall, J. L., Filippenko, A. V., Marcy, G. W., Bloom, J. S., Patat, F., Foley, R. J., Yong, D., Penprase, B. E., Beeler, D. J., Allende Prieto, C., & Stringfellow, G. S. 2011, *Science*, 333, 856
- Sussman, M., Smereka, P., & Osher, S. 1994, *Journal of Computational Physics*, 114, 146
- Thielemann, F.-K., Argast, D., Brachwitz, F., Hix, W. R., Höflich, P., Liebendörfer, M., Martinez-Pinedo, G., Mezzacappa, A., Nomoto, K., & Panov, I. 2003, in *From Twilight to Highlight: The Physics of Supernovae*, ed. W. Hillebrandt & B. Leibundgut, 331–343
- Thielemann, F.-K., Nomoto, K., & Hashimoto, M.-A. 1996, *ApJ*, 460, 408
- Thielemann, F.-K., Nomoto, K., & Yokoi, K. 1986, *A&A*, 158, 17
- Timmes, F. X., & Arnett, D. 1999, *ApJS*, 125, 277
- Timmes, F. X., Brown, E. F., & Truran, J. W. 2003, *ApJ*, 590, L83
- Timmes, F. X., & Swesty, F. D. 2000, *ApJS*, 126, 501
- Timmes, F. X., & Woosley, S. E. 1992, *ApJ*, 396, 649

- Toonen, S., Nelemans, G., & Portegies Zwart, S. 2012, *A&A*, 546, A70
- Travaglio, C., Hillebrandt, W., & Reinecke, M. 2005, *A&A*, 443, 1007
- Travaglio, C., Hillebrandt, W., Reinecke, M., & Thielemann, F.-K. 2004, *A&A*, 425, 1029
- Truran, J. W., Arnett, W. D., & Cameron, A. G. W. 1967, *Canadian Journal of Physics*, 45, 2315
- Umeda, H., Nomoto, K., Kobayashi, C., Hachisu, I., & Kato, M. 1999, *ApJ*, 522, L43
- Wang, B., & Han, Z. 2010, in *American Institute of Physics Conference Series*, Vol. 1314, *American Institute of Physics Conference Series*, ed. V. Kologera & M. van der Sluys, 244–249
- Webbink, R. F. 1984, *ApJ*, 277, 355
- Whelan, J., & Iben, I. J. 1973, *ApJ*, 186, 1007
- Winkler, K.-H. A., Norman, M. L., & Mihalas, D. 1984, *Journal of Quantitative Spectroscopy and Radiative Transfer*, 31, 473
- Woosley, S. E. 2007, *ApJ*, 668, 1109
- Woosley, S. E., Kerstein, A. R., Sankaran, V., Aspden, A. J., & Röpke, F. K. 2009, *ApJ*, 704, 255
- Woosley, S. E., Taam, R. E., & Weaver, T. A. 1986, *ApJ*, 301, 601
- Yoon, S.-C., & Langer, N. 2004, *A&A*, 419, 623

Zusammenfassung

In der vorliegenden Diplomarbeit wurde der Einfluss der Zusammensetzung des Weißen Zwerges als Vorläufersystem auf thermonukleare Supernovae untersucht.

Supernovae sind variable astronomische Erscheinungen, die als solche die Menschheit schon sehr lange faszinieren. Sie stellen die hellsten Ereignisse im Universum dar und können auf dem Maximum ihrer Helligkeit ihre komplette Heimatgalaxie überstrahlen. Mit dem Aufkommen besserer Teleskope und Spektrographen im 20. Jahrhundert war es möglich, Supernovae von Novae zu unterscheiden und anhand ihrer optischen Eigenschaften in Unterkategorien einzuteilen. Die für diese Arbeit relevanten Typ Ia Supernovae zeigen keine Spuren von Wasserstoff oder Helium im Spektrum, dafür aber eine ausgeprägte Silizium-Linie. Die meisten Objekte dieser Kategorie werden durch thermonukleare Explosionen Weißer Zwerge, die aus Kohlenstoff und Sauerstoff bestehen, ausgelöst. Die Energie wird dabei durch die nuklearen Reaktionen von C und O zu Eisengruppenelementen, hauptsächlich ^{56}Ni , geliefert. Die γ -Quanten, die beim anschließenden Zerfall des ^{56}Ni und des Tochterkerns ^{56}Co entstehen, sind für die Helligkeit der Supernova verantwortlich. Auf dem Weg durch die Explosionsprodukte werden diese γ -Quanten mehrfach absorbiert und wieder emittiert, wodurch dann das beobachtete Spektrum zustande kommt.

Ziele

Ziel dieser Diplomarbeit ist es, die numerische Modellierung dieser Explosionsphase zu verbessern, indem verschiedene Kompositionen der Vorläufersysteme in Betracht gezogen werden. Die Motivation für diese Verbesserung ist zum Einen eine genauere Modellierung, da Sternentwicklungsmodelle Vorläufersysteme mit variabler Komposition und einem Kern mit geringerem Massenanteil von Kohlenstoff voraussagen, wobei dieser Anteil von der Entwicklung des Vorläufersterns abhängt. Bisherige Modellierungen von verzögerten Detonationen von Weißen Zwergen nahe der Chandrasekhar-Masse mit denselben numerischen Methoden legten als Anfangsmodell eine homogene Zusammensetzung mit einem Massenanteil von Kohlenstoff von 0.5 zugrunde (z.B. Seitenzahl et al., 2012).

Zum Anderen soll überprüft werden, ob die Modellierung anderer Anfangszusammensetzungen in der Lage ist, Beobachtungen besser zu reproduzieren. Dazu müssen synthetische Lichtkurven und Spektren aus Strahlungstransportrechnungen mit Beobachtungen verglichen werden. Außerdem soll untersucht werden, ob die auftretende Variabilität in der chemischen Zusammensetzung die variablen Helligkeiten normaler Typ Ia Supernovae erklären kann.

Grundlagen

Ein Weißer Zwerg stellt das Endstadium von Sternen mit Massen $\lesssim 8 M_{\odot}$ dar. Diese Masse reicht nicht aus, um den Stern so stark zu kontrahieren, dass die nächste Stufe nuklearen Brennens nach Wasserstoff- und Heliumbrennen im Innern einsetzt. Da Weiße Zwerge nun durch den Entartungsdruck der Elektronen stabilisiert werden, sind sie in Einzelsternsystemen stabile Objekte. In einem Binärsternsystem hingegen kann der Begleitstern Materie auf den Weißen Zwerg transferieren, was zu einem Anwachsen der Masse des Weißen Zwerges bis zur Chandrasekhar-Masse führen kann. Trotz der intensiven Forschung auf diesem Gebiet steht noch nicht fest, wie genau das Vorläufersystem beschaffen ist, d.h. welcher Art der Begleitstern ist und wie genau die Explosion abläuft. Verschiedene Möglichkeiten werden diskutiert, so etwa verzögerte Detonationen von Weißen Zwergen nahe der Chandrasekhar-Masse, doppelte Detonationen von Weißen Zwergen weit unterhalb der Chandrasekhar-Masse und gewaltsame Verschmelzungen von zwei Weißen Zwergen.

Der Weiße Zwerg besteht aus einem Plasma aus Atomkernen, die einer Maxwell-Boltzmann-Verteilung folgen, und Elektronen, die in verschiedenem Grade entartet und relativistisch sind. Der Gravitationsdruck der Materie wird durch den Entartungsdruck der Elektronen ausgeglichen. Erreicht der Weiße Zwerg durch Massenakkretion jedoch die kritische Chandrasekhar-Masse, wird er instabil und durch eine thermische Instabilität kann eine thermonukleare Flamme entstehen.

Es gibt generell zwei Propagationsarten thermonuklearer Flammen, ähnlich zu chemischen Flammen: Deflagrationen und Detonationen. Deflagrationen breiten sich mit Unterschallgeschwindigkeit aus und werden durch Wärmeleitung von der heißen Asche in den Brennstoff angetrieben. Detonationen hingegen breiten sich mit Überschallgeschwindigkeit aus und werden durch die Kompression einer führenden Schockwelle getrieben. In der Schockwelle wird die Materie komprimiert und dadurch über die Schwelle erhitzt, bei der thermonukleare Reaktionen einsetzen. Deren Energiefreisetzung wiederum treibt den Schock an. Diese beiden Flammenarten unterscheiden sich außerdem in ihren Brennprodukten in Abhängigkeit von der Dichte.

In der vorliegenden Arbeit werden die verzögerten Detonationen von Weißen Zwergen genauer untersucht. In diesem Szenario beginnt die thermonukleare Explosion mit einer Deflagration, die nahe des Zentrums gezündet wird. Durch die hydrodynamische Rayleigh-Taylor-Instabilität wird das Voranschreiten der Flammenfront beschleunigt und es entsteht eine turbulente Flamme, die eine verwinkelte, fraktal-ähnliche Struktur aufweist. Nach einer gewissen Zeit ändern sich die Eigenschaften der Flamme und das Einsetzen einer Detonation wird möglich, die den Rest des Sternes verbrennt. Die Reaktionsprodukte der Flammen hängt von der Dichte der unverbrannten Materie vor der Flammenfront ab, bei hohen Dichten werden Eisengruppenelemente erzeugt, bei niedrigeren Dichten herrscht Brennen zu Elementen mittlerer Masse vor. Da sich durch die Deflagration, die sich mit Unterschallgeschwindigkeit fortpflanzt, der Weiße Zwerg ausdehnt, sinkt die Dichte und die anschließende Detonation verbrennt weniger Materie zu Eisengruppenelementen. Dieses Szenario ist in der Lage, die aus Beobachtungen abgeleiteten ^{56}Ni -Massen von etwa $0.6 M_{\odot}$ zu reproduzieren.

Modellierung

Die thermonukleare Explosion wird mit Hilfe von hydrodynamischen Simulationen untersucht. Hierbei wird das Plasma des Weißen Zwergs als Kontinuum angenommen, sodass die Euler-Gleichungen der Hydrodynamik angewandt werden können. Diese werden auf einem numerischen Gitter mit der Methode der Finiten Volumen diskretisiert. Diese hat den Vorteil, Erhaltungsgrößen – wie etwa Masse, Impuls und Energie – durch die numerische Implementation exakt zu erhalten.

Da die direkte Implementierung der nuklearen Reaktionen aufgrund der unterschiedlichen Zeitskalen sehr rechenzeitaufwändig ist, wird ein vereinfachtes Verfahren benutzt: die „level set“-Methode. In dieser Methode wird die Flammenfront als Isofläche des Nullwerts einer Distanzfunktion dargestellt, wobei die Reaktionsprodukte instantan direkt hinter der Flammenfront erzeugt werden. Dies ist vor allem für Detonationen bei hohen Dichten und für Deflagrationen im Allgemeinen eine sehr gute Näherung, da die Flammendicken um viele Größenordnungen unter der Auflösung des Gitters liegen. Die Werte für die Zusammensetzung der Reaktionsprodukte hängen von der Zusammensetzung und der Dichte des unverbrannten Materials ab und werden einer Tabelle entnommen, die vor den eigentlichen Simulationen erstellt werden muss. Diese Tabelle wurde mit Hilfe einer iterativen Kalibrierungsmethode separat für Detonationen und Deflagrationen erstellt.

Um dennoch detaillierte Informationen über die Zusammensetzung der Explosionsprodukte zu erhalten, werden sogenannte „Tracerteilchen“ eingesetzt, welche passiv mit dem hydrodynamischen Fluss advektiert werden. Da dies dem Lagrange-Bezugssystem entspricht, hängt die chemische Zusammensetzung nur von der thermodynamischen Trajektorie (Dichte, Temperatur) ab und kann in einem separaten Schritt, dem Postprozessieren, berechnet werden.

In der iterativen Kalibrierung der Tabellen für die Energiefreisetzung werden abwechselnd hydrodynamische Simulationen und Postprozessierungsschritte durchgeführt, wobei die Ergebnisse des Postprozessierens zur Berechnung einer neuen Tabelle für die nächste Iteration benutzt werden.

Ergebnisse

Die iterative Kalibrierung der Tabellen für die „level set“-Methode wurde für Deflagrationen und Detonationen bei verschiedenen Anfangszusammensetzungen durchgeführt. Hierdurch können auch Modelle mit variierender Anfangszusammensetzung, die durch den Massenanteil des Kohlenstoffs charakterisiert sind, behandelt werden. Die Tabellen zeigen zwei charakteristische Eigenschaften in Abhängigkeit von der Anfangszusammensetzung: Einerseits ist die totale Energiefreisetzung niedriger für geringere Kohlenstoffanteile, was durch die geringere Differenz der Bindungsenergien zu den Produkten des Brennens, also hauptsächlich Eisengruppenelementen mit hoher Bindungsenergie, erklärt werden kann. Zum Anderen verschieben sich die Übergänge in die einzelnen Brennphasen (C-, O-, Si-Brennen) zu höheren Dichten für niedrigere Kohlenstoffmassenanteile. Zusammen führen diese beiden Effekte dazu, dass die Brennfronten – Deflagrationen

und Detonationen – für geringere Massenanteile des Kohlenstoffs systematisch weniger nukleare Energie freisetzen.

Die Tabellen aus dem Kalibrierungsverfahren wurden nun benutzt, um zwei- und dreidimensionale Simulationen von verzögerten Detonationen für verschiedene Anfangskompositionen – homogen und variabel – durchzuführen. Ein wesentlicher Effekt ist die geringere Produktion von ^{56}Ni für geringere Kohlenstoffanteile bei gleichen Zündkonfigurationen. Die geringere Energiefreisetzung führt zu einer schwächeren Entwicklung der Deflagration mit geringeren turbulenten Geschwindigkeitsfeldern. Dadurch wird die Detonation erst bei niedrigeren Dichten gezündet und produziert daher weniger ^{56}Ni . Insgesamt ergibt sich durch die veränderte Entwicklung eine geringere Gesamtmasse von ^{56}Ni . Daraus lässt sich schließen, dass variable Anfangszusammensetzungen, die von den Sternentwicklungsmodellen je nach Vorläuferstern vorhergesagt werden, auch zu einer Variabilität in der produzierten ^{56}Ni -Masse und somit der Helligkeit der Supernova führt. Dies bedeutet, dass die Verschiedenheit der Typ Ia Supernovae in der Helligkeit zumindest teilweise durch Variationen der Anfangszusammensetzung erklärt werden kann.

Um die Ergebnisse der Simulationen mit Beobachtungen zu vergleichen, wurden für drei 2D-Modelle Strahlungstransport-Rechnungen von M. Kromer¹ durchgeführt. Berechnungen des Strahlungstransportes simulieren die Propagation sowie Absorptions- und Emissionsprozesse von Photonenpaketen. Sie liefern synthetische Lichtkurven und Spektren, die mit beobachteten Supernovae verglichen werden können. Der Aufbau der Lichtkurven und Spektren basiert dabei auf der Struktur der Explosionsprodukte im Geschwindigkeitsraum. Im Groben sind alle Modelle im Geschwindigkeitsraum ähnlich aufgebaut; sie zeigen eine geschichtete Struktur mit einem Kern aus ^{56}Ni und stabilen Eisengruppenelementen, der von äußeren Hüllen aus Elementen mittlerer Masse (v.a. Si) und unverbranntem Material (O, C) umgeben ist. Allerdings hängt die Geschwindigkeit, bei der die einzelnen Schichten auftreten, von der Anfangszusammensetzung ab. Da die freigesetzte Energie abzüglich der anfänglichen Gravitationsenergie in die kinetische Energie der expandierenden Hülle umgewandelt wird, hängen die Geschwindigkeiten der einzelnen Schichten von der gesamten Energie ab, die für geringere C-Massenanteile kleiner ist. Dies führt dazu, dass die Geschwindigkeit des Si, die ein dominantes Merkmal im Spektrum bestimmt, von der Anfangszusammensetzung abhängt.

Die berechneten Lichtkurven und Spektren wurden mit beobachteten Supernovae verglichen. Dabei zeigt sich, dass die absoluten Helligkeiten und Anstiegszeiten mit normalen Supernovae vergleichbar sind. Die Lichtkurven der berechneten Spektren weisen allerdings einen Überschuss in roten Bändern auf. Im blauen *B*-Band stimmt die Lichtkurve um das Maximum relativ gut mit Beobachtungen überein. Im *V*-Band hingegen, bei größeren Wellenlängen, ist am Maximum die Helligkeit der berechneten Modelle zu hoch. Die Ursache hierfür liegt wahrscheinlich in den vergleichsweise hohen Geschwindigkeiten der Eisengruppenelemente. Da die Eisengruppenelemente über dem Teil des Kerns liegen, in dem die Strahlung ausgesandt wird, können sie Strahlung aus dem blauen Bereich absorbieren und im roten Bereich wieder emittieren. Man sollte

¹Max-Planck-Institut für Astrophysik, Garching

allerdings auch beachten, dass die drei Modelle im Vergleich zur beobachteten Supernova eine höhere gesamte ^{56}Ni -Masse aufweisen. Für die 3D-Modelle sollte die Rötung der Lichtkurven schwächer sein, da hier geringere Geschwindigkeiten für den inneren Kern aus Nickel und Eisengruppenelementen auftreten. Die synthetischen Spektren zeigen ebenfalls einen zu hohen Fluss im roten Bereich, können aber sonst die Hauptmerkmale des beobachteten Spektrums reproduzieren. Speziell die Si II-Absorptionslinie verschiebt sich zu niedrigeren Geschwindigkeiten und daher höheren Wellenlängen für einen geringeren Kohlenstoffmassenanteil und damit zu einer besseren Übereinstimmung mit dem beobachteten Spektrum.

Insgesamt lässt sich sagen, dass die realistischere Modellierung der Anfangszusammensetzung zu einer besseren Übereinstimmung mit der beobachteten Supernova führt als die bisher benutzten, generischen Annahmen.

Ausblick

Um realistischere Vergleiche mit beobachteten Spektren zu erhalten, müssen noch mehr 3D-Modelle mit anschließendem Strahlungstransport berechnet werden. Dies wird es auch erlauben, Effekte bezüglich der Beobachtungsrichtung zu betrachten.

Darüber hinaus können die in dieser Arbeit erhaltenen Tabellen auch benutzt werden, um den Effekt unterschiedlicher Anfangszusammensetzungen auf andere Modelle zu untersuchen, wie etwa das Szenario der doppelten Detonation von Weißen Zwergen unterhalb der Chandrasekhar-Masse oder das Szenario der gewaltsamen Verschmelzung zweier Weißer Zwerge.

Danksagung

Zunächst möchte ich meinem Betreuer Prof. Friedrich Röpke herzlich dafür danken, dass er es mir ermöglicht hat, meine Diplomarbeit in seiner Gruppe in Würzburg anzufertigen, und dass er mir immer mit Rat und Tat zur Seite stand, gerade auch in der letzten Phase.

Dann möchte ich mich bei Prof. Guido Drexlin bedanken, der sich freundlicherweise bereit erklärt hat, meine Arbeit in Karlsruhe zu betreuen; auch dafür, dass seine Vorlesungen mein Interesse in die Astrophysik (wieder) erweckt hat.

Ich möchte allen Kollegen am Institut für die herzliche Arbeitsatmosphäre bedanken, insbesondere unserer Arbeitsgruppe. Für fachlichen Rat sowie schöne Abende danke ich Michael, Ivo, Kai und Alejandro. Stephan danke ich auch für die Bereitstellung von Spektren sowie allgemeine Diskussionen über Beobachtungen. Mein Dank gilt natürlich auch dem zweiten Stock, allen voran Till, Annika und Robert.

Aus der „erweiterten Gruppe“ möchte ich besonders Markus danken, der die Strahlungstransportrechnungen für die 2D-Modelle durchgeführt hat; außerdem Rüdiger, der bei technischen Problemen gerne weiter half.

Allen, die meine Arbeit durchgelesen haben, danke ich für ihre Korrekturvorschläge und die Zeit, die sie sich dafür genommen haben.

Ich möchte außerdem Watz danken, der den Rechner „Bocksbeutel“ eingerichtet hat, auf dem viele meiner 2D Simulationen liefen. Dem Rechenzentrum Jülich danke ich für die Bereitstellung von Rechenzeit unter HMU13, wodurch ich die 3D Simulationen auf JUGENE und JUQUEEN durchführen konnte.

Ein ganz besonderer Dank gebührt meinen Eltern Josef und Regine, die mich schon immer in allem unterstützt haben, auch und gerade im Studium; auch dafür, dass ich immer gerne nach Hause komme. Meinem Bruder Dominik danke ich für die zahlreichen entspannenden Spielerunden sowie immer gelungene Konzertbesuche.

Zu guter Letzt möchte ich Isa danken, dass sie gemeinsam mit mir nach Würzburg gekommen ist; ohne sie wäre dieses Jahr in Würzburg sicherlich nur halb so schön gewesen.

Eigenständigkeitserklärung

Hiermit versichere ich, die vorliegende Arbeit selbstständig verfasst zu haben und keine Quellen oder Hilfsmittel außer den angegebenen verwendet zu haben.

Karlsruhe, den 20. November 2012,

Sebastian Ohlmann